Novel Self-Sealing Materials and Poromechanical Analysis for Permanently Plugging Wells for Abandonment (P&A) in High Temperature Environments

by

Yunxing Lu

B.S. Geotechnical Engineering, Nanjing Tech University, 2015

M.S Geotechnical Engineering, Texas A&M University, 2017

Submitted to the Graduate Faculty of the

Swanson School of Engineering in partial fulfillment

of the requirements for the degree of

Doctor of Philosophy

University of Pittsburgh

2022

UNIVERSITY OF PITTSBURGH

SWANSON SCHOOL OF ENGINEERING

This dissertation was presented

by

Yunxing Lu

It was defended on

November 3, 2022

and approved by

Enick, Robert M, PhD, Professor, Department of Chemical and Petroleum Engineering

Lin, Jeen-Shang, PhD, Associate Professor, Department of Civil and Environmental Engineering

Alessandro Fascetti, PhD, Assistant Professor, Department of Civil and Environmental Engineering

Dissertation Director: Bunger, Andrew P, PhD, Associate Professor, Department of Civil and Environmental Engineering, Department of Chemical and Petroleum Engineering

Novel Self-Sealing Materials and Poromechanical Analysis for Permanently Plugging Wells for Abandonment (P&A) in High Temperature Environments

Yunxing Lu, PhD

University of Pittsburgh, 2022

Permanent abandonment refers to the final stage of the life-cycle for a petroleum well. Because the goal is to render harmless a well that will never again be accessed, plugging must be done in such a way that the material is effective and resilient over geological time. The difficulties and cost of P&A are mainly coming from two parts: the harsh P&A conditions (high temperature, high pressure, acidic reservoir conditions, and mud contamination) and the lack of guidance from P&A codes and standards. Thus motivated, this research is firstly aimed at demonstrating the feasibility of generating new "Geologically Activated Cement" (GAC) plugging material that turns the above mentioned harsh conditions of deep-water wells into an advantage. More importantly, if damaged, the GAC can self-seal within a few hours when subjected to flow of acidic fluid under HPHT conditions. This self-sealing trait provides the potential for a resilient cementing system. Secondly, with aid of a new semi-analytical solution for thermo-poro-elastic (TPE) stresses in a cylindrical cement plug that includes consideration of full coupling between hydraulic and thermal transport models, this work rigorously challenges the status quo design assumption that a lower permeability barrier material always better. To the contrary, because extremely low permeability porous material is slow to drain excess pore pressure, low permeability cement can be prone to damage from thermally-induced pore pressure buildup. Furthermore, the analysis is the first to identify an important role of specific heat of the cement in preventing pore pressure buildup, thereby showing a new way forward for cement design that targets high specific heat additives.

Thirdly, this research presents an experimental demonstration of a novel mode of periodic tensile cement failure that could be commonly encountered in the life span of wells that undergo rapid temperature and/or pressure cycling. This is the first demonstration of such predictably spaced periodic cracks under conditions relevant to P&A operations. Overall, these findings provide new materials and analysis methods that invoke change in P&A codes and practices and therefore aim make P&A more reliable and resilient over geological timeframes.

Table of Contents

Preface xiv

1.0 Introduction 1

1.1 The Upcoming P&A Waves 1

1.2 What the Current P&A System Code Provides 3

1.3 Current State of the Art in Advanced Plugging Materials 8

1.3.1 Micro/Nano Particle Enhanced Wellbore Cements 8

1.3.2 Carbonation Enhanced Wellbore Cements 10

1.3.3 Using the Magnesium Carbonates as New Cementitious Binders 17

1.3.4 Three-Dimensional and Four-Dimensional Printing Technology 19

1.4 Current Placement and Verification Techniques for P&A 20

1.5 Summary of Knowledge Gaps 22

1.6 Objectives and Scope of this Dissertation Research 24

2.0 Experimental Study of Genesis of a Geologically Activated and Self-Sealing Cementing Material for Deep Wellbore Plugging and Abandonment 27

2.1 Chapter Summary 27

2.2 Introduction 28

2.3 Experimental Procedures 33

2.3.1 Genesis of GAC Materials 33

2.3.2 Self-Sealing of GAC Materials 36

2.4 Results 38

2.4.1 Genesis of Geologically Activated Cementing Materials 38

2.4.2 Self-Sealing Behavior 42

2.5 Discussions... 46

2.5.1 Binding Mechanism of GAC 46

2.5.2 Self-Sealing Mechanism of GAC...48

2.5.3 Carbonation Level and Reaction Rate 49

2.6 Conclusions 51

3.0 Semi-Analytical Solution for Thermo-Poro-Elastic Stresses in a Wellbore Cement Plug and Implications for Cement Properties that Minimize Risk of Failure 54

3.1 Chapter Summary 54

3.2 Introduction 55

3.3 Governing Equations... 59

3.4 PTEOF Solution for Constrained Cylinder 63

3.4.1 Problem Description and Boundary Conditions 63

3.4.2 Solution to The Fully Coupled Diffusion Equations 65

3.5 Behavior of The Model.. 70

3.5.1 Pore Pressure Responses and Thermal Osmosis Effect 71

3.5.2 Thermo-Osmosis and Thermo-Filtration Effects......................................75

3.5.3 Effective Stress 78

3.6 Pairwise Bivariate Analysis and Dimensional Analysis 80

3.6.1 Pairwise Bivariate Analysis for Each Variable 82

3.6.2 Parameter Groups Governing Effective Stress Evolution 85

3.7 Conclusions 90

4.0 Prediction and Demonstration of Periodic Dilation Band Formation in Rate-Dependent Porous Cement 93
4.1 Chapter Summary 93
4.2 Introduction 94
4.3 Governing Equations of Periodic Dilation Band Theory 97
4.4 Behavior of the Model 101
4.5 Experimental Demonstration 107
4.5.1 Experimental Setup and Procedures 107
4.5.2 Experimental Results 110
4.6 Discussions 111
4.7 Conclusions 116
5.0 Conclusions 119
Appendix A Details of Stehfest's Method 124
Bibliography 125

List of Tables

Table 1 Current cement integrity related standards and regulations 4

Table 2 Summary of proportion of each ingredients for carbonation reaction.................... 35

Table 3 Results of the solubility test. 39

Table 4 Self-sealing data of class H cement and GAC under HTHP testing conditions 46

Table 5 Notation.. 61

Table 6 Lower boundary and upper boundary for Monte Carlo Sampling 80

Table 7 Unloading time and experimental measured spacing of each specimen in Figure 32 111

List of Figures

Figure 1 The distribution of the wells that await abandonment in the United States (up to 2021.5) (raw data available via: https://www.fractracker.org). 2

Figure 2 The numbers of the wells that await abandonment in each state in the United States (up to 2021.5) (raw data available via: https://www.fractracker.org). 2

Figure 3 Well locations in GoM (up to 2022.5) (raw data available via: https://skytruth-org.carto.com). 3

Figure 4 Illustration of four main factors (high temperature, high pressure, acidic fluid, and drilling mud contaminations) that are threating the integrity of well barrier material in geological time frame. 29

Figure 5 Conceptual illustration of three potential outcomes of permeability evolution of a material that has been damaged, where the reduction with time indicates a resilient response to the damage. 31

Figure 6 Relative increase in carbonation rate of olivine at elevated pressure and temperature compared to surface conditions (after Keleman and Matter 2008, with permission). 33

Figure 7 Left: laboratory setup for carbonated olivine generation; Right: experimental setup for the self-sealing test. 36

Figure 8 (a) Pre-reaction: loose olivine sand; (b) post-reaction: hardened carbonated masses in the reactor. 40

Figure 9 The results of XRD of the reaction product (the black color arrow labels on the are the reference locations of different phases of Magnesium Carbonate in the Power Diffraction File (PDF)). 40

Figure 10 Post-reaction products under SEM and point 1-5 are selected for EDS analysis. 41

Figure 11 Element spectrum of selected points in Figure 10. 42

Figure 12 (a) permeability change of class H cement during HPHT self-sealing tests (citric acid group); (b) permeability change of GAC during HPHT self-sealing tests (citric acid group). 44

Figure 13 (a) Permeability change of class H cement during HTHP self-sealing tests (carbonic acid group);(b) permeability change of GAC cement during HTHP self-sealing tests (carbonic acid group). 46

Figure 14 Inferred binding mechanism of Geologically Activated Cement material. 48

Figure 15 (a) Sketch showing a primary plug in P&A and its boundary conditions; (b) A zoom in sketch showing a cross-section of the plug in plane-strain conditions and its boundary conditions. 64

Figure 16 (a) Pore pressure change (p) due to mode 1 loading, where the curves grade from gray to black as time increases; (b) Evolution of pore pressure change (p) induced by mode 1 at center of the cylinder (r=0) 72

Figure 17 (a) Pore pressure change (p) due to mode 2 loading, where the curves grade from gray to black as time increases; (b) Evolution of pore pressure change (p) induced by mode 2 at center of the cylinder (r=0) 72

Figure 18 (a) Pore pressure change (p) due to mode 3 loading, where the curves grade from gray to black as time increases; (b) Evolution of pore pressure change (p) induced by mode 3 at center of the cylinder (r=0) 73

Figure 19 Various ratios of kpt/k(thermo-osmosis's influence) impacting the mode 2 induced pore pressure shown at (10-4 days). 75

Figure 20 The development of temperature change (T) under loading mode 2, where the curves grade from gray to black as time increases. 77

Figure 21 Various ratios of kt/ktp (thermal filtration's influence) impacting the temperature change (T) due to loading mode 1. 77

Figure 22 Effective radial stress of cement, with tension positive, where the curves grade from gray to black as time increases (boundary conditions and input values of each parameter are stated at Eq.3-35). 79

Figure 23 The algorithm that is used to construct the parametric studies. 81

Figure 24 Pairwise bivariate distributions for eleven variables. The blue distribution on diagonals indicate distribution of the parameters for comparative cases, while orange shows distribution for tensile. 83

Figure 25 (a) Z1 and Z2 plot with tensile cases (red color) and compressive cases (green color). Note the range of Zeta One can be larger than 1 based on the ranges of the selected parameters. (b) The probability plot of generating tensile cases on different Z1 . 89

Figure 26 The influence of Zeta 1 on the Mode 2 induced pore pressure. Peak 1 is recalled from Fig. 17 Right; The permeability of Peak 2 is three orders of magnitude smaller than Peak 1, the rest of selected parameters remain the same as Peak 1; The specific heat of Peak 3 is two orders of magnitude smaller than Peak 2, the rest of selected parameters remains the same as Peak 2. 90

Figure 27 Illustrations of the initial and boundary conditions during dilation in the unloading progress. 101

Figure 28 Different solution behaviors of when material sensitivity m and Zeta is taking different values. 105

Figure 29 When m=2, two different power law relationships occur between the number of singularities (N) and Zeta based on different ranges of Zeta. The orange dash line is an illustration for fitting purpose when the exponent is 1/2. 106

Figure 30 Experimental setup of the decompression tests, includes the axial loading system, confining stress system, and temperature-control system. 109

Figure 31 (a) The internal structure of the Hoek-cell; (b) Specimen with its boundary conditions and the loading and unloading paths. 109

Figure 32 Measurement of tensile bands spacing occurs during decompression test at room temperature and 90 C. The location of each observed fractures is indicated and labeled by an arrow on the right side. 110

Figure 33 Power law relationship between unloading time and spacing from the experimental observation is summarized in Table 7. 112

Figure 34 Left: Compaction band surface is characterized by grain translation, displacement, or even crushing in poorly consolidated sand and sandstone; Right: dilation bands surface is characterized by planar opening-mode fractures with two discrete and neat surface. 114

Preface

I would be lying if I said I didn't dream about this moment before. However, when I finally sit down, try to organize the words in my heart and pick up the threads, I find it is not as easy as I thought.

First and foremost, I would like to give my sincerest thanks and appreciation to my PhD advisor – Prof. Andrew Bunger, for accepting me into his group, providing me with this amazing opportunity to work on the NAS project, and involving me in many other different projects. His guidance through my Ph.D. program is extremely important - he not only helps me to strengthen and solidify my knowledge and understanding of the mechanics but also shapes my scientific thinking and inspires me on how to approach scientific problems in the future. Meanwhile, I also appreciate his trust in giving me a lot of freedom to implement many adventurous ideas in the lab (also for allowing me to sleep and "live" in the lab). More importantly, by working with him and watching him, I learned how to become a better person – it is not merely about the rigorous scientific attitude, virtues of discipline, and hardworking, but also how to love, respect, and care for people around you. I believe what I learned from him will be beneficial for my entire life. Without him, all of these were impossible. I also deeply value the insightful suggestions, comments, and contributions of my thesis committee members - Profs. Lin, Jeen-Shang, Alessandro Fascetti, and Enick, Robert M. I also would like to give many thanks to Prof. Mileva Radonjic from Oklahoma State University, who is always caring and encouraging me throughout my Ph.D. program.

The outstanding technical staff here at Pitt are super friendly and helpful. Hager Charles, aka Scooter, has never stopped amazing and surprising me for his excellent experimental preparations and helps during my Ph.D. studies. I lose count of the number of times that I went to his machine shop and desperately asked him for help. It was him that made me get through the deadlines one after another with great outcomes. I would also like to thank the staff from our admin office – Grogan Alysia, Morand Cheryl, Kozak Katie. The great and joyful talks with them always brighten my days, and after that, I usually will have more nicknames that will be flowing within our department, the famous ones would be “A-A-RON” or simply “Aaron”.

I am very lucky and be able to meet and know all of our lab members: the graduated alumnus Drs. Wei Fu, Guanyi Lu, Pengju Xing, Navid Zolfaghari, Yao Huang, Qiao Lu, Delal Gunaydin-Tulu, and current lab members Maggie Benge and Mustafa, Ayyaz. At the same time, I also would like to give thanks to Spencer-Williams Isaiah, Nina Chang, and Aubrey Green, who gave me a lot of help and supports for my Ph.D. studies on experimental testing and thesis writing when they were working as undergrad summer interns in the Hydraulic Fracturing Lab. It was an honor to work with them during my Ph.D. time, especially, I am very grateful that I can develop life-long friendships with some of them that can enrich my entire career. I am also grateful for the support from my Aggies from A&M over the years: Drs. Xi Luo, Yong Deng, Mark Wang, Jack Kong, Jeff Shi, Shuna Ni, Yunlong Zhang. Even though most of them are not in College Station anymore and we have not seen each other for many years, they are always reachable by phone call or message whenever I need them.

I would like to extend my thanks to my former committee member Dr. Luis Vallejo from Pitt and my undergraduate advisor Guanglong Huang, who, although are no longer with us, continue to inspire us with their legacy and commitments to their students.

There were many ups and downs during my PhD time, especially the stumbling journey after I failed my first qualifier, I still clearly remember the pain even after many years but am still truly grateful for experiencing such a period of time in my life. Through these dark periods, the main strength and supporting source are coming from the faith in an amazing God. Thus, I appreciate the great lectures from David Pawson and the great music from Hillsong Worship, Lamb Music, DonMoen TV, and many others. Because of them, many sleepless nights are becoming less suffering and more peaceful, actually filling with hope to embrace the dawn. I also want to especially thank Ken Wagoner - the meetings and hangouts with him and with our group members are recharging me every time.

Last but not the least, this dissertation is for my beloved family, my parents, Ying Li and Longchen Lu, and my fiancé, Dr. Mengyan Li, who are always supporting me with their unconditional love. I cannot express my gratitude enough for all that they have done for me. Furthermore, I want to give special thanks to Prof. Yanyuan Ma from Penn State University, who has taken Mengyan and I in as family especially during the pandemic, and always inspires us in many different ways.

Benedum Hall
Pittsburgh
Nov. 11th 2022

1.0 Introduction

1.1 The Upcoming P&A Waves

Different from a temporarily abandoned well and a suspended well, a permanent abandonment well implies that the well is at the last stage of its life cycle (drilling, completion, production, and abandonment) and it will never be used or re-accessed (Khalifeh et al., 2020). Hence the well must be plugged with an everlasting perspective accounting for all expected situations that the well might encounter during the entire abandonment period, which is called plug and abandonment (P&A). P&A is not as easy as pouring cement into the wellbore and hoping it will form a proper seal. Instead, it is considered one of the most delicate operations conducted on the rig and is also resource intensive in terms of time, money, and technology (Hmadeh, 2021).

The database FracTracker, which was originally developed to aid investigation for health concerns by addressing data availability gaps surrounding western Pennsylvania fracking, is now a non-profit organization that provides timely and provocative data about the risks on communities from oil and gas development. Based on their data records of the abandoned wells, we visualized them on the map, as shown in Figure 1, with the help of the Python library. Each dot in Figure 1 represents a well that needs or waits to be properly abandoned. By the time of May 2021, there are a total of 203726 wells in the United States that needs P&A. Figure 2 shows the distribution of wells in each state. It shows that California, Kansas, and Illinois are the top three states that have wells that need to be P&A, with numbers of 38555, 31353, and 19819, respectively.

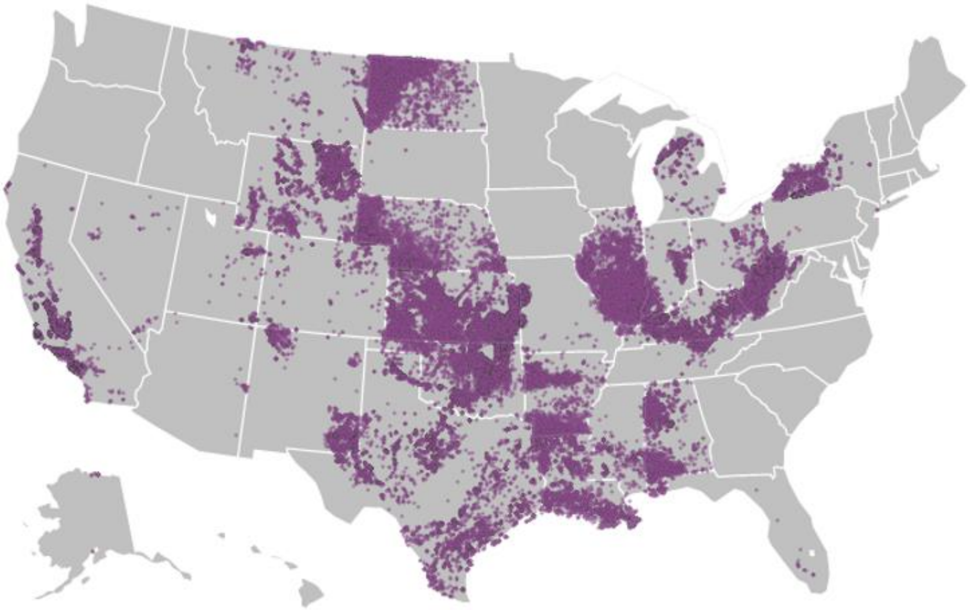

Figure 1 The distribution of the wells that await abandonment in the United States (up to 2021.5) (raw data available via: https://www.fractracker.org).

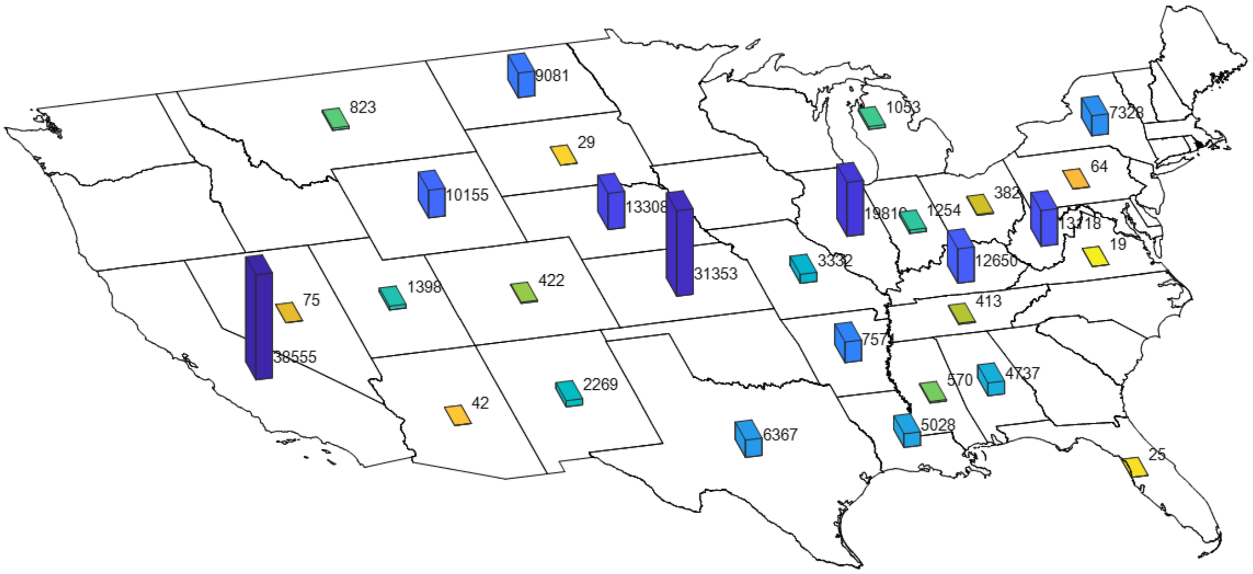

Figure 2 The numbers of the wells that await abandonment in each state in the United States (up to 2021.5) (raw data available via: https://www.fractracker.org).

The cost of P&A operations can be very high. For example, the industry projection for Norway is an abandonment of 3308 wells (Aarlott, 2016) in the North Sea that will require 15 rigs on full time P&A over 40 years. By the mid-way point of the year 2022, there are a total of 51312 wells in the Gulf of Mexico (GoM) and their distributions are shown in Figure 3. They are expected to plug and abandon 4582 deep-water wells, as well as 20989 shallow-water wells (Kaiser et al., 2018). By using the same statistics model of the Norway industry, back of the envelope calculations reveal that the deep-water wells alone will take the GoM 50-55 years, 15 rigs, and over 300 billion dollars.

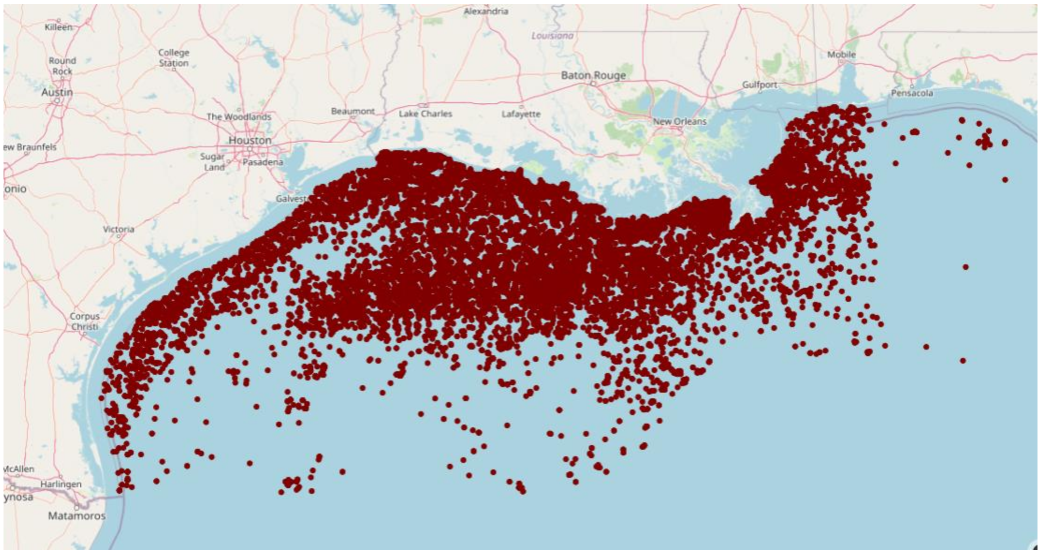

Figure 3 Well locations in GoM (up to 2022.5) (raw data available via: https://skytruth-org.carto.com).

1.2 What the Current P&A System Code Provides

Unfortunately, up to now, there are no universal standards and regulations that specially design for P&A operations. This is the result of several factors. First of all, nearly all of the current cementing integrity related codes, which are summarized in Table 1, do not encompass the entire life cycle of the well, as most of them focus on drilling, completion, and production phases while the P&A phase is left behind. One exception is that the NORSOK D-010, which is an important standard followed by many industry professionals and companies, provides a rough guidance of the P&A operations. For example, they advise on the minimum barrier numbers and minimal length of each barrier in the P&A system in an attempt to reduce leakage paths and therefore strengthen the integrity of the P&A system. According to NORSOK D-010, for the barrier to stay impermeable for eternity, the required length of the cement plug is 100 m measured depth if the plug is set inside a casing, and 50 m if a mechanical plug is used as a basis (Hmadeh, 2021). In addition to that, it is also vital that the plug should extend a minimum of 50 m above any source of inflow or leakage point.

Table 1 Current cement integrity related standards and regulations

	Standards Name	Code
1	Isolating Potential Flow Zones During Well Construction	API RP 65-2 (2010)
2	Deepwater Well Design and Construction	API RP 96 (2011)
3	Annular Casing Pressure Management for Offshore Wells	API RP 90 (2012)
4	Annular Casing Pressure Management for Onshore Wells	API RP 90-2 (2016)
5	Well Integrity in Drilling and Well Operations	NORSOK D-010 (2013)
6	Recommended Guidelines for Well Integrity	Norwegian Oil & Gas 117 (2017)
7	Well Integrity - Part 1: Lifecycle Governance Manual	ISO 16530-1 (2017)

However, these two measures are far from controlling leaking wells completely. By reviewing the tragedy that is the Deepwater Horizon oil spill at Macondo (Bly, 2011; Group, 2011; Water, 2011), we learn that even the P&A system has several wellbore barrier elements, and if one of them fails to carry out its function properly, the balance of the whole system will be broken by the accumulative effects. This could accelerate the degradation of the system or even lead to a system failure. Thus, it is important to know that the NORSOK D-010 solely serves as a recommendation provider to execute the requirements of the regulations issued by the Norwegian Petroleum Safety Authority (PSA). In other words, this standard only describes the minimum requirements to maintain P&A through design, planning, and execution of P&A operations in Norway, and it is not a universal standard. It also does not include many current challenging factors such as fatigue/creep failure due to load and thermal cycle/variations caused by high temperature and high pressure, etc., into consideration. Thus, only following this guidance will not necessarily ensure long term P&A safety and integrity.

Second, by the law of U.S. Bureau of Land Management Instruction Memorandum No.NM-95-022, it is the operating company's responsibility to plan and design the well operation in a way that secures the well's integrity throughout the entire life cycle of the well. Especially for P&A operations, the operating company should be responsible for ensuring that there are no leaks in the well even after the operation is done, because if any leaks happen in the long run, the company is held responsible to pay all the costs to clean and re-plug the well properly. This has led to many operating companies having their own internal regulations and requirements for the P&A operations.

Considering what has been said so far, without very comprehensive, specific, and strict codes to follow, the void of clear guidance will impose a big challenge on any P&A operations team. To make matters more complicated, the well will have already passed through many phases, and in turn a large amount of information obtained prior to the abandonment phase may have changed, which leads to many more unknowns that could jeopardize the quality of P&A work.

The well integrity, which is defined in NORSOK D-010 (2021) as: “application of technical, operational, and organizational solutions to reduce risk of uncontrolled release of formation fluids throughout the life cycle of a well”, has to be achieved by the well barrier elements. The primary use of well barrier elements is to avert any leakage, ensure complete and adequate isolation of mobile fluids, and prevent leakage within the wellbore and unintentional flow from the seabed or surface (Vrålstad et al., 2019). Well barriers must be established in every stage of the well’s life cycle from drilling, testing, completion, production, and finally plugging & abandonment. NORSOK D-010 recommends (but does not require) a set of properties for a permanent well barrier, such as being non-shrinking, impermeable, and mechanical load/impact durable. However, these are still minimal requirements and will not ensure the P&A’s safety and integrity in the long term. The main cause of leaky wellbores is inadequate performance of wellbore cement when faced with challenging reservoir conditions. Although Portland cement (class H and G) is by far the most commonly used plugging material for offshore abandonment in the world (Vrålstad et al., 2019), these materials were initially designed for wells drilled at low pressure and temperature conditions, within competent formations, and with required service lives of 20-30 years (Corina et al., 2019a; Maurice B Dusseault et al., 2000). Portland cement is also not designed for geochemical compatibility with subsurface formations (Bachu et al., 2009; Barlet-Gouédard et al., 2009), so the stability over an extended period of time is unknown. When they are placed in high pressure high temperature (HPHT) formations, exposed to corrosive fluid, contaminated with drilling fluid, subjected to complex completions and stimulations, there is a substantial risk that the current wellbore barrier materials will be insufficient and it will cause leaky wellbores (Beltrán-Jiménez et al., 2019b; Katende et al., 2020a; Kiran et al., 2017). At the same time, the leaky pathways could occur at multiple locations. The microscopic scale of these pathways makes them very hard to locate and mitigate, which makes leaky wellbores the most difficult to plug and abandon (Standard, 2004).

In fact, some of the important threatening factors, such as high temperature and high pressure (HTHP), are missing in the list that NORSOK D-010 provides; thus, some of requirements that it asks are controversial and may not be realistic. For example, the NORSOK D-010 states that in order to prevent the flow of hydrocarbons and/or over pressurized fluids through the wellbore, the barriers must be impermeable. Although the low permeability is the most essential characteristic to trap the flow within the wellbore, simply defining impermeability as the ultimate goal could be misguiding. Let us firstly clarify that impermeable material is not the same as material that has no porosity. Known as the cementitious saturated porous material with varying porosity at different scales (Banthia et al., 1989; Goto et al., 1981; Meng et al., 2021; Picandet et al., 2011), the cement's behavior can be heavily influenced by the thermo-hydraulic-mechanical (THM) coupling in the porous space, especially when it is experiencing large temperature and pressure variations. Within the porosity and permeability range mentioned above, a very large pore pressure could be induced by the THM coupling and the pore pressure would be progressively reestablished over time, which would also lead to the changing of the effective stress, and increase the possibility of shear failure, hydraulic fracturing, or even tensile failure (Ghabezloo et al., 2010). While THM coupling phenomena in porous media has been studied by considerable researchers, their applications have been mainly focused on the wellbore stability during drilling and fluid injection into borehole (Detournay et al., 1988; Gao et al., 2017; Song et al., 2019; Tao et al., 2010; Zhou et al., 2009). The THM coupling effect in the cementing and plugging designs and operations has rarely been properly considered and fully investigated under HTHP conditions, which could result in jeopardizing the cementing integrity and lead to many serious consequences. More importantly, these THM coupling related issues cannot be addressed by any of the current available additives, because none of them can change the intrinsic nature, i.e. the porous structure, of the cement.

1.3 Current State of the Art in Advanced Plugging Materials

Besides the HTHP conditions, other factors such as geofluid attack, tectonic stresses exerted by formation, and unconsolidated formations also impose a great impact on the sealing barrier. Despite many deficiencies that Portland cement has under the deep-well P&A situations, it is still the most used plugging material due to its low cost and ready availability. Thus, many pioneering researches, summarized below, have been dedicated to improving the performance of the Portland cement by adding different additives and using cutting-edge technology, such as 3D printing.

1.3.1 Micro/Nano Particle Enhanced Wellbore Cements

The potential of micro/nano particles to improve the cement's performance mainly comes from their reduced particle size which significantly increases their surface-area to volume ratio, which not only decreases the setting time and accelerates the hardening of the cement without losing the final strength (Ginebra et al., 2004), but also increases the final strength of the hardened conditions by altering the microstructure development (Aggarwal et al., 2015; Senff et al., 2009). Nano-silica is one of the most popular and frequently used nanoparticle groups, and has been studied and gained extensive attention over the last two decades (Aggarwal et al., 2015; Gaitero et al., 2008; Hou et al., 2014; Hou et al., 2015; Sanchez et al., 2014; Singh et al., 2013). The purpose of the nano-silica is to fill the gaps in the void space of the cement and consequently increase its mechanical properties, such as compactness and bonding strength. However, the nano-silica has a very high cost, a significant carbon footprint, and can cause some serious health problems, like silicosis (de Brito et al., 2021).

For the reasons mentioned above, various studies have been conducted to find a suitable replacement for nano-silica, one of which is a pozzolanic material (also known as geopolymer), which is generally used to describe the amorphous to crystalline reaction products from the reaction of a solid aluminosilicate (Davidovits, 1991). However, this reaction has to be accompanied with a highly concentrated aqueous alkali hydroxide or silicate solution as a precursor, creating a so-called alkali-activated cement. The most common pozzolanic materials are fly ash (FA) and metakaolin (MK) (Bu et al., 2016; Luhar et al., 2021). The geopolymer is famous for reducing the greenhouse emissions while performing comparably to ordinary Portland cement. Luhar et al. (2021) carried out an experiment on lignite-based fly ash and sodium silicate solution with sodium hydroxide (NaOH) as activating reagents. They reported that the strength development was dependent on the ratio by mass of sodium silicate to NaOH and the concentration of NaOH. Davidovits (1991) investigated the effect of the water, sodium hydroxide, and sodium silicate contents in the synthesis of class F fly ash (FFA) based geopolymers obtained from the Greek Public Power Corporation S.A. derived from lignite combustion. It was observed that water content was a crucial parameter in the synthesis of fly ash-based geopolymers for the development of mechanical strength. The sodium hydroxide content and the amount of sodium silicate solution in the synthesis of geopolymers were found to significantly affect their compressive strength. Khalifeh et al. (2014) also showed usability of class C fly ash (CFA) geopolymer for oil well cementing. In their experiment, they showed that the curing temperature affects the early compressive strength development. For the particular CFA that they used for their experiment, they observed that as the temperature rises from 87 C to 125 ℃, a reaction takes place at the higher concentrations of NaOH which decreases the compressive strength at the higher temperature. Despite the variety of the geopolymers, they all utilize the same chemistry to describe the material synthesizing: a complex system of coupled alkali-mediated dissolution and precipitation reactions in an aqueous reaction substrate (Duxson et al., 2007). But this important chemical reaction is not suitable for the challenging P&A conditions where the alkaline precursor will be jeopardized by the acidic geofluid.

1.3.2 Carbonation Enhanced Wellbore Cements

Carbonation is one of the chemical degradations that occur to cement paste when the pH of the pore solution is decreased by CO_2 existing in the reservoir (Duguid et al., 2011; Marangu et al., 2019). It will cause decalcification of the gel binder and precipitation of calcium carbonate. In the acidic environment, the conventional cement has very limited resistance to carbonation (Mahmood et al., 2021). The rapid drop in pH will cause the dissolution of portlandite ($Ca(OH)_2$), followed by the decalcification of the main binding phase, the calcium-silicate-hydrate (C-S-H) gel. Carbonation of C-S-H gel is an important chemical degradation process that controls concrete durability (Morandeau et al., 2015a). Carbonation of C-S-H gel will occur naturally under atmospheric conditions, and consists of the removal of calcium ions from the gel, which leads to the formation of an amorphous silica gel and various polymorphs of calcium carbonate, such as amorphous calcium carbonates, calcite, vaterite, and aragonite (Kutchko et al., 2007; Kutchko et al., 2008). During the carbonation process, C-S-H gel transforms rapidly into a predominately amorphous silica gel, with most of the calcium being leached out from the C-S-H gel and incorporated into amorphous calcium carbonate prior to quickly transforming into a more stable crystalline polymorph (Morandeau et al., 2015b). However, the results presented by Morandeau et al. (2015a) indicates that the extent of carbonation-induced chemical degradation, which governs the removal of calcium from the calcium-alumino-silicate-hydrate (C-A-S-H) gel, can be reduced by tailoring the precursor chemistry, specifically the magnesium content. High-magnesium alkali-activated slag (AAS) is seen to form stable magnesium-containing amorphous calcium carbonate phases, which prevents the removal of additional calcium from the C-A-S-H gel, thereby halting the progress of the carbonation reaction and mitigating the carbonation-induced chemical degradation (Abdel Gawwad et al., 2017; Morandeau et al., 2015b; Zhang et al., 2016).

As discussed above, the carbonation reaction of cement is conventionally considered as an unfavorable event, as it demeans the durability performances of such materials. However, there are research interests focusing on the beneficial aspects of carbonation of cement-based materials recently. Generally speaking, there are two major beneficial features involved in it: A. rapid strength gain of the cementitious matrix when curing it in the presence of CO2 (because the presence of CO_2 accelerates the reaction of calcium silicates); B. sequestration of CO_2 in concrete (Ashraf, 2016).

Some knowledge of the key characteristics associated with developing the carbonate binders or using carbonation to activate binders can be drawn from the geological evolution of carbonate binders which occurs in nature, such as the limestone, beach rock, dolomite, and magnesite. Although these products may take geological time (thousands of years) to occur, they are considered the main rock-forming carbonate minerals in nature and are proven to possess superior chemical and physical properties (De Silva et al., 2006; De Silva et al., 2009). The superior qualities of these geological materials are attributed to their compacted, interlocked, and well-developed crystalline calcium and/or magnesium carbonate microstructures (De Silva et al., 2006). Therefore, in developing carbonate binders to achieve the goal of “cap rock restoration” in the deep well plug and abandonment in situ, obtaining microstructures that replicate, or to a certain extent, are similar to those of nature, is one of the main tasks researchers face. The concept of carbonation-activated binders was first proposed by De Silva et al. (2006). They show a detailed insight into the process of the development of carbonate binders from the carbonation of hydrated lime, with respect to both the rate of hydrated lime conversion and the strength of the binder. They concluded that the crystalline state and the morphology of the carbonate formed are critical to the strength of the binder.

The possibility of activating low lime calcium silicates as carbonation-activated binders was first tried by Ashraf et al. (2015).The strength development of this type of binder relies on the carbonation reaction of its ingredients (i.e., calcium silicates (Ashraf et al., 2016)). The crystalline calcium carbonate and highly polymerized amorphous silica gels formed during the carbonation process of low calcium silicates minerals are responsible for the strength development of hardened pastes. Ashraf et al. (2018) also present the mechanical properties from microscopic and macroscopic views of the products from the carbonation activated binders test. In their work, the mechanical properties of the individual microscopic phases were evaluated using the nano-indentation test, whereas the overall strength of the carbonated paste was evaluated using a macroscale three-point bending test. Correlations between the mechanical performances and microstructural characteristics revealed the performance controlling factors of the carbonation activated binders. They concluded that the higher bound water contents of the carbonated matrix tend to increase the short-term (up to 3 hours) creep deformation of the matrix when subjected to constant stress. The presence of a higher proportion of poorly-crystalline forms of calcium carbonates (i.e., aragonite, vaterite, and amorphous calcium carbonate) were observed to increase the flexural strength but decrease the elastic modulus of the carbonated matrix. Three individual carbonated wollastonite paste samples, each representing a different degree of carbonation, were selected for nanoindentation tests. The obtained elastic moduli for silica gel, calcium carbonate, and unreacted wollastonite grains were, respectively, 41.7 GPa, 67.3 GPa, and 134.7 GPa (Ashraf et al., 2018). The degree of polymerization of the Ca-modified silica gel is substantially higher than that of the calcium silicate hydrate (C-S-H) gel present in a hydrated ordinary Portland cement system.

However, it is important to note that there will be different productions from the carbonation process of calcium silicate minerals depending on the properties of the starting material. Ashraf et al. (2015) studied the hydration and carbonation reactions of individual calcium silicate system such as tricalcium silicate (or dicalcium silicate) instead of the conventional cement binders which are composed of both tri- and di- calcium silicates. They used laboratory based synthetic tri- and di- calcium silicates (by mixing the CaO and SiO_2 in different proportions) and natural wollastonite as the test materials. These samples were subjected to carbonation and hydration reactions at room temperature for 24 hours. They found that in case of tri- and di-calcium silicates, the main reaction products were identified as $Ca(OH)_2$, $CaCO_3$, and C-S-H for both hydration and carbonation reactions. For the wollastonite specimens, the main reaction products were $CaCO_3$ and polymerized silica rich phase.

One main concern of achieving the mineral carbonation is the reaction rate. Recent research has focused on two broad processes to achieve the goal of olivine mineral carbonation: gas-solid process and aqueous sorption. In the gas-solid process, carbonation occurs by chemisorption of

CO_2 to the solid by the strong chemical bonds, or by physisorption by weaker inter-molecular bonds. In aqueous sorption, CO_2 is initially dissolved into the solvent and is subsequently reacted with the mineral feedstock (Power et al. 2013). One of the major benefits of the gas-solid carbonation process is its simple design compared with a gas-water-solid system (dioxide-water-rock). Power et al. (2013) lists the forsterite, serpentine, and brucite as three potential mineral feedstock for the gas-solid carbonation, and he also compares the reaction rates with each other. In Power's conclusions, these reaction rates can be generally improved by higher gas pressure and temperature; however, they are also subject to thermodynamic limitations. For example, the decomposition of Mg-carbonate begins at 406 ℃, and the rate of olivine carbonation begins to decrease at an even lower temperature due to the chemical potential for reaction (O'Connor et al., 2005a). At higher pressure, the range of temperatures that promote carbonation is considerably larger (Lackner et al., 1997). Fosterite, serpentine, and brucite have different reaction rates. Experimental rates of Mg-silicate carbonation using gas-solid processes are too slow for large scale application. Even under highly favorable conditions (5000 psi, 500℃), a powder (20 um) Mg-silicate sample does not react appreciably. In contrast, the carbonation of brucite was nearly complete after two hours under the same conditions (Lackner et al., 1997). So Power et al. (2013) conclude that the brucite is a better feedstock for gas-solid carbonation, compared to Mg-silicate minerals. However, magnesium hydroxides are not abundant in nature and extracting them from Mg-silicate minerals without using large chemical or energy inputs remains the principal challenge to achieving significant, large-scale gas-solid carbonation.

Due to the slow reaction rate of the gas-solid reaction, there is a focus on aqueous carbonation pathways. Aqueous carbonation involves a reaction of CO_2 and water with solids. There may be an additional step of cations from the feedstock followed by an acid-base reaction between metal oxides and CO_2. The aqueous carbonation can be divided into the following steps: the dissolution and hydration of CO_2 in water, the dissolution of silicate minerals using forsterite (as an example), and the precipitation of carbonate. If we combine the above steps, the process can yield a net aqueous carbonation reaction, which is represented by the fifth step. Under the scenario of aqueous carbonation, olivine and pyroxene have the greatest potential for CO_2 storage capacity by mineral trapping, i.e., ~2 tons and 1.3-1.4 tons of CO_2 per m^3 of rock, respectively. This capacity is a consequence of the following two factors: firstly, the strong disequilibrium of olivine and pyroxene in the presence of aqueous fluid under shallow crustal conditions can improve the reaction rate of the dissolution and carbonation, secondly, the high ratio of divalent cations silica can provide abundant Mg^{2+} ,Fe^{2+},Ca^{2+} to form carbonates when olivine dissolves in a CO_2 – rich aqueous fluid.

Generally speaking, the overall reaction rate for the aqueous carbonation process is dependent on the slowest, rate-limiting steps. Basically, the carbonate precipitation is much faster than the dissolution reaction of olivine and pyroxene. Several experimental studies evaluated the kinetics of olivine and pyroxene dissolution in the presence of CO_2, as they assume the silicate dissolution is the limiting rate step of the overall carbonation process. All of these experiments show that the rate of olivine dissolution increases with increasing P_{CO2}, temperature, NaCl concentration, and with decreasing pH. The fastest known olivine carbonation was observed in studies at the U.S. Department of Energy’s Albany Research Center (O’Connor et al., 2005a) and at Arizona State University (Chizmeshya et al., 2007a). These studies combined olivine dissolution with carbonate precipitation at an olivine-to-water ratio of 1:4. Olivine in saline aqueous solutions with 1 M NaCl and high bicarbonate (e.g., $NaHCO_3$, $KHCO_3$) concentrations was held in a closed reaction vessel at high P_{CO2} (>70 bar). The fastest rates were at 185 °C. Rates were 103 times faster than those for the same conditions without bicarbonate, and more than 106 times faster than rates observed and calculated at 25 °C, pH 8, and atmospheric levels of P_{CO2}. The olivine carbonation proceeded to over 80% in 6h in these optimum conditions. Based on the results from the initial test series, it was theorized that solution pH plays a conflicting role in the two-stage reaction process. While acidic solutions should favor mineral hydrolysis and improve silicate dissolution rates, carbonate precipitation likely requires alkaline solutions. Thus, a buffered solution chemistry (NaCl & $NaHCO_3$) was formulated to permit simultaneous silicate dissolution and carbonate precipitation.

The extent of the product formation of the olivine carbonation depends on the conditions and rates of the preceding reactions. If these processes are operated in different conditions, three different products (Magnesite, Nesquehonite, and Lansfordite) of the olivine carbonation reaction can be obtained, even while using the same reactant (forsterite), to trap the CO_2. This is very important information for future research of olivine carbonation due to carbon dioxide-water-rock interactions, because some researchers have found that the carbonation has some beneficial effects on the properties of cement materials in unreinforced concrete, including microstructure densification and mechanical strength improvement (De Silva et al., 2006; De Silva et al., 2009; Mo et al., 2017). These beneficial effects are closely associated with the formation of $CaCO_3$, magnesium carbonates, and magnesian calcite, which are also considered to be the main rock-forming carbonate minerals in nature. So De Silva et al. (2009) are trying to use the magnesium carbonates as well as calcium magnesium carbonates as cementitious binders. Her preliminary results showed that the compressive strength of the carbonate is improved with the presence of nesquehonite and/or other magnesium-containing phases, which is better than the equivalent calcium system.

1.3.3 Using the Magnesium Carbonates as New Cementitious Binders

Due to the poor thermal conductivity of mass concrete, its temperature may increase significantly due to the heat of cement hydration, which then causes significant thermal shrinkage during the cooling period and leads to the shrinkage cracking at later ages (Mo et al., 2014). As a relative new technology, the MgO has been employed in the cement clinker or as an expansive additive to compensate for the thermal shrinkage of mass concrete, especially dam concrete, for almost 40 years. The definition of MgO cement is a mixture of PC and reactive magnesia in different proportions, depending on their intended application (Unluer et al., 2013). The hydration product of MgO, $Mg(OH)_2$, is far less soluble than portlandite and its pH is stable in the long term imparting enhanced chemical stability. The formation of $Mg(OH)_2$ is expansive with around two-fold solid volume increase, so compensating shrinkage with expansion produced by MgO has been proved to effectively prevent thermal cracking of mass concrete, reduce the cost of temperature control measures, and speed up the construction process. As an expansive cement or expansive additive, MgO has many advantages. They can be summarized as follows:

- Its chemically stable hydration product, namely $Mg(OH)_2$
- Relatively low water requirement for the hydration of MgO
- Rapid expansion produced by MgO with high reactivity, which can thus be used for compensating the shrinkage of concrete at an early stage, and its expansion properties are designable.

However, the use of magnesium carbonates as cementitious binders is not very common to date, and there are just a few literatures available on the subject, especially concerning information regarding how to obtain the magnesium carbonates binders from the magnesium silicate mineral. In addition to the relevance of these systems as binders, MgCO3 is also known to be the main product in the CO_2 sequestration process by magnesium-containing minerals. Serpentine ($Mg_3Si_2O_5(OH)_4$) and brucite ($Mg(OH)_2$) are Mg-rich lamellar minerals that are being investigated worldwide in relation to the CO_2 sequestration process. Overall, the availability and low cost of these minerals, combined with the exothermic nature of the carbonation process, provides exciting potential for economically viable product development (De Silva et al., 2009).

During the formation of calcium carbonate, the foreign ions (Mg^{2+}, OH^{-1}, and SO_4^{-2}) have the most important impact. Among these foreign ions, magnesium can be considered as the most influential ion in calcium carbonate formations. Depending on the Mg/Ca ratio at the start, different carbonate phases are known to be formed. In the work of De Silva et al. (2009), they used laboratory-grade magnesium hydroxide as the magnesium source and industrial-grade CO_2 as the carbon source throughout the work. Their equipment allowed samples to be compacted and subsequently exposed to CO_2 at different gas pressures. All the mix formulations have the same water/solid (w/s) ratio of 0.25, but have different ratios of magnesium hydroxide and calcium hydroxide, in order to obtain the different Mg/Ca molar ratios. Then a known amount of mixture was compacted at 2 MPa mechanical pressure for 2 minutes and exposed to two different CO_2 pressures (14 psi & 300 psi) at room temperature (~ 23℃) and 50 RG for 24 hours before being subjected to strength measurements and solid phase analysis by XRD, SEM, and EDAX. From their experimental work, they have the following conclusions:

- With more magnesium, the strength of the compact will grow from the longer CO_2 exposures. For example, the strength of the compact with only magnesium hydroxide will reach 70 MPa after 6 hours of CO_2 exposure.
- The compacts with high magnesium contents benefited more from increasing CO_2 pressure.

- Regarding long term strength, the sample with very high magnesium contents show no strength improvement at 28 days with the low CO_2 ambient environment.

1.3.4 Three-Dimensional and Four-Dimensional Printing Technology

With the help of computer-aided design, the three-dimensional (3D) printing technology is able to fabricate the complex shapes and structures from 3D model data (Gibbons et al., 2010; Shakor et al., 2017). Hambach et al. (2019) show that with an automatically 3D-printed composite of Portland cement paste and reinforcing short fibers, the resulting material exhibits excellent flexural strength (up to 30 MPa) and compressive strength (up to 80 MPa). Furthermore, the 3D printing technology could offer a possibility to provide the cement with various spatial and temporal ratios which could lead to a new self-adjusting material based on cellular materials with shape memory that induce adaptation according to thresholds such as temperature, pressure, or triggering chemicals (such as changing salinity). The “smart” capabilities of this material come from the freeform geometry of internal and external structures that 3D printing can fabricate, and also stem from its ability to combine different materials into one structure. For example, the excessive pore pressure caused by the changing boundary conditions will be drained by the well-designed internal poro-structures/channels that are difficult to construct with conventional techniques, while the external surface can still have ultra-low permeability to control the subsurface flow. By combining two types of materials with different, or even contrasting, properties during 3D printing, the different long-term deformation components (visco-elastic, visco-plastic) will be offset by different materials. This would hinder, or at least delay, wholescale plug failure, as compared to a stiff plug.

1.4 Current Placement and Verification Techniques for P&A

When considering the designs and operations of P&A, usually two general scenarios will be encountered: cased hole and open hole. The key element to distinguish these two cases is the qualification of the barrier behind the casing where it has to be examined. If it is qualified, then first a mechanical plug is placed to be used as a foundation for the cement to set. Then the cement plug is poured on top of the mechanical foundation and left undisturbed until it solidifies and develops strength (Khalifeh et al., 2020). Wherever the quality of the casing cement is not qualified, the cement and the casing of the previous phase, i.e. production phase, have to be removed by many different techniques, such as milling and cut-and-pull, and the plugging material is put in contact with the formation to achieve a cross sectional sealing.

Ideally, the open-hole run is considered to be the best practice of plug and abandonment because it builds a full cross-sectional barrier from rock to rock, and the zonal isolation is thus ensured. However, several other factors also influence the process and will eventually have an impact on the final quality of the P&A job. For example, the fluid (drilling or spacer) needs to be replaced along with the cement in the process of open-hole P&A, as severe contaminations can occur at the interface of drilling fluid and cement slurries due to incompatibility (Katende et al., 2020; Khalifeh et al., 2020). Thus, it is a crucial task to fully remove the drilling fluid from the open-hole interval and prevent it from exchanging with the cement or any other plugging material (Khalifeh et al., 2020). This contamination process can also occur in the cased hole. The swarf generated during the milling cannot be transported to the surface by the drilling fluids. Thus, one special fluid that usually is mixed with bentonite/bicarbonate mud, bentonite/mixed metal hydroxide, and xanthan gum/sea water mud will be used as the milling fluid to carry this debris to the ground (Ford et al., 1994; Messler et al., 2004; Offenbacher et al., 2018). These milling fluids can also cause contaminations to the cement slurries.

Once the barrier is established inside the well, verifications need to be done to check the cap rock restoration functionalities. Usually the annular barriers are tested indirectly by the sonic logging, whereas the cement plug along the well uses hydraulic pressure testing and weight testing (Achang et al., 2020; Acosta et al., 2017; Bois et al., 2019; Gong et al., 1992; Rouillac, 1994; Trudel et al., 2019). The hydraulic pressure testing applies pressure to the plugs, which are either installed inside the casing or installed entirely in open-hole. Depending on the direction of applied hydraulic pressure, there are two testing scenarios: positive pressure testing and negative pressure testing (Khalifeh et al., 2020). In the positive pressure test, the fluid pressure above the plug (P1) is higher than the pressure below the plug (P2). When the pressure difference reaches the requirement asked by the local authority, then this pressure will be monitored for a certain period of time (in minutes) and if the pressure is still stable, then this plug is considered to be a qualified plug. In the negative pressure testing, the pressure above the plug (P1) is decreased so the pressure below the plug (P2) will be higher than P1, and the pressure difference will be monitored for a period of time for verification purposes. There are some concerns associated with both forms of hydraulic pressure testing, one of the most important among them is that the pressure difference and the loading/unloading rate in both testing scenarios must be specified. Given the intrinsic porous nature of cement and the existence of pore fluid, any excessive amount of load and unnecessary rapid loading rate could cause the pore pressure to increase, which will put the plug at risk of tensile damage and shear damage.

1.5 Summary of Knowledge Gaps

Based on the literatures review above, the main knowledge gaps for P&A can be identified as follows. The P&A Codes and Standards solely serve as a recommendation provider to execute the requirements of the regulations issued by various local authorities. Following them can only meet the minimum requirements to maintain the P&A through design, planning, and executions. However, the long-term integrity cannot be guaranteed, since the current P&A codes and standards are missing many important aspects.

First of all, the high temperature, high pressure, acidic reservoir conditions, and mud contaminations are challenging and threatening to the performances of the commonly used oil cements (class H and G). These materials were initially designed for wells drilled at low pressure and temperature conditions, within competent formations, and with required service lives of 20-30 years. They are also not designed for geochemical compatibility with subsurface formations, so the stability over an extended period of time is unknown. When they are placed in high pressure high temperature (HPHT) formations, exposed to corrosive fluid, contaminated with drilling fluid, subjected to complex completions and stimulations, there is a substantial risk that the current wellbore barrier materials will be insufficient and it will cause leaky wellbores.

Secondly, while much effort has been focused on development of materials and additives to improve the performance of the Portland cement, the identification of what comprises “better” mechanical and hydraulic properties of cement are still unclear based on the definitions and information provided and defined by the current P&A codes. This is especially true for high temperature and high pressure (HTHP) environments. Wellbore cement can be classified as cementitious saturated porous material with permeability ranges from milli- to nano-Darcies. Such a material can be heavily influenced by thermo-hydraulic-mechanical (THM) coupling in the pore space, especially when it is experiencing large temperature and pressure variations. Within the permeability range mentioned above, a very large pore pressure could be induced by the THM coupling and the pore pressure would be progressively reestablished over the time, which would also lead to the changing of the effective stress and increase the possibility of shear failure, hydraulic fracturing, or even tensile failure.

Thirdly, the current placement and verifications techniques that are recommended by P&A codes are not specific enough, and these vacancies may lead to some detrimental effects during the P&A operations. For example, among many various P&A codes that are led by different local authorities, none has specified the pressure rate in loading/unloading in the pressure difference testing scenarios. Given the intrinsic porous nature of cement and the existence of pore fluid, any excessive amount of load and unnecessary rapid loading/unloading rate could cause the pore pressure to increase, which will put the plug at risk of tensile damage and shear damage. It will become even worse when the primary plug maintains the pressure difference for a certain amount of time and passes the pressure difference test. While everyone will consider it as a successful P&A job, no one will realize that the rapid unloading of the pressure difference already caused tensile damage inside the primary plug. Given the nature of the permanent P&A, no one will ever know that this “verified” work is actually malfunctioning at the very beginning of its service life in the geological timeframe and people will still wonder why oil and gas pollution keep occurring even when thousands of well have be plugged and abandoned.

1.6 Objectives and Scope of this Dissertation Research

Based on the knowledge gaps summarized above, the objectives and scope of this dissertation are stated as follows.

First of all, the harsh subsurface conditions of permanent plug and abandon (P&A) motivate development of new plugging materials that are able to thrive over the service time and span geological timeframes. Inspired by naturally-occurring geochemical processes, this research is aimed to demonstrate the feasibility of generating new cement-free plugging material that turns the often acidic geofluid, high-pressure, and high-temperature (AG-HP-HT) conditions of deep-water wells, which are detrimental to existing materials, into an advantage. The accelerated hydration and carbonation reactions turn granular ultramafic raw materials into competent rock, dubbed here as "Geologically Activated Cement" (GAC). The experimental details and results are presented in Chapter 2 in this dissertation. The results demonstrate that within the hours to days relevant to P&A operational timeframes, the magnesium silicate-based, solid, rock-like material can be produced from Mg_2SiO_4-CO_2 mixtures. Furthermore, the GAC can self-seal the damage when subjecting it to flow of acidic fluid under HPHT conditions within a few hours, which provides the potential for a resilient cementing system.

Secondly, with the aid of a new semi-analytical solution for thermo-poro-elastic (TPE) stresses in a cylindrical cement plug that includes consideration of full coupling between hydraulic and thermal transport models (so-called “porothermoelastic-osmosis-filtration”, or “PTEOF” model), this work is aimed to find the optimal mechanical, hydraulic, and thermal properties of Portland cement under HPHT. The solution details and results are presented in Chapter 3 in this dissertation. Briefly, our results shows that lower permeability is not always better for cementing under HPHT. The solution shows that materials that are unable to drain excess pore pressure quickly enough compared to the rate at which these pressures build due to thermal changes, are more prone to generate regions of internal tensile effective stress and hence are more likely to be damaged. The specific parameter groups associated with this newly identified "permeability penalty" are obtained through a combination of dimensional analysis and pairwise bivariate analysis. These approaches give rise to two dimensionless groups of parameters that are mainly associated with propensity to generate TPE tensile effective stresses. The parametric space defined by these two groups is shown to have three distinct regions based on the probability of generating tensile effective stresses in a plug with a given set of material properties. By shifting the focus of material design from achieving the lower possible permeability to instead achieving the lowest permeability that will not incur increase likelihood of failure due to pore pressure buildup, this work provides a new design concept for wellbore cement. Furthermore, this work highlights for the first time the important role of specific heat of the cement in preventing pore pressure buildup, thereby showing a new way forward for cement design to increase this quantity.

Thirdly, the lack of guidance regarding the loading/unloading rates during the plug verification phase in the P&A codes motivates this research to demonstrate that within the current cement hydraulic and mechanical properties, an excessive amount of load and unnecessary rapid loading/unloading rate, or even temperature change, could cause tensile damage to the cement plug, due to the trapped and increased pore pressure. These experiment details relevant to this issue are presented in Chapter 4, which presents an experimental demonstration of a novel mode of failure that could be very commonly encountered in a full life span of wells that undergo rapid temperature and/or pressure cycling. It shows that if a material's creep deformation is rapid enough compared to its ability to dissipate pore pressure build up, then it will be prone to fail through the generation of regularly and predictably spaced periodic cracks. This is the first demonstration of such cracking under conditions relevant to P&A operations. Overall, the intent is that these findings make P&A researchers and practitioners reevaluate the current technical details in the P&A codes and therefore will make future P&A a more reliable work in the geological timeframe.

2.0 Experimental Study of Genesis of a Geologically Activated and Self-Sealing Cementing Material for Deep Wellbore Plugging and Abandonment

2.1 Chapter Summary

The harsh subsurface conditions of permanently plug and abandon (P&A) motivate development of new plugging materials that are able to thrive over the service time spans geological timeframes. Inspired by naturally-occurring geochemical processes, this research demonstrates the feasibility of generating new cement-free plugging material that turns the often acidic geofluid, high-pressure, and high-temperature (AG-HP-HT) conditions of deepwater wells, which are detrimental to existing materials, into an advantage. The accelerated hydration and carbonation reactions that turn granular ultramafic raw materials into competent rock, dubbed here as "Geologically Activated Cement" (GAC). The results demonstrate that within the hours to days relevant to P&A operational timeframes, the magnesium silicate-based, solid, rock-like material can be produced from Mg_2SiO_4-CO_2 mixtures. Furthermore, the GAC can self-seal the damage when subjecting it to flow of acidic fluid under HPHT conditions within a few hours, which provides the potential for a resilient cementing system.

2.2 Introduction

When oil and gas wells are at the end of their service lives and no longer economically viable for production, it is required that they be safely plugged before permanent abandonment (Vrålstad et al., 2019). The key goal of this plug and abandonment (P&A) is to permanently isolate all of the formations that are penetrated by the well. It requires setting up multiple plugs along the well. These plugs control the subsurface fluid flow, preventing fluids from migrating along the wellbore over time. The plug also protects the casing from acidic fluids and mechanical impact (Norge, 2013; Oil et al., 2015). However, for deep wells, especially those encountered in deep-water offshore environments, as shown in Figure 4 Illustration of four main factors (high temperature, high pressure, acidic fluid, and drilling mud contaminations) that are threating the integrity of well barrier material in geological time frame., mainly four harsh subsurface conditions include high-temperature, high-pressure, the presence of acidic fluid, drilling mud contamination pose a threat to the integrity of traditional materials (Ahmed et al., 2020; Allahvirdizadeh, 2020b; Kiran et al., 2017). As a result, pursuing a new and improved cementitious material to remediate wellbore leakage has become urgent and necessary.

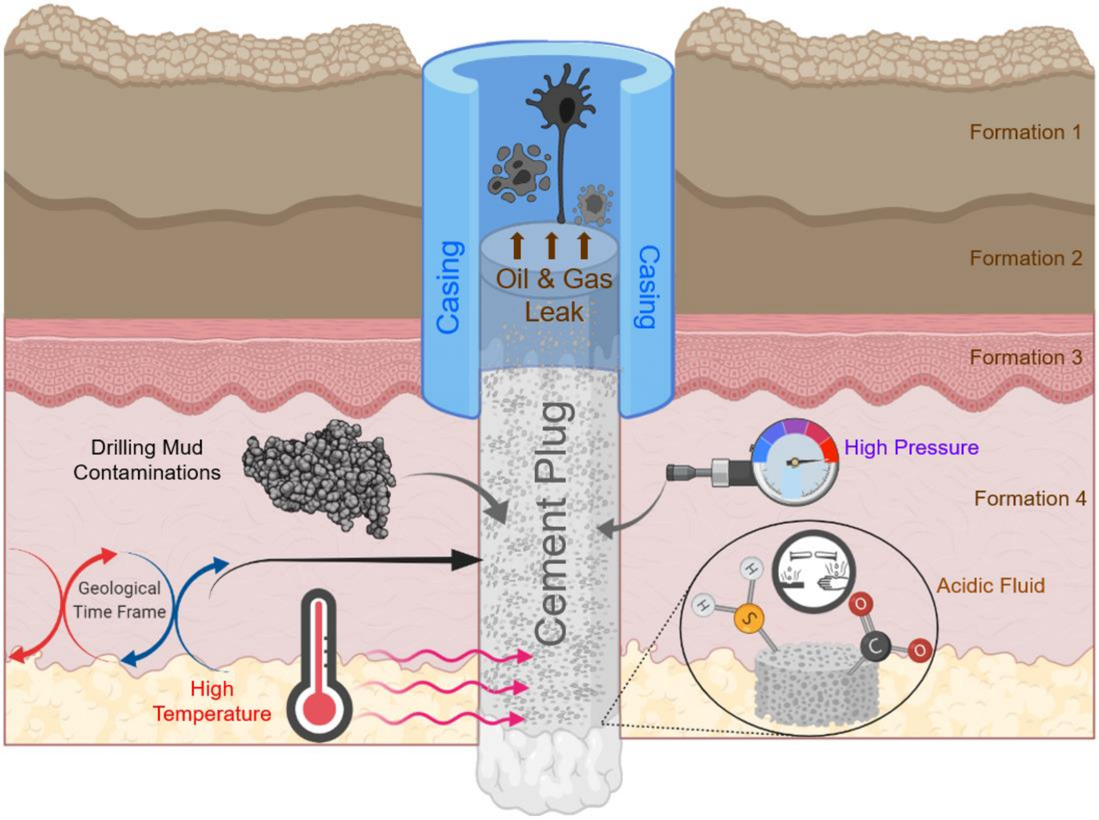

Figure 4 Illustration of four main factors (high temperature, high pressure, acidic fluid, and drilling mud contaminations) that are threating the integrity of well barrier material in geological time frame.

There is currently a growing interest in developing deep-water P&A technologies. This interest is not only because of an increasing number of deep-water wells waiting to be plugged and abandoned (Aarlott, 2016), but also due to the inadequate performance of the currently-available plugging materials. Although Portland cement (class H and G) is by far the most commonly used plugging material for the offshore abandonment in the worldwide, these materials were initially designed for wells drilled at low pressure and temperature conditions, within competent formations and with the required service life of 20-30 years (Corina et al., 2019b; Ingraffea et al., 2014; Vrålstad et al., 2019). Portland cement is also not designed for geochemical compatibility with subsurface formations (Bachu et al., 2009; Barlet-Gouédard et al., 2009; Maurice B. Dusseault et al., 2000), so the stability over an extended period of time is unknown. When placed in high pressure and high temperature (HPHT) formations, exposed to acidic geofluid (AG), and/or contaminated with the drilling fluid, there is a compounding risk that the current wellbore barrier materials will be insufficient and therefore will allow leakage through the abandoned wellbores (Beltrán-Jiménez et al., 2019a; Jiang et al., 2019; Katende et al., 2020b; Li et al., 2019; Shadravan et al., 2014). The issue is complex because the leakage pathways could occur at multiple locations along the well and could include damage to the vulnerable interface between the reservoir formation and cement plug (Carroll et al., 2016; Kiran et al., 2017). The microscopic scale of these pathways can make them difficult to locate and mitigate (Norge, 2013).

Current industry practice and regulatory guidelines most likely can reduce leakage of fluids along wellbores, but true prevention remains an unattained goal. By increasing the minimum length of the primary plug and setting multiple well barriers, the expectation is these leakage paths could be reduced and the integrity of the P&A system should be strengthened. However, these two measures fall short of truly prevening leakage of the well, particularly if there is degradation of the plugging material. Furthermore, if plugging fails, remediation is difficult and expensive, and the damage to the environment which is caused by the leaky well can be extensive (Barclay et al., 2001). So it is of utmost importance to seal the well correctly with a material that resists decay of its performance and is able to naturally restore performance even if chemical, thermal, and/or mechanical assault causes it to be compromised at some point during its service life.

There is a wide distribution of severity of consequences of failure of a wellbore plugging and sealing system. Many lessons can be learned from perhaps the highest consequence event in the history of the industry, the Deepwater Horizon oil spill at Macondo (Bly, 2011; Group, 2011; Summerhayes, 2011). This experience shows that even when the P&A system has several wellbore barrier elements, if one of them fails to carry out its function properly, the balance of the whole system can be broken by the accumulative effects, which can accelerate the degradation of the system or even lead to the system failure. Therefore, when considering the next generation of barrier materials for P&A, the ideal barrier material not only needs to overcome the challenging conditions but also needs to have resilience. The concept of resilience is often used in the structural engineering discipline to evaluate the performance of structures after they experience an event such as an earthquake (Bruneau et al., 2003). In P&A, the proposed resilience is focused on the plugging material's self-restoration or self-sealing behavior. When the barrier in the P&A is damaged, it will lose its integrity and the permeability will become larger than prior to the damage. As fluid flows through the material, based on the Darcy's law where permeability can be calculated from flow rate (q), specimen length (l) and pressure drop (Δp), the permeability can stay the same with time t (stable damage), increase with time t (growing damage), or decrease with time t (sealing damage). The latter case comprises resilient behavior and will be taken as evidence of self-sealing within the material (Figure 5).

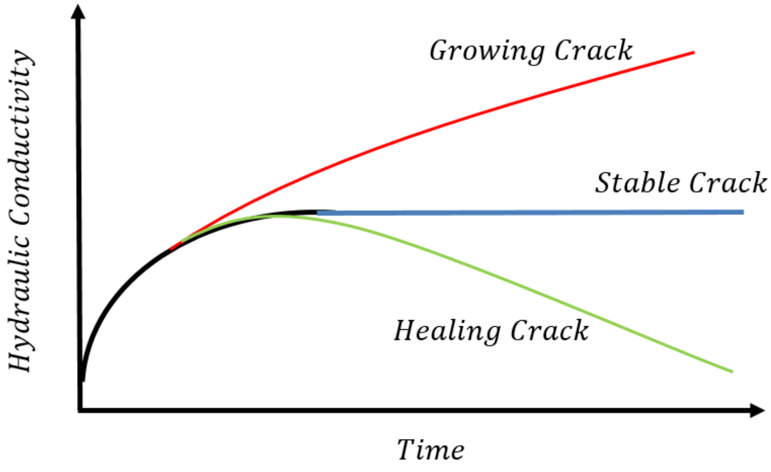

Figure 5 Conceptual illustration of three potential outcomes of permeability evolution of a material that has been damaged, where the reduction with time indicates a resilient response to the damage.

Resilience is difficult to attain with Portland cement-based systems because the properties tend to naturally degrade in acidic environments (Gutberlet et al., 2015). Furthermore, the material has only existed for a short time, geologically speaking, and so there is no relevant data on its performance over geological timescales. On the other hand, many geological materials naturally undergo alterations and many of these result in cemented rocks which have been discovered to be stable under acidic hydrothermal conditions for millenia. Inspired by work on the reaction kinetics associated with the geochemical alteration of ultramafic minerals (Kelemen et al., 2008), the present work focuses on one of these, investigating the feasibility of inducing nature-mimicking carbonation and hydration reactions of ultramafic rocks under wellbore conditions to generate a material that is stable and self-sealing.

Drawing on reaction pathways and kinetics of silicate dissolution and subsequent carbonate precipitation (Lisabeth et al., 2017; Zhu et al., 2016), the principle of the new “Geologically Activated Cement” (GAC) is to place ultramafic minerals, such as olivine, into the wellbore and allow them to hydrate and carbonate in-situ. This approach is a form of so-called "cap rock restoration", novel in that it utilizes geochemical alterations that are ubiquitous, but typically too slow for engineering applications. However, Kelemen and Matter (Kelemen et al., 2008) show that certain temperature-pressure conditions, serendipitously very similar to HPHT reservoirs associated with many deep-water wells, result in drastic speed up of the relevant reactions (Figure 6) such that processes that would take tens of thousands of years at surface conditions could occur within one day under AG-HP-HT deep-water well conditions. Hence, leveraging this nature-inspired reaction turns challenging AG-HP-HT conditions into an advantage. Furthermore, it hypothesizes that reactions will occur at the surfaces of granular olivine, leaving a cemented material with unreacted olivine at the particle cores. This unreacted material is expected to remain available to carbonate or hydrate in a manner that is restorative, sealing cracks that form as a result of damage to the material during its service life. This work is therefore aimed at proof-of-concept for genesis of GAC and testing the hypothesis that such a material will exhibit self-sealing behaviors under simulated AG-HP-HT, deep-water well-like conditions.

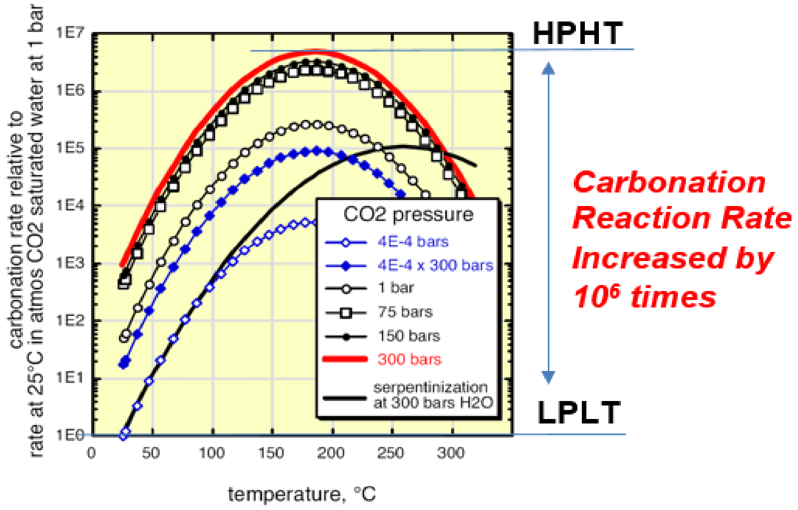

Figure 6 Relative increase in carbonation rate of olivine at elevated pressure and temperature compared to surface conditions (after Keleman and Matter 2008, with permission).

2.3 Experimental Procedures

2.3.1 Genesis of GAC Materials

The first objective is the initial exploration of the conditions enabling the necessary reactions to occur at the relevant engineering timescale. The goal is to provide demonstration of pressure, temperature, and fluid chemistry to obtain the desired alteration products.

The apparatus used to generate GAC material at elevated temperatures and pressures is shown in Figure 7 Left. The syringe pump at the upstream side can provide the pressure up to 68.94 MPa (10,000 psi). The stainless-steel reactor with 203.3 mm length and 15.7 mm internal diameter has a cap at the downstream end and so behaves as a closed system. The external heating is provided by an oven that enables the specimen to be heated up to 250°C. Sodium bicarbonate, which is used as the CO_2 source, will undergo a decomposition reaction and start to produce CO_2 when the temperature is above 50 °C. As the temperature increases, the reaction goes to completion, with the decomposition of all the sodium bicarbonate ($2NaHCO_3$ (s)$\rightarrow Na_2CO_3$(s) + $2H_20$ + CO_2(g)). The chemical composition of olivine fine particles used in the experiment is 90.7% Mg_2SiO_4, 7.6% Fe_2SiO_4 and 0.27% Al_2O_3. Its size distribution is determined by sieving and selecting particle sizes less than 0.075 mm.

In this system, the dissolution and precipitation reaction can be represented by the following steps (Gerdemann et al., 2007; O'Connor et al., 2005a):

$$\mathrm{CO_{2(g)} = CO_{2(aq)}} \tag{2-1}$$

$$\mathrm{CO_{2(aq)} + H_2O = CO_3^{2-} + 2H^+} \tag{2-2}$$

$$\mathrm{Mg_2SiO_{4(s)} + 4H^+ = 2Mg^{2+} + H_4SiO_4} \tag{2-3}$$

$$\mathrm{Mg^{2+} + CO_3^{2-} = MgCO_{3(s)}} \tag{2-4}$$

$$\mathrm{2CO_{2(aq)} + 2H_2O + Mg_2SiO_{4(s)} = 2MgCO_{3(s)} + H_4SiO_4} \tag{2-5}$$

Here the system consists of dissolution and hydration of CO_2 in water (equation 2-1 & 2-2), the dissolution of silicate minerals using magnesium silicate as an example (equation 2-3), and the precipitation of carbonate (equation 2-4). If we add the first four equations, then it yields a net aqueous carbonation reaction, which is represented by equation 2-5.

The experimental procedures are as follows: firstly, the fine olivine particles and sodium bicarbonate are thoroughly mixed. Secondly, each ingredient is prepared under the ambient atmosphere and temperature based on the proportion information provided in Table 2. Note that based on the stoichiometric calculations implied by equation 2-1 to 2-5, the ideal ratio of bicarbonate of fine olivine particles should be 2.4:1. In present experiment work, this ratio is increased to 4.8:1 in order to increase the carbonation level of the fine olivine particles. Then, the reactor is loaded by the solution with a volume of 39.2 mL, which is its full capacity. When the reactor is sealed, the oven is turned on to 180°C and the upstream pressure is adjusted to 13.79 MPa (2000 psi). After 24 hours of HPHT curing, the post-reaction products are taken out from the system after releasing the pressure and turning off the oven.

Table 2 Summary of proportion of each ingredients for carbonation reaction

	BB/OFP	DW/OFP	Water to Solid Ratio
Based on Stoichiometry	2.4	0.25	0.07
In Present Work	4.8	0.5	0.08

*OFP = olivine Fine Particles; Bicarbondate = BB; Distilled Water = DW;

The product is observed and analyzed under Scanning Electron Microscopy (SEM) and Energy Dispersive Spectroscopy (EDS). To improve the image quality, the samples were carbon-coated prior to SEM/EDS analysis. Images, maps, and spectra were obtained at 20 KeV, and various magnifications, from a larger field of view to a higher magnification that reveal characteristics of the interfaces and surface properties of the new generated cementitious material.

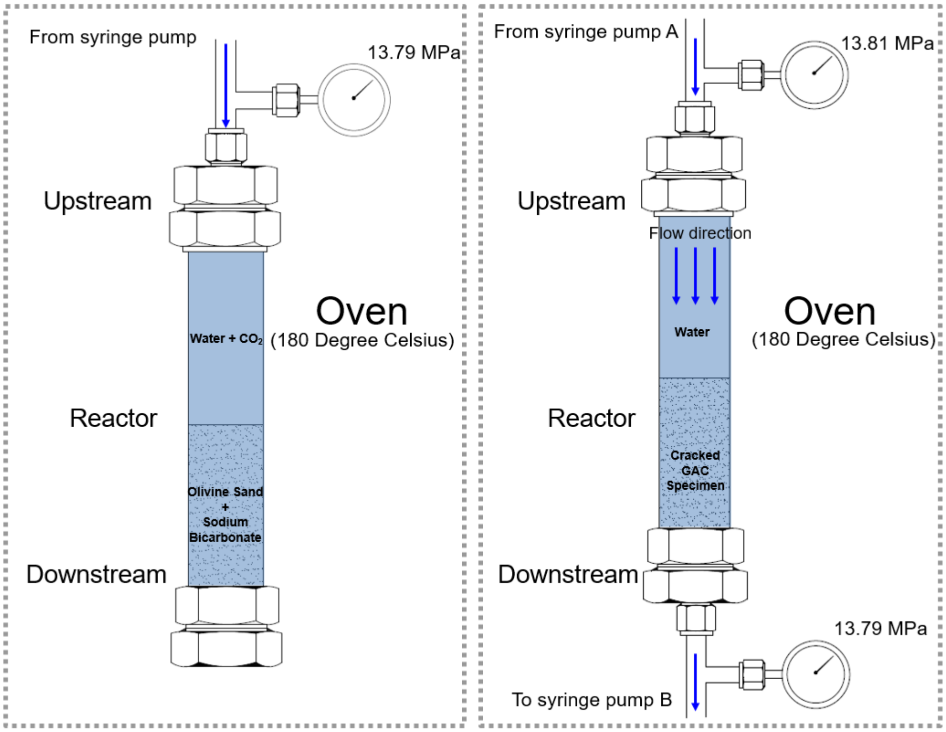

Figure 7 Left: laboratory setup for carbonated olivine generation; Right: experimental setup for the self-sealing test.

2.3.2 Self-Sealing of GAC Materials

The second objective is to test the self-sealing hypothesis for the GAC by measuring the evolution of permeability of damaged GAC subjected to flow of fluid under wellbore-like conditions. The experiments entail firstly inducing damage to the GAC, that is, inducing cracks. Thermal shocking was found to be the most convenient because it does not require removal of the GAC from the steel tube in which it is generated. It was also found that, by carefully repeating the same procedure, the crack widths generated by the thermal shock could be reasonably consistent from one test to another, ranging 0.1 to 1 mm. Several methods were explored, but the most effective was found to be pouring boiling water on the room temperature specimen (which includes the stainless steel tube).

After inducing cracking, the self-sealing experiments are performed with a wellbore-analog setup, which is illustrated in Figure 7(right). The reactor loaded with cracked GAC is placed inside an oven. Pressure is applied at both ends of the reactor by two syringe pumps. The instrumentation on these pumps enables monitoring and recording the change of pressure and flow rate in the system.

Before a self-sealing test is started, the upstream pressure and downstream pressure are both increased to 13.79 MPa and the oven is set to 180 ℃. This is followed by a brief (60-90 minutes) waiting period for the temperature of the specimen to equilibrate to the oven temperature. After that, the pressure at the upstream is increased from 13.79 MPa to 13.81 MPa. This pressure difference will drive the fluid flow to penetrate the cracked specimen and flow to the downstream end of the specimen. Immediately after the upstream pressure is increased, the flow rate is monitored and measured using the downstream syringe pump displacement. The testing time for the self-sealing of GAC usually takes 10 to 20 hours. The pressure at upstream and downstream ends remain unchanged during testing, controlled independently by two syringe pumps. As the control group, the class-H cement is cured in the same HPHT reactor and is tested under the same experimental conditions as the GAC. Besides control experiments with Class H cement, two types of self-sealing tests are performed where the fluid is taken alternatively as carbonic acid (pH~3) and distilled water with anhydrous citric acid (pH~4).

2.4 Results

2.4.1 Genesis of Geologically Activated Cementing Materials

As shown in Figure 8, the initially loose olivine fine particles (Figure 8a) with the maximum particle size less of 75 microns, has been turned into solid material. Recall this end product is obtained after subjecting the mixture of olivine sand, water, and the CO_2 source (in this case degenerating sodium bicarbonate) to 13.79 Mpa (2000 psi) of pressure and 180℃ of temperature for 24 hours. This cementitious and hardened solid becomes firmly lodged in the reaction chamber (Figure 8b), which is expected because the overall is accompanied by volumetric increase (Kelemen et al., 2008; Zhu et al., 2016).

From the decomposition reaction $2NaHCO_3(s) \rightarrow Na_2CO_3(s) + 2H_20 + CO_2(g)$, we can see that the $Na_2CO_3(s)$ will remain in the post-reaction system as a residue. This residue is in addition to the reaction products. To exclude the possibility that $Na_2CO_3(s)$ is contributing the binding ability in GAC, another control group test was performed. It entails repeating the same test procedures described above but replacing the fine olivine particles with the same size of silica sand particles. At room temperature, the solubility of the magnesium carbonate is 1.06e-2 g/100 ml whereas the Na_2CO_3 is 7.1 g/100 ml. The huge difference between the solubilities provides a method by which to distinguish magnesium carbonate and sodium carbonate through a test of solubility performed on the products from the olivine sand mixture system and the silica sand mixture system.

The olivine GAC material is created as described above. The contrasting system using silica sand is produced using the same method. The result is a slurry like material after taking out of the reactor.

Both products are submerged in water and stirred for ten minutes. The pre-stir mass and post-stir mass are recorded in Table 3. The mass of magnesium carbonate cementing material from the olivine system does not change at all after stirring. However, the product from the silica sand mixture system is completely dissolved in the water. We see, then, that Na_2CO_3 binder dissolves rapidly, and the binder for the olivine-based GAC does not measurably dissolve, and thus the results from the solubility test exclude the possibility that Na_2CO_3 is the binder in GAC.

Table 3 Results of the solubility test.

	Mass of solid (pre-stir)	Mass of solid (post-stir)
Products from olivine system	1.9 g	1.9 g
Products from silica sand system	1.5 g	0.0 g

While solubility provides evidence that Na_2CO_3 is not the binder, it is worthwhile to explore in more detail to ascertain the composition of the GAC binder. Taking part of the GAC material and analyzing it under XRD shows that the product is a mixture of magnesium carbonate ($MgCO_3$) and remaining fine olivine particles (Figure 9). It demonstrates that within the timeframe of hours to days, i.e. relevant to P&A operations, the system of fine olivine particles (Mg_2SiO_4) and CO_2 at temperatures and pressures relevant to the challenging conditions of the deep-water well, has the ability to produce sandstone-like material which is cemented by magnesium carbonate. At the same time, the dissolution-precipitation reaction in this sandstone-like material has not completed yet within this timeframe, which leaves unreacted Mg_2SiO_4 particles widely distribute in the GAC and thus providing the material needed to repair further damage by generating new carbonate binder through reapplication of the carbonation reaction.

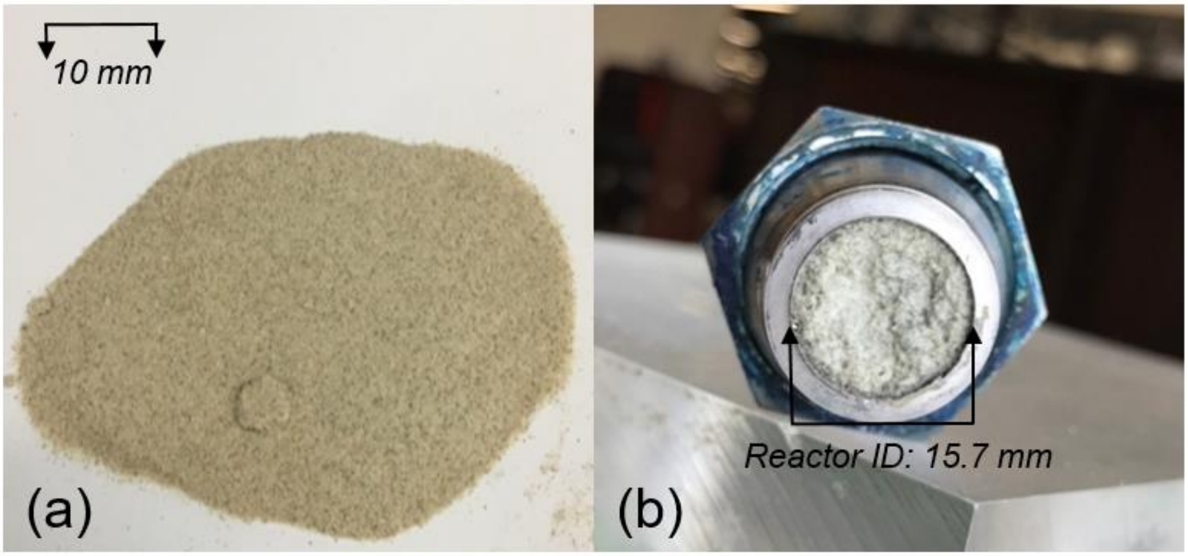

Figure 8 (a) Pre-reaction: loose olivine sand; (b) post-reaction: hardened carbonated masses in the reactor.

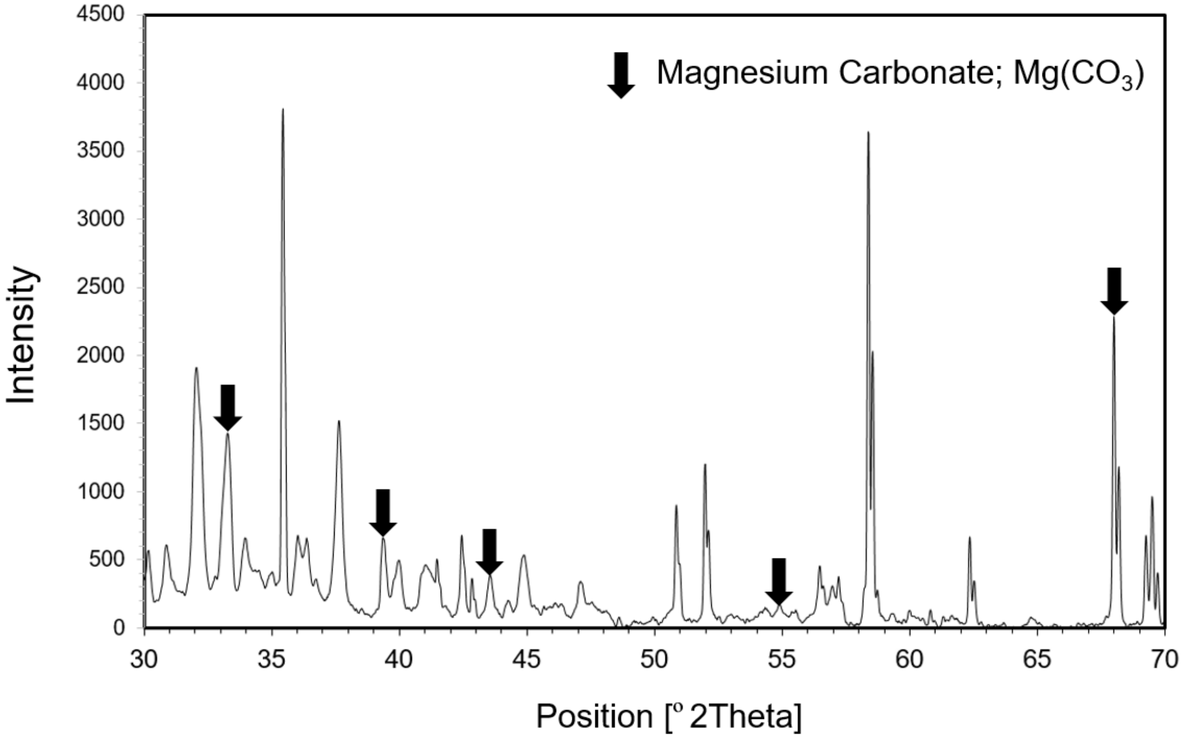

Figure 9 The results of XRD of the reaction product (the black color arrow labels on the are the reference locations of different phases of Magnesium Carbonate in the Power Diffraction File (PDF)).

To better observe the GAC microstructure and indentify the elemental composition of the materials, GAC is then put under SEM and EDS, as shown in Figure 10 (~600 microns across). The GAC is shown to be comprised of olivine particles bonded together by a material that almost certainly is magnesium carbonate ($MgCO_3$). The analysis leading to this conclusion begins with selection of several points in Figure 10 for elemental analysis (EDS). The EDS results for the selected points and their element spectrums (percentage by weight) are shown in Figure 11. From these data, clearly different chemical compositions can be found among the five selected points. For example, the point 1 does not contain any C (Carbon) but is rich in O (Oxygen), Mg (Magnesium) and Si (Silicon). Thus, it is inferred to be magnesium silicate (Mg_2SiO_4). However, points 4 and 5 contain C (Carbon), O (Oxygen) and Mg (Magnesium), but without any Si (Silicon). So they are inferred to be the carbonation reaction product of magnesium carbonate ($MgCO_3$). For points 2 and 3, they are containing the C (Carbon) and Mg (Magnesium)/Fe (Iron) at the same time, which is taken to imply they consist of product of mixture of carbonated and unreacted olivine.

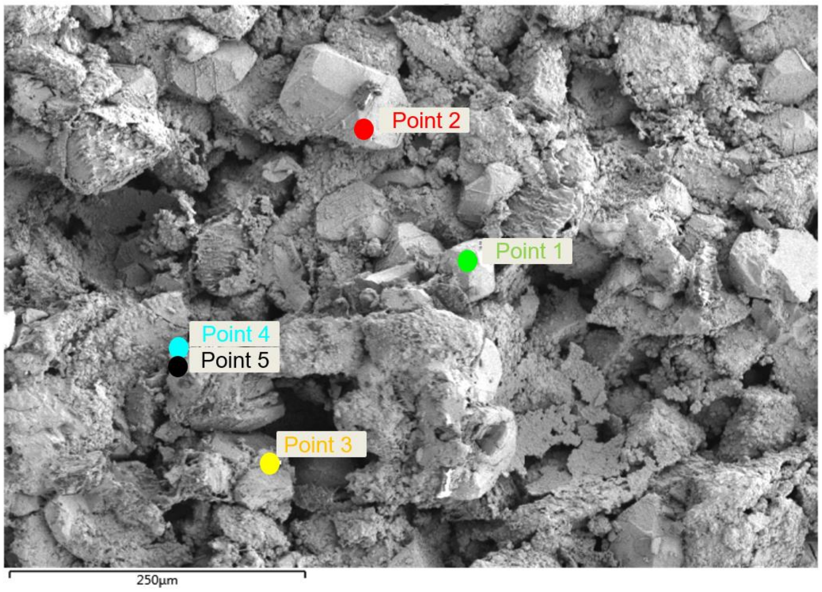

Figure 10 Post-reaction products under SEM and point 1-5 are selected for EDS analysis.

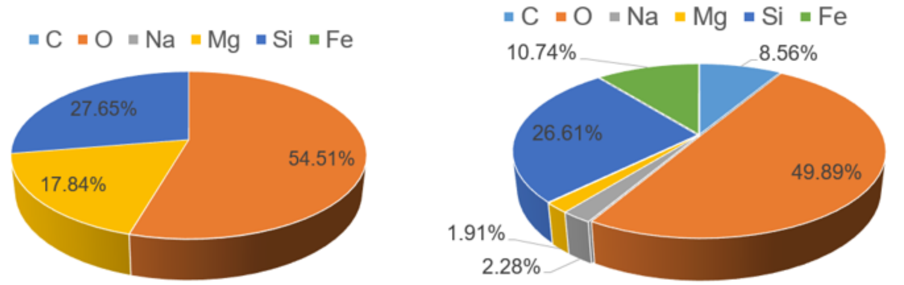

(a) Elemental Composition of Point 1

(b) Elemental Composition of Point 2

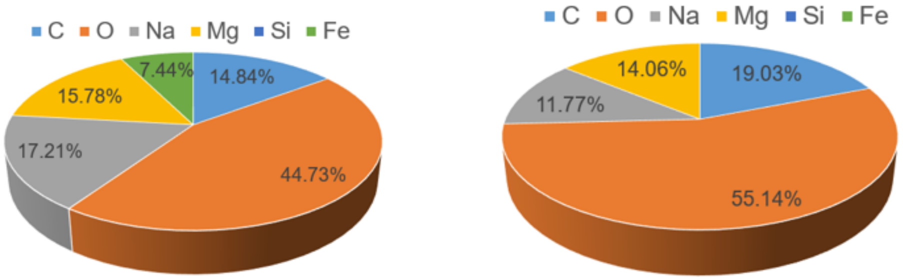

(c) Elemental Composition of Point 3

(d) Elemental Composition of Point 4

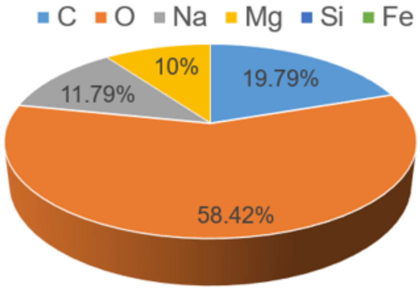

(e) Elemental Composition of Point 5

Figure 11 Element spectrum of selected points in Figure 10.

2.4.2 Self-Sealing Behavior

With the proof-of-concept for genesis of GAC established, the attention turns to behavior of the material when it is damaged and as it subsequently interacts with flowing fluids. The overall idea is to compare GAC with class-H cement to determine if it is prone to increasing permeability or decreasing permeability with time. The scenario in which the permeability increases with time is taken to imply that, once it is initially damaged, fluid interaction with the material further degrades it as a plugging material. The scenario in which the permeability decreases with time is taken to imply resilience of the material in that it is able to heal the damage and self-restore as a competent plugging material.

Both fluids used in the study of self-sealing have a low pH. The first is citric acid and the second is carbonic acid, with the latter a common cause for low-pH fluids in the subsurface including deep-water wells. As previously described, for each self-sealing experiment, the flow rate was recorded as it evolved in time in response to a fixed pressure difference at the two ends of a pre-damaged sample. Based on the flow rate and pressure difference, the permeability is computed according to Darcy's law as equation 6 (Verruijt, 2016), where k is the intrinsic permeability (m^2), q is flow rate (m^3/s), μ is the viscosity (Pa · s), L is the sample length (m), A is cross-sectional area of flow (m^2) and Δp is pressure drop (Pa)

$$k = q \times \mu \times L/(A \times \Delta p) \tag{2-6}$$

The evolution of the flow rate is therefore used to ascertain evolution of the permeability of damaged class-H cement and GAC specimens. The results are shown for these two materials in Figure 12(a) and Figure 12(b), respectively. The results firstly show that the class-H specimen exhibits permeability that is increasing with time. As shown in Table 4, the flow rate of water through the damaged class-H specimen is increased by 70%, from 0.024 ml/min to 0.041 ml/min after six hours of core flooding with citric acid under HTHP conditions. This increasing permeability with time corresponds to the "unstable" behavior (Figure 5) and suggests that baseline class-H cement is not resilient when subjected of damage and subsequent flow of acidic fluid.

In contrast to the unstable behavior of class-H cement, Figure 13(b) shows that the permeability of GAC is decreasing with time with flooded with citric acid under HTHP testing conditions. As detailed in Table 4, the GAC specimen undergoes a reduction of flow rate (and hence permeability) of about 75% (Figure 12(b)). The GAC therefore demonstrates resilience when subjected to damage and the experimental results provide evidence for the capacity of GAC to self-heal when subjected to injection of citric acid under HTHP conditions.

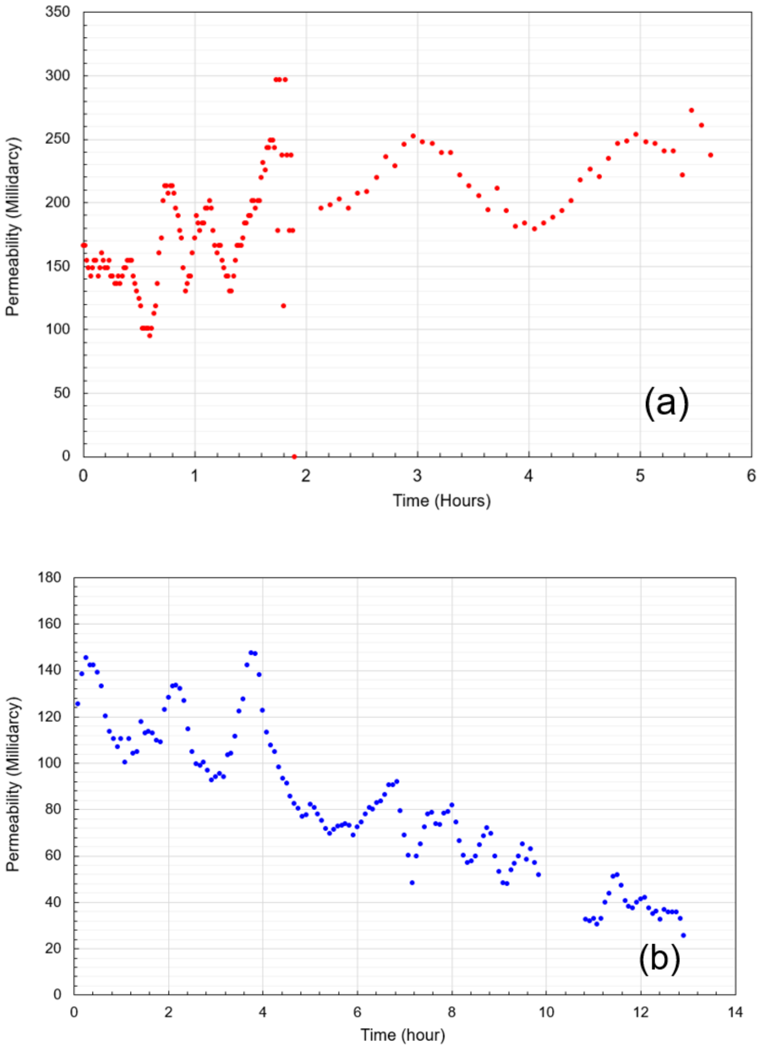

Figure 12 (a) permeability change of class H cement during HPHT self-sealing tests (citric acid group); (b) permeability change of GAC during HPHT self-sealing tests (citric acid group).

Similar behavior is observed for injection of carbonic acid under HPHT conditions. Specifically, the class-H cement again shows increasing permeability with time by about 50% after 7 hours of testing (Figure 13(a)). Again, this unstable behavior suggests that the class-H cement does not self-restore the damage when subjected to carbonic acid at HPHT conditions. Of course this only considers the first few hours, and other modes of self-restoration could be relevant on longer time scales. But, it could also be argued that if the material becomes damaged, restoration on the timeframe of hours is a desirable characteristic of a material, and on this time frame, class-H cement evolves in the direction of increasing rather than decreasing permeability.

Once again, and in contrast to the class-H cement, the GAC shows decreasing permeability when subjected to carbonic acid flowing through under HPHT conditions. As shown in Figure 13(b), the permeability of cracked GAC decreases from around 130 mD to 68 mD after 12 hours, giving an roughly 50% reduction relative to the initial permeability and demonstrating self-repair of damage within hours.

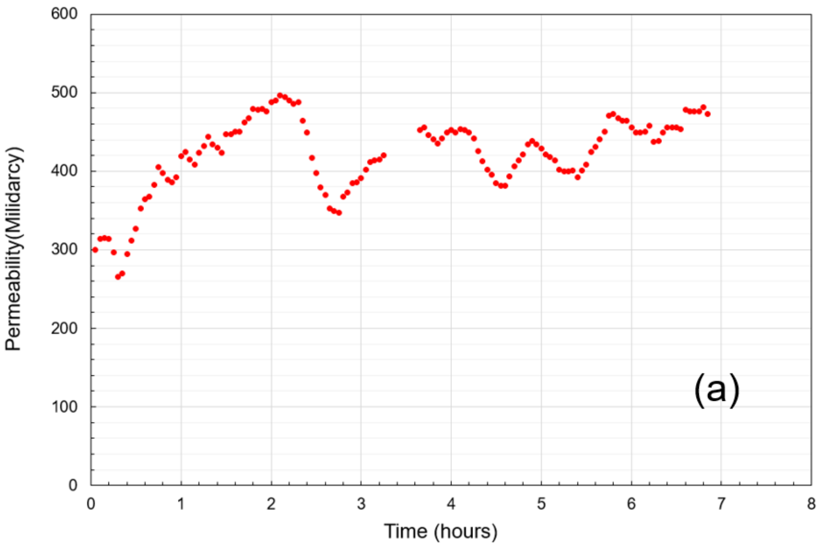

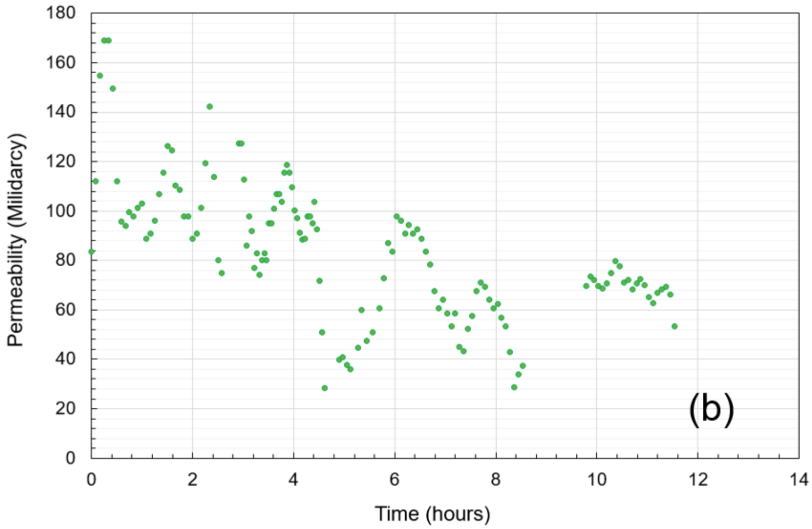

Figure 13 (a) Permeability change of class H cement during HTHP self-sealing tests (carbonic acid group);(b) permeability change of GAC cement during HTHP self-sealing tests (carbonic acid group).

Table 4 Self-sealing data of class H cement and GAC under HTHP testing conditions

Acid source	Specimen name	Testing time (hours)	Initial flow rate (ml/min)	Final flow rate (ml/min)	Initial Permeability (mD)	Final Permeability (mD)	Permeability change percentage	Tendency
Citric acid	Class-H	6	0.024	0.041	150	260	+73%	Unstable
	GAC	13	0.107	0.026	144	36	-75%	Sealing
Carbonic acid	Class-H	7	0.085	0.1275	300	450	+50%	Unstable
	GAC	12	0.022	0.011	130	68	-47%	Sealing

2.5 Discussions

2.5.1 Binding Mechanism of GAC

The binding mechanism of GAC is inferred from XRD and EDS compositions and SEM microstructure. It is conceptually illustrated in Figure 14. Before the carbonation reaction, the CO_2

is firstly dissolved in the water to form the carbonic acid (pH 3~4), which is represented by equation (2-2). The carbonic acid is surrounding the magnesium silicate (MS) in the form of a film around the particle. Although the dissolution-precipitation reaction is already happening at this moment, it is at an extremely slow rate (in the timeframe of geological time). However, once the pressure-temperature contains an ideal range (180℃ and 13.79 MPa in our proof of concept), the rate of dissolution-precipitation reaction will be dramatically increased. Then, the periphery of the olivine particle is carbonating first and the reaction product of the carbonation will surround the MS particle until it completely covers it. The magnesium carbonate (MC) is not only functioning as the binder among the each particles to form the hardened solid product, but also is the main strength source of the GAC. Furthermore, the generated MC is also filling the pore space between the MS, which causes the reduction of the pore volume and leads to denser structure. As shown in previous studies (Chizmeshya et al., 2007b; Lisabeth et al., 2017; O'connor et al., 2005b), there will be volume expansion occurring during the olivine carbonation rection. However, due to the limitations of the current experimental setup, how much the volume is expanded and what was the expansion induced stress remains a topic for future investigation.

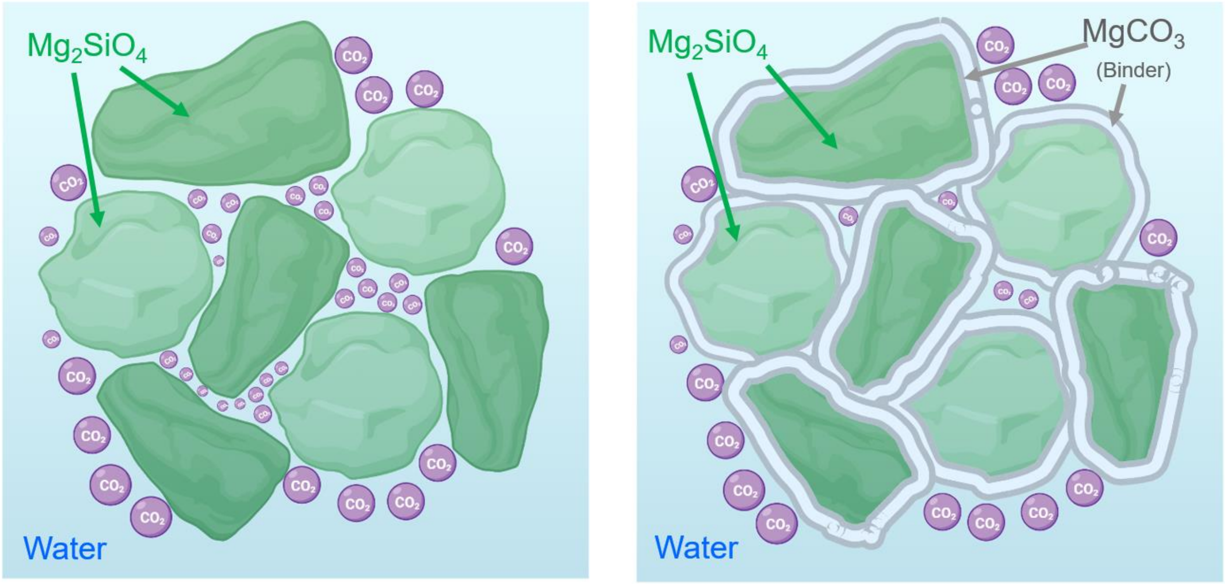

Figure 14 Inferred binding mechanism of Geologically Activated Cement material.

2.5.2 Self-Sealing Mechanism of GAC

The self-sealing mechanism is inferred to rely on the unreacted olivine particles that are shown by SEM-EDS to be widely dispersed in the GAC (recall Figure 10). In fact, XRD further shows that the proportion of olivine that is reacted in the original GAC formation is relatively small, leaving a large amount available for future reaction. So, in the presence of acidic fluid and under HPHT conditions, the rate of hydration-carbonation reaction of remaining olivine particles will be rapid enough to enable effective sealing of the breakage flow paths using the products from the mineral carbonation reaction (mainly magnesium carbonate). Specifically, because of the presence of a carbon source (i.e. carbonic acid), there is a supply of CO^{2-} ions. Additionally, because of the HPHT conditions, the Mg^{2+} ions will be continuously released via dissolution of unreacted olivine. Thus, the self-sealing of GAC could be achieved many times owing to a large source of Mg^{2+} and CO^{2-}. When present, movement of these ions is presumably by a combination of advection as well as diffusion that is driven by the concentration difference. Hence, when damage occurs and the precipitation reaction begins repair, the ions locally deplete as they form solid reaction products. But, subsequent movement of Mg^{2+} and CO^{2-} will be impacted by the concentration difference, leading reactants to repair locations where cracking has exposed to the fresh olivine. By this process, the fracture will be sealed by the new binder $MgCO_3$ which is generated from the carbonation reaction.

2.5.3 Carbonation Level and Reaction Rate

Using carbonation to activate binders is not new. Indeed, natural formation of carbonate binders is one of the most common geochemical processes that occurs in nature. Representing various reactants, products, and processes, rock that owe their binding to carbonate formation include limestone, beachrock, dolomite, and magnesite. All of them are considered as the main rock-forming carbonate minerals in nature and proven to possess chemical and physical properties that allow the rock to remain competent for millions of years (Ashraf, 2016; De Silva et al., 2006; De Silva et al., 2009). While drawing inspiration from these systems is a starting point for developing cap rock restoration systems that are intended to seal for millions of years, the ubiquitous problem is that these natural geological processes occur over geological time scales that greatly exceed the time scales needed for engineering applications. Thus, for practical engineering purposes, how to enhance the carbonation level and reaction rate to create natural carbonate like binders in a short time is a recurring research theme (Gerdemann et al., 2007; Power et al., 2013). In the context of using GAC as the barrier material, the ongoing issues will be to reduce permeability and bound the range of fluid flow rate for which self-sealing is still effective. Some considerations for both of these ongoing objectives are briefly described in this section.

Under our current experimental conditions, the permeability of GAC is falling into the range of 10-500 milidarcy after 24 hours of reaction, which is equivalent to the permeability of many sandstone formations. Although it is relatively high when compared with other plugging materials, it is anticipated that the permeability GAC can be further reduced by increasing the carbonation level, that is, the ratio of the amount of carbonated olivine in the post-reaction products over the total amount of fresh olivine in the pre-reaction product. For example, previous research has shown that the longer reaction time can enhance the carbonation level (Case et al., 2011; Giammar et al., 2005; O'Connor et al., 2005a, 2005b; Oelkers, 2001). Since the time frame of P&A is geological time, this extremely long service life may be beneficial for the ongoing increase of carbonation level and could further reduce the permeability. Furthermore, the carbonation level can even more substantially increased if the current MC-surrounding-MS binding pattern can be improved. As shown in Figure 11, since the reaction will first start from the periphery of the olivine particle, the reaction will stop once the newly generated MC completely covers the unreacted MS, which leaves a low carbonation level around the center area in the MS-surrounding-MS structure. This binding pattern has also been observed in some previous studies (Ashraf, 2016; Guan et al., 2018). So, it is likely that the ratio of surface area to volume, which is directly related to the particle size distribution, is important and can be optimized to obtain both short term permeability and proportion of unreacted olivine that will remain for self-sealing after initial carbonation takes place.

While the matrix permeability of the GAC is related to the carbonation level, the self-sealing ability of GAC is proposed to be largely determined by the carbonation reaction rate.

Because self-sealing is almost certainly rate-dependent, it is likely that it fluid transport could, at some point, become so rapid that reactants, most notably Mg^{2+} ions, will be swept away by advection before they are able to participate in a precipitation reaction that will seal a fracture. So, the efficacy of self-sealing must rely on the comparison between the reaction rate and the fluid flow rate. When the reaction rate is significantly larger than the leak flow rate, the fluid can be gradually trapped by the newly generated binder until the flow path is completely sealed. Thus, the maximum effective flow rate of self-sealing is associated with temperature, pressure, fracture width, and presumably a variety of other parameters. The work presented in this paper conceptually demonstrated the self-sealing ability under the combinations of certain representative challenging factors, but future studies are needed in order to investigate how the interplay between the reaction rate and transport rate determines the ability of the material to self-seal.

2.6 Conclusions

Experiments provide proof-of-concept for genesis and self-sealing of Geologically Activated Cementing materials (GAC). These experiments are performed at conditions that are both ideal for olivine carbonation and similar to HPHT conditions in many deep wells including deep-water reservoirs. The products of GAC genesis experiments were analyzed and identified under XRD, SEM/EDS, and solubility tests. Permeability testing of damaged specimens of both GAC and class H cement provide measurement of the evolution of transport properties when subjected to flow of acidic fluid under HPHT conditions.

The results of these experiments demonstrate that combining a CO_2 source and olivine (Mg_2SiO_4) mimics the natural process of olivine weathering via dissolution and subsequent carbonate precipitation. However, because of the HPHT conditions, the reactions occur on a time scale of hours to days, thereby making the process relevant to engineering applications. In this way, an approach is developed that transforms sand into a sandstone-like material within a day. By using a binder that does not rely on Portland cement, the reactions proceed with minimally processed materials and lead to product(s) that are more chemically similar to natural materials such as limestone and carbonate-bound sandstone.

Besides the improvement in potential for long-term chemical stability that is expected from a material that emulates natural carbonates that can be stable for millions of years, GAC is shown in these experiments to have a self-sealing capacity in the presence of acidic fluid under HPHT conditions. These conditions are ideal for self-sealing of GAC, but are adverse conditions for class-H cement. The data show that damaged class-H cement experiences continued increase in permeability during the hours following damage and commencing of flow of acidic fluid. In contrast, GAC experiences significant reduction in permeability over a period of hours. This result indicates that the GAC can effectively seal the breakage flow paths by the products from mineral carbonation reaction. Our experimental results therefore clearly show the potential of GAC to perform under the low pH and HPHT conditions which usually threaten most of the current plugging materials. We therefore propose GAC as a demonstration of a new direction in wellbore plugging materials, emulating natural rocks for which long term stability is well-established and turning the low pH and HPHT conditions from a threat to an advantage by seeking in nature to find desirable reactions for which the kinetics are optimized under wellbore conditions. This concept is proposed to provide resilience to failure and therefore the potential to be an important advanced material for the next generation of resilient wellbore cementing and plugging systems.

3.0 Semi-Analytical Solution for Thermo-Poro-Elastic Stresses in a Wellbore Cement Plug and Implications for Cement Properties that Minimize Risk of Failure

3.1 Chapter Summary

Cementing materials used for plugging wellbores are subjected to evolving temperature, stress, and pore pressure conditions during their service lives. The induced pore pressure changes can be problematic, especially in high temperature and high pressure (HTHP) environments and especially in low permeability materials. However, a design goal of most cement plugs is to achieve very low permeability, with the idea that lower permeability leads to better isolation. Here, with aid of a new semi-analytical solution for thermo-poro-elastic (TPE) stresses in a cylindrical cement plug that includes consideration of full coupling between hydraulic and thermal transport models (so-called "porothermoelastic-osmosis-filtration", or "PTEOF" model), this work shows that lower permeability is not always better. Specifically, the solution shows that materials that are unable to drain excess pore pressure quickly enough compared to the rate at which these pressures build due to thermal changes are more prone to generate regions of internal tensile effective stress and hence are more likely to be damaged. The specific parameter groups associated with this "permeability penalty" are obtained through a combination of dimensional and pairwise bivariate analysis. These approaches give rise to two dimensionless groups of parameters that are mainly associated with propensity to generate TPE tensile effective stresses. The parametric space defined

by these two groups is shown to have three distinct regions based on the probability of generating tensile effective stresses in a plug with a given set of material properties. By shifting the focus of material design from achieving the lower possible permeability to instead achieving the lowest permeability that will not incur increase likelihood of failure due to pore pressure buildup, this work provides a new design concept for wellbore cement. Furthermore, this work highlights for the first time the important role of specific heat of the cement in preventing pore pressure buildup, thereby showing a new way forward for cement design to increase this quantity.

3.2 Introduction

Properly designed and executed wellbore cementing and plugging operations are important for various geotechnical applications. These include radioactive waste disposal, deep-well plug and abandonment (P&A), drilling and completion in unconventional reservoirs, Enhanced Geothermal System (EGS), and carbon capture utilization and storage (CCUS) (Gruber et al., 2021; Hargis et al., 2021; Koťátková et al., 2017; Olson et al., 2015; Vrålstad et al., 2019). Despite the advancements in cementing materials over the last several decades, the quality of cementing is still often associated with some deficiencies, mainly due to the harsh environments where cement is placed (Ahmed et al., 2020; Allahvirdizadeh, 2020a; Kiran et al., 2017). Taking wellbore P&A as an example, over the years and across companies, the upper range of the reservoirs' pressure and temperature have been pushing up to 275 MPa and 315 Celsius (DeBruijn et al., 2008; Khalifeh et al., 2020). However, the cement is originally designed for low-temperature and low-pressure conditions. Under harsh wellbore conditions, its stability over an extended period of time is unknown. To mitigate this problem, extensive research has been focusing on reinforcing the cement by inclusion of various additives aiming to provide better mechanical and hydraulic properties, with the goal of maintaining the system integrity under the extreme conditions (Cai et al., 2022; Ge et al., 2018; Katende et al., 2020a; Krakowiak et al., 2018; Massion et al., 2021; Massion et al., 2022; Qin et al., 2021; Samarakoon et al., 2022).

While much effort has been focused on development of materials and additives, the identification of what comprises “better” mechanical and hydraulic properties of cement are still unclear. This is especially true for high temperature and high pressure (HTHP) environments.

Wellbore cement can be classified as cementitious saturated porous material with permeability ranges from milli- to nano-Darcies (Banthia et al., 1989; Goto et al., 1981; Meng et al., 2021; Picandet et al., 2011). Such a material can be heavily influenced by thermo-hydraulic-mechanical (THM) coupling in the pore space, especially when it is experiencing large temperature and pressure variations. Within the permeability range mentioned above, a very large pore pressure could be induced by the THM coupling, which will also lead to changing of the effective stress and increase the possibility failures (Ghabezloo et al., 2010). While THM coupling phenomena in porous media has been studied extensively, the wellbore-related applications have been mainly focusing on wellbore stability during drilling and fluid injection into borehole (Gao et al., 2017; Song et al., 2019; Tao et al., 2010; Zhou et al., 2009). The THM coupling effect in the cementing designs and performance has rarely been considered and fully investigated under the HTHP conditions. This knowledge gap means that conditions that will generate stresses that are able to damage the material are not well understood, and therefore it has potentially serious consequences.

To include these mutual interactions between thermal, hydraulic, and mechanical systems in the non-isothermal conditions, Biot (Biot, 1977) extended the traditional theory of poromechanics (Biot, 1941) to include the uncoupled thermal effects by incorporating the thermomolecular diffusion and dynamic forces using a variational Lagrangian thermodynamics approach. Later on, the thermal diffusion process was coupled in solid and fluid deformation by Derski (1979), as well as others (Bear et al., 1981; Kurashige, 1989; Smith et al., 1993). The abovementioned porothermoelastic formulations include an assumption to neglect the non-linear term associated with connective heat transfer, which is thought to be most appropriate for low permeability materials (Chen et al., 2005; Delaney, 1982; Gomar et al., 2014; Wang et al., 2003). Within the framework of linear porothermoelasticity, past studies have been performed for coupled THM behavior of isotropic porous media, but most of the works are assuming the fluid flux and heat flux are dominated by the pore pressure gradient and thermal gradient, respectively (Ghassemi et al., 2002; Ghassemi et al., 2009; Valov et al., 2022). That is to say, the thermo-osmosis denoted by k_{pt} (fluid flux generated by thermal gradient) and mechano-caloric effects denoted by k_{tp} (heat flux generated by pore pressure gradient) are neglected in the transport equations

$$q = -{}^{k}\!/_{u}\nabla p + k_{pt}\nabla T \,, \tag{3-1}$$

$$h = k_{tp}\nabla p - k_{t}\nabla T \,. \tag{3-2}$$

Here $\bar{q}$ is the fluid flux, $\bar{h}$ is the heat flux, p is the pore pressure, and T is the temperature field. Note that the mechano-caloric coefficient is also known thermal filtration coefficient (Cheng, 2016).

Although thermo-osmosis and mechano-caloric effects are often neglected (if for no other reason, this assumption greatly simplifies solution methods), for porous material with low permeability, these two effects can play important roles (Gonçalvès et al., 2010; Roshan et al., 2015; Trémosa et al., 2010). For example, Carnahan (1983) has shown that the thermo-osmotic flow through kaolinite can be two orders of magnitude higher than Darcy's flow (that is, the fluid flux driven by the pressure gradient term in Eq. (1)) near a nuclear waste repository. Thus, when designing the cementing under the HTHP conditions, both the thermo-osmosis and mechano-caloric effects should be taken into consideration and should not be dismissed at the outset of the solution. To the best of our knowledge, under the HTHP conditions, their influences on the cement integrity are still unclear.

By introducing a fully-coupled porothermoelastic model, which incorporates both of the thermo-osmosis and the mechano-caloric (thermal filtration) effects, dubbed here as “porothermoelastic-osmosis-filtration” (PTEOF), the present work uses a cylindrical geometry and boundary conditions inspired by cement plugs for P&A as an example to highlight the cementing challenges that are associated with HTHP conditions. The motivation of creating the PTEOF model is to have a comprehensive understanding of the cement behavior under HTHP conditions and to build up a general framework and solutions for future cementing studies. Specifically, we derive a semi-analytical solution (analytical up to a numerical inversion of a Laplace transport) that draws inspiration from the method of Sarout et al. (2011) and therefore leverages the mathematical similarity between PTEOF and linear chemo-poroelasticity. After presenting the governing equations, solution method, and examples of the behaviors predicted by the model, the key parameters associated with preventing tensile effective stresses from developing in a cement plug are identified. These are identified through a combination of dimensional analysis and pairwise bivariate analysis, leading to dimensionless groups that define a parametric space with regions that are “safe” and regions that are associated with material parameter combinations more likely to sustain damage. The work concludes with a discussion of implications for design of cement materials that do not just pursue the lowest possible permeability, but rather pursue a combination of material properties that will provide the necessary isolation without incurring elevated risk of damage from PTEOF phenomena under HTHP conditions.

3.3 Governing Equations

The formulation begins with classical tensorial strain-stress constitutive relation that expatiates upon the coupled thermo-hydro-mechanical behaviors of fluid saturated porous medium under the plain-strain conditions could be rewritten as (Cheng, 2016)

$$\bar{\sigma} = 2G\bar{\varepsilon} + \frac{2\nu G}{1-2\nu}\varepsilon\bar{I} - \alpha p\bar{I} - \alpha_d T\bar{I} \,, \tag{3-3}$$

where $\bar{\sigma}$ and $\bar{\varepsilon}$ is stress tensor components matrix and strain tensor components matrix, respectively; ε is the volumetric strain (the trace of the strain tensor); $\bar{I}$ is the second rank identity tensor; p is pore pressure change from virgin pore pressure and T is temperature change from the reference temperature $\mathcal{T}_0$; G is shear modulus and ν is Poisson's ratio; α is the Biot effective stress coefficient and α_d is the thermoelastic effective stress coefficient.

Note that, following the sign convention in Detournay et al. (1988), positive stress is considered to be tensile within the present work.

Furthermore, based on the fundamental work of Cheng (2016) and Wang (2017), within the framework of linear thermoporoelasticity, the coupled volumetric response relations are

$$\begin{pmatrix} \mathcal{E} \\ \zeta \\ \mathcal{S} \end{pmatrix} = \mathcal{N} \begin{pmatrix} \sigma \\ p \\ T \end{pmatrix}, \quad \text{where } \mathcal{N} = \begin{pmatrix} -\frac{1}{K_d} & \frac{\alpha}{K_d} & \beta_d \\ -\frac{\alpha}{K_d} & \frac{\alpha}{BK_d} & -\beta_v \\ \beta_d & -\beta_v & m_d \end{pmatrix}, \tag{3-4}$$

Note that one of these three equations can be obtained from contraction on Eq. (3-3). In Eq. (3-4), $\mathcal{E}$ and σ are volumetric strain and stress, respectively, given as the traces of their respective tensors; ζ is the variation of fluid content per unit volume; $\mathcal{S}$ is entropy density.

The material constants include the drained bulk modulus tensor K_d, Biot effective stress coefficient α, Skempton pore pressure coefficient B, coefficient of volumetric thermal expansion of porous media frame β_d, coefficient of volumetric thermal expansion of variations in fluid content in the solid-fluid system β_v (Cheng, 2016), and m_d represents the specific heat of the porous medium at the reference temperature.

Before moving on to the solution method, it is intuitive to reflect that from Eq. (3-4), deformation of the solid frame is caused by changes in stress, pore pressure, and/or temperature. The fluid phase in the porous medium is not only deforming with the solid frame, but at the same time, driven by pore pressure gradient and thermal forces, causing the pore fluid to be entering or leaving the solid frame of unit volume.

Similarly, the stress and temperature change will cause the change of the entropy of the porous system based on the generalized-energy relation. The entropy density is therefore a function of volumetric strain of the solid frame, fluid content, and the change of temperature.

Thus, the constitutive equations relate and couple volumetric strain, fluid content, and energy variables $\{\mathcal{E},\zeta,\mathcal{S}\}$ with total stress, pore stress, and temperature variables $\{\sigma, p, T\}$ with the material constants $\{\alpha, B, K_d, \beta_d, \beta_v, m_d\}$. The notation that used within this work is summarized in Table 5.

Table 5 Notation

Symbol	Definition	Unit
α	Biot effective stress coefficient	---
α_d	Drained thermoelastic effective stress coefficient	$N\cdot m^{-2}\cdot K^{-1}$
B	Skempton pore pressure coefficient	---
β_f	Coefficient of volumetric thermal expansion of fluid	K^{-1}
β_v	Coefficient of volumetric thermal expansion for variation in fluid content	K^{-1}
β_d	Drained coefficient of volumetric thermal expansion of porous medium frame	K^{-1}
m_d	Specific heat of the porous medium at reference temperature	$J\cdot m^{-3}\cdot K^{-1}$
$\overline{q}$	Fluid flux	$m\cdot s^{-1}$
$\overline{h}$	Heat flux	$J\cdot m^{-2}\cdot s^{-1}$
k	Permeability	m^2
k_t	Thermal conductivity	$W\cdot K^{-1}\cdot m^{-1}$
k_{tp}	Mechano-caloric coefficient (Thermal filtration)	$m^2\cdot s^{-1}$
k_{pt}	Thermo-osmosis coefficient	$m^2\cdot s^{-1}\cdot K^{-1}$
ν	Poisson’s ratio	---
K_d	Bulk modulus	$N\cdot m^{-2}$
G	Shear modulus	$N\cdot m^{-2}$
c_t	Thermal Diffusivity	m^2/s
c_f	Fluid Diffusivity	m^2/s

Next, based on quasi-static equilibrium, the divergence of the stress tensor is taken to be zero, $\bar{\sigma}$, that is

$$\nabla \cdot \bar{\sigma} = 0 , \tag{3-5}$$

where volumetric stress σ is the trace of the stress tensor. Furthermore, if the displacement is $\bar{\mathcal{U}}$, then the classical small strain assumption is adopted whereby the strain-displacement relations are

$$\bar{\varepsilon} = \frac{1}{2}(\nabla \bar{\mathcal{U}} + \nabla^{T} \bar{\mathcal{U}}) . \tag{3-6}$$

Next, we consider the fluid in the pore spaces to be incompressible so that the divergence of the fluid flux (q) is directly balanced by rate of change of the variation of fluid content (ζ), hence (Cheng, 2016)

$$\frac{\partial \zeta}{\partial t} + \nabla \cdot \bar{q} = 0 . \tag{3-7}$$

A similar conservation law assumes the heat flux only through conduction and relates the divergence of the heat flux (h) to the rate of change of the entropy density ($\mathcal{S}$) according to (Cheng, 2016)

$$\frac{\partial \mathcal{S}}{\partial t} + \nabla \cdot \bar{h} = 0 . \tag{3-8}$$

By substituting both transport laws (Eq. (3-1) and Eq. (3-2)) into the conservation laws, the fully coupled diffusion equations are obtained as

$$\frac{\partial \zeta}{\partial t} = k \nabla^{2} p - k_{pt} \nabla^{2} T , \tag{3-9}$$

and

$$\frac{\partial \mathcal{S}}{\partial t} = -k_{tp} \nabla^{2} p + k_{t} \nabla^{2} T . \tag{3-10}$$

In these equations, the balancing of the rate of change of fluid content and entropy density with the Laplacian of the fluid pressure and temperature, respectively, comprise the classical uncoupled diffusion equations. However, these equations also have off-diagonal terms that relate rate of change of fluid content to the Laplacian of the temperature field, as well as the rate of change of entropy density to the Laplacian of the fluid pressure. These impacts are known as the thermal osmosis effect and thermal filtration effect, respectively. The model fully coupling all of these terms will henceforth be referred as the porothermoelastic-osmosis-filtration (PTEOF) model. While it may indeed be valid at times to neglect thermal osmosis and/or thermal filtration, here we retain the full coupling in order to elucidate conditions in which they may have an important impact.

With the addition of boundary and initial conditions (to be discussed later), Eqs. (3-1 to 3-10) comprise a complete model, sufficient to solve for all unknown quantities.

3.4 PTEOF Solution for Constrained Cylinder

3.4.1 Problem Description and Boundary Conditions

Consider a thermoporoelastic cylinder of radius R and length 2L (Figure 15 a). Both of its ends are jacketed which is fixed and impermeable for fluid and thermal isolation from heat. The radial boundary conditions are unjacketed and can have fluid and heat exchange at the boundary. This constrained cylinder geometry is inspired by the geometry and boundary conditions of the primary plug in P&A (Figure 15 a) where the length of the primary plug is usually 50 to 100 times larger than its diameter that often ranges from 5 to 20 inches and its loadings mainly come from the high temperature, and pore pressure from the formation, and the far-field in-situ stress. Thus, it is appropriate to apply the generalized plane-strain assumption where the pore pressure and thermal diffusion only appear in the isotropic plane that is perpendicular to the length axis of the plug which is fully saturated.

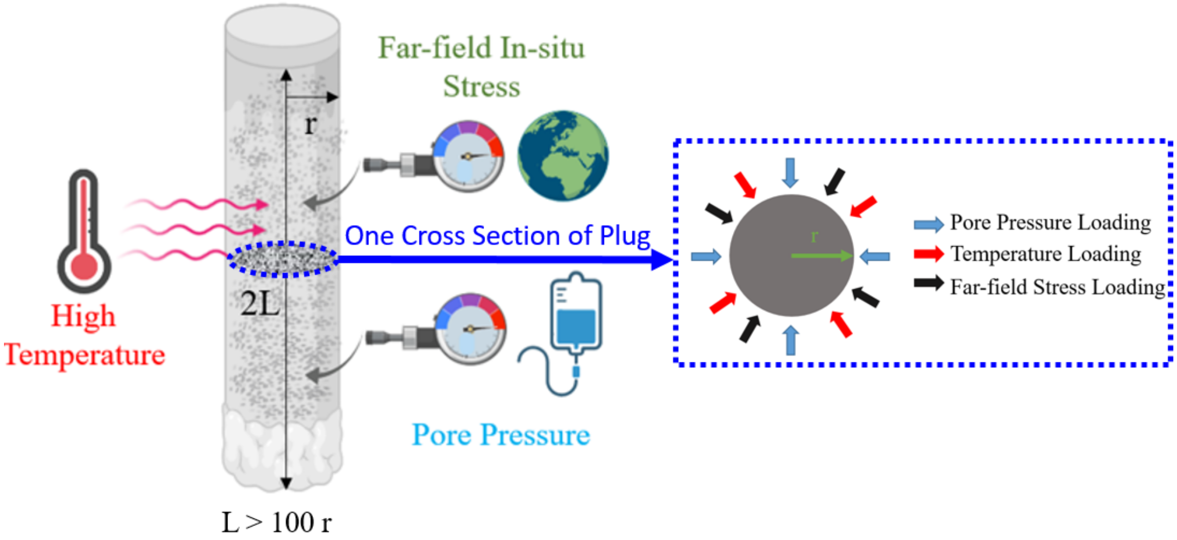

Figure 15 (a) Sketch showing a primary plug in P&A and its boundary conditions; (b) A zoom in sketch showing a cross-section of the plug in plane-strain conditions and its boundary conditions.

In line with the loading decomposition scheme proposed by Detournay et al. (1988) in the context of poroelasticity, the PTEOF model can be decomposed into three sub-loading cases to simplify the analysis. These are: 1) pore pressure loading, 2) temperature loading, and 3) isotropic far-field stress loading. Thus, the boundary conditions at the outside surface of the primary cement plug for each of the loading modes can be written as follows (the subscript f denotes formation, subscript c denotes cement)

- Mode 1: $\sigma_{rr} = 0$, $p = \Delta p \bullet H(t)$, and $T = 0$, at $r = R$;
- Mode 2: $\sigma_{rr} = 0$, $p = 0$, and $T = \Delta T \bullet H(t)$, at $r = R$;

- Mode 3: $\sigma_{rr} = \Delta\sigma \bullet H(t)$, $p = 0$, and $T = 0$, at $r = R$;

where σ_{rr} is the normal stress in the radial direction, and $H(t)$ is the Heaviside step function

$$H(t) = 1, \text{ when } t > 0. \tag{3-11}$$

Since the PTEOF model is linear, the principle of superposition will be used as final step to obtain the final solution by combining the individual loading modes. Note that, in general, there is a fourth mode of loading corresponding to deviatoric far field stress, which is neglected here but can be useful as a future investigation.

3.4.2 Solution to The Fully Coupled Diffusion Equations

The solution method starts with obtaining a general solution of the fully coupled diffusion equations (Eq. (3-9) and Eq. (3-10)). Note that the plane-strain assumption will lead to fluid and thermal transport directed only along the radial direction in the cylindrical coordinates system. Then, the first step is to eliminate ζ and $\mathcal{S}$ in the diffusion equations by substituting the constitutive equations (Eq. (3-4)). This results in a new form of coupled diffusion equations

$$\frac{\partial \mathcal{E}}{\partial t} = \frac{k}{\alpha}\nabla^2 p - \frac{1}{M\alpha}\frac{\partial p}{\partial t} + \frac{k_{pt}}{\alpha}\nabla^2 T + \frac{\beta_e}{\alpha}\frac{\partial T}{\partial t}, \tag{3-12}$$

$$\frac{\partial \mathcal{E}}{\partial t} = \frac{k_t}{\alpha_d}\nabla^2 T - \frac{m}{\alpha_d}\frac{\partial T}{\partial t} + \frac{k_{tp}}{\alpha_d}\nabla^2 p + \frac{\beta_e}{\alpha_d}\frac{\partial p}{\partial t}, \tag{3-13}$$

where $\beta_e = \alpha\beta_d + \beta_v$, $\alpha_d = \beta_d K_d$ and $M = BK_d / (\alpha - \alpha^2 B)$.

Next, by combining Eq. (3-3), Eq. (3-4) and Eq. (3-5), and taking the body force to zero, an extended form of the classical Navier equation is obtained as

$$G\nabla^2 \bar{\mathcal{U}} + \frac{G}{1-2\nu}\nabla\mathcal{E} = \alpha\nabla p + \alpha_d \nabla T\ . \tag{3-14}$$

Drawing on the approach of Sarout et al. (2011), we can then use the irrotational field assumptions to simplify the process of solving the Navier equations. When displacement field is irrotational, i.e. $\bar{\mathcal{U}}$ is the gradient of a scaler, one can integrate Eq. (3-14) to obtain

$$\mathcal{E} = g_1 p + g_2 T + f(t), g_1 = \frac{\eta}{G}, g_2 = \frac{\eta_d}{G} \tag{3-15}$$

where $\eta = \frac{\alpha(1-2\nu)}{2-2\nu}$ and $\eta_d = \frac{\alpha_d(1-2\nu)}{2-2\nu}$.

The function $f(t)$ results from the integration and it therefore does not depend on the spatial coordinates. In fact, for many infinite or semi-infinite domain problems, conditions exist to require quantities decay to zero in the far field, thus forcing to *f(t)* to be zero (Detournay et al., 1993). But, for the present finite domain problem, $f(t)$ will not be zero but instead is a part of the solution. Next, by substituting Eq. (3-15) into Eq. (3-12) and Eq. (3-13), the volumetric strain $\mathcal{E}$ can be eliminated thus leaving the coupled diffusion equations

$$\begin{bmatrix} \mathcal{K}_{11} & \mathcal{K}_{12} \\ \mathcal{K}_{21} & \mathcal{K}_{22} \end{bmatrix} \begin{bmatrix} \nabla^2 p \\ \nabla^2 T \end{bmatrix} = \begin{bmatrix} \frac{\partial p}{\partial t} \\ \frac{\partial T}{\partial t} \end{bmatrix} + \begin{bmatrix} \Theta_1 \\ \Theta_2 \end{bmatrix} f^{'}(t), \tag{3-16}$$

where:

$$\mathcal{K}_{11} = [k_{tp} M(ag_2 - \beta_e) + Mk(m + K_d \beta_d g_2)] / \mathit{\Psi}, \tag{3-17}$$

$$\mathcal{K}_{12} = [-Mk_t(ag_2 - \beta_e) - Mk_{pt}(m - K_d \beta_d g_2)] / \mathit{\Psi}, \tag{3-18}$$

$$\mathcal{K}_{21} = [k_{tp}(aMg_1 - 1) - kM(\beta_e - K_d \beta_d g_1)] / \mathit{\Psi}, \tag{3-19}$$

$$\mathcal{K}_{22} = [k_t(1 + aMg_1) - k_{pt} M(\beta_e - K_d \beta_d g_1)] / \mathit{\Psi}, \tag{3-20}$$

$$\Theta_1 = M(am_d + K_d \beta_d \beta_e) / \mathit{\Psi}, \tag{3-21}$$

$$\Theta_2 = (aM\beta_e + K_d \beta_d) / \mathit{\Psi}, \tag{3-22}$$

$$\mathit{\Psi} = (m_d - M\beta_e^{\,2} + K_d\beta_d g_2 + aM\beta_e g_2 + aMg_1 m_d + K_d M\beta_d\beta_e g_1)\,. \tag{3-23}$$

The diffusion equations in Eq. (3-16) are coupled in terms of T and p, which can be transformed into uncoupled equations in terms of Φ_1 and Φ_2 by using the eigen decomposition approach developed by Sarout et al. (2011). This methodology starts by obtaining two eigenvalues λ_1 and λ_2 of the $\bar{\mathcal{X}}$ matrix. Then, the eigen decomposition theorem (Weisstein, 2002) allows us to define a transition matrix $\bar{\Upsilon}$, which is composed of eigenvalues and eigenvectors of $\bar{\mathcal{X}}$. The temperature and pore pressure therefore be changed into new variables by

$$\begin{bmatrix} p \\ T \end{bmatrix} = \begin{bmatrix} 1 & \Upsilon_{12} \\ \Upsilon_{21} & 1 \end{bmatrix} \begin{bmatrix} \Phi_1 \\ \Phi_2 \end{bmatrix}, \tag{3-24}$$

where

$$\Upsilon = \begin{bmatrix} 1 & \dfrac{\lambda_2 - \mathcal{X}_{22}}{\mathcal{X}_{21}} \\ \dfrac{\lambda_1 - \mathcal{X}_{11}}{\mathcal{X}_{12}} & 1 \end{bmatrix},$$

$$\lambda_{1,2} = \frac{1}{2}[\mathcal{X}_{11} + \mathcal{X}_{22} \pm \sqrt{(\mathcal{X}_{11} - \mathcal{X}_{22})^2 + 4\mathcal{X}_{12}\mathcal{X}_{21}}\,]\,.$$

Substituting this change of variables into Eq. (3-16) leads to an uncoupled system of diffusion equations and this process can be developed based on the Eigen decomposition theorem

$$\frac{\partial \Phi_i}{\partial t} = \lambda_i \nabla^2 \Phi_i - \mathcal{D}_i f^{'}(t)\,, \tag{3-25}$$

where $\mathcal{D}_i = \Upsilon^{-1}\mathcal{X}^{-1}\Theta_i, i = 1, 2$. Then, by applying the Laplace transform to the eigenfunction

$$\mathcal{L}[\Phi(\xi_i, t)] = \tilde{\Phi}(\xi_i, s), \tag{3-26}$$

where $\xi_i = \rho\sqrt{\frac{s}{\lambda_i}}$, one obtains an uncoupled system of ordinary differential equations (ODEs) in terms of the variables ξ_i, where ξ_i is function of the coordinators in cylindrical system ρ, and the Laplace parameter s and the $\mathcal{X}$'s eigenvalue λ_i. These ODEs are

$$s\tilde{\Phi}_i = \lambda_i \nabla^2 \tilde{\Phi}_i - \mathcal{D}_i sF(s). \tag{3-27}$$

$\tilde{\Phi}_i$ are zeroth-order modified Bessel equations, which have the general solution

$$\tilde{\Phi}_i(\xi_i, s) = c_i(s) I_0(\xi_i) + d_i(s) K_0(\xi_i) - \lambda_i \mathcal{D}_i F(s), i = 1, 2, \tag{3-28}$$

Here c_i , d_i and $F(s)$ are unknowns that will be determined based on boundary conditions, $I_0(\xi_i)$ and $K_0(\xi_i)$ are the zeroth-order modified Bessel functions of the first and second kind, respectively.

The next step is to invoke the symmetry conditions of the problem under consideration, which ensure that d_i =0. Thus the pore pressure and temperature profile in the Laplace domain are

$$\tilde{p} = \mathcal{X}_{11}\tilde{\Phi}_1(\xi_1, s) + \mathcal{X}_{12}\tilde{\Phi}_2(\xi_2, s)\,, \tag{3-29}$$

$$\tilde{T} = \mathcal{X}_{21}\tilde{\Phi}_1(\xi_1, s) + \mathcal{X}_{22}\tilde{\Phi}_2(\xi_2, s)\,. \tag{3-30}$$

The radial stress under the plane-strain conditions (Eq. 3-3) consists volumetric strain (ε) and radial strain (ε_{rr}). Both of them can be obtained through the radial displacement $\mathcal{U}_r$, which is integrated by the Eq. (3-15). Thus, the radial stress can be expressed in Laplace domain as

$$\tilde{\sigma}_{rr} = 2Gv/(1-2v)\tilde{\mathcal{E}} + 2G\tilde{\mathcal{E}}_{rr} - \alpha\tilde{p} - \alpha_d\tilde{T}\,, \tag{3-31}$$

Where the trace of strain tensor in Laplace domain is

$$\tilde{\mathcal{E}} = \frac{1}{r}\frac{\partial r\tilde{\mathcal{U}}_r}{\partial r} = \frac{\partial\tilde{\mathcal{U}}_r}{\partial r} + \frac{\tilde{\mathcal{U}}_r}{r}\,, \tag{3-32}$$

and radial strain is

$$\tilde{\mathcal{E}}_{rr} = \frac{\partial\tilde{\mathcal{U}}_r}{\partial r}\,. \tag{3-33}$$

Up to now, there are three unknowns $c_1(s)$, $c_2(s)$, and $F(s)$ in the system. The first two unknowns $c_1(s)$ and $c_2(s)$ come from the coefficient of the zeroth-order modified Bessel functions of the first kind. The third unknown, $F(s)$, is coming from the spatially uniform function from Eq. (3-27). In the process of deriving the above expressions for the pore pressure, temperature, and radial stress, we can create three equations for these three unknowns

$$\begin{pmatrix} \Upsilon(1,1)\,I_0(\xi_1) & \Upsilon(1,2)I_0(\xi_2) & \Upsilon(1,2)\lambda_2\mathcal{H}_2 + \Upsilon(1,1)\,\lambda_1\mathcal{H} \\ \Upsilon(2,1)\,I_0(\xi_1) & \Upsilon(2,2)I_0(\xi_2) & \Upsilon(2,2)\lambda_2\mathcal{H}_2 + \Upsilon(2,1)\,\lambda_1\mathcal{H}_1 \\ \mathcal{M}_1 & \mathcal{M}_2 & \mathcal{M}_3 \end{pmatrix}\begin{pmatrix} c_1 \\ c_2 \\ -F \end{pmatrix} = \begin{pmatrix} p/s \\ T/s \\ \sigma_{rr}/s \end{pmatrix} = \begin{pmatrix} \tilde{p} \\ \tilde{T} \\ \tilde{\sigma}_{rr} \end{pmatrix} \quad （3\text{-}34）$$

where

$$\mathcal{M}_1 = \frac{1}{r}\frac{I_1(\xi_1)}{\sqrt{\lambda_1/s}}\left[\mathcal{A}_2\Upsilon(1,1)+\mathcal{A}_1\Upsilon(2,1)\right]+I_0(\xi_1)\left[\mathcal{A}_3\Upsilon(2,1)+\mathcal{A}_4\Upsilon(1,1)\right],$$

$$\mathcal{M}_2 = \frac{1}{r}\frac{I_1(\xi_2)}{\sqrt{\lambda_2/s}}\left[\mathcal{A}_1\Upsilon(1,2)+\mathcal{A}_2\Upsilon(1,2)\right]+I_0(\xi_2)\left[\mathcal{A}_3\Upsilon(2,2)+\mathcal{A}_4\Upsilon(1,2)\right],$$

$$\mathcal{M}_3 = -\mathcal{A}_5+\frac{1}{2}\begin{pmatrix}\mathcal{A}_1\left[\mathcal{H}_1\Upsilon(2,1)+\mathcal{H}_2\Upsilon(2,2)\right]+\mathcal{A}_2\left[\mathcal{H}_1\Upsilon(1,1)+\mathcal{H}_2\Upsilon(1,2)\right]+\\ \mathcal{A}_3\left[\mathcal{H}_1\Upsilon(2,1)+\mathcal{H}_2\Upsilon(2,2)\right]+\mathcal{A}_4\left[\mathcal{H}_1\Upsilon(1,1)+\mathcal{H}_2\Upsilon(1,2)\right]\end{pmatrix}, \mathcal{H}_i=\Upsilon^{-1}\Theta_i, i=1,2,$$

$$\mathcal{A}_1 = \frac{2Gv}{1-2v}\frac{\eta}{G}-\frac{2G-2Gv}{1-2v}\frac{\eta}{G},$$

$$\mathcal{A}_2 = \frac{2Gv}{1-2v}\frac{\eta_d}{G}-\frac{2G-2Gv}{1-2v}\frac{\eta_d}{G},$$

$$\mathcal{A}_3 = \frac{2G-2Gv}{1-2v}\frac{\eta}{G}-\alpha,$$

$$\mathcal{A}_4 = \frac{2G-2Gv}{1-2v}\frac{\eta_d}{G}-\alpha_d.$$

So, when given a value of s, the three unknowns can be readily computed, thus the solution can be numerically inverted to the time domain using Stehfest's method (Stehfest, 1970), which has been shown to be efficient in poroelastic problems, and its details are given in Appendix A.

3.5 Behavior of The Model

This section will investigate different behaviors of the model and an example case is selected in order to have a further illustration. Based on the information provided by the literatures (Addis, 1997; Santarelli et al., 1998; Snee et al., 2018; Zoback et al., 2003), this example involves all three loading modes which are determined by the boundary conditions, specifically:

- Mode 1: a difference between the formation and cement plug is $\Delta p = 2.9 \times 10^7$ Pa;
- Mode 2: a difference between the formation and cement is taken as $\Delta T = 40$ Kelvin;
- Mode 3: a change of far-field isotropic stress is taken as 1.5×10^7 Pa.

The details of the initial conditions will be introduced later in the section 3.5.3 where the effective stress is discussed. The above mentioned literatures also inspire the other parameters to be taken as

$$\begin{aligned} &\alpha = 0.95 \qquad B = 0.9 \qquad v = 0.22 \qquad G = 12E9 N \cdot m^{-2} \\ &k_{tp} = 1E-6 m^2 \cdot s^{-1} \qquad k_t = 10 W \cdot K^{-1} \cdot m^{-1} \qquad k = 1E-20 m^2 \\ &k_{pt} = 1E-20 m^2 \cdot s^{-1} \cdot K^{-1} \qquad \beta_v = 2E-4 K^{-1} \qquad m_d = 1E6 J \cdot kg^{-1} \cdot K^{-1} \end{aligned} \tag{3-35}$$

3.5.1 Pore Pressure Responses and Thermal Osmosis Effect

The change of pore pressure (p) in response to different loadings is a key component in poromechanical analysis. It is therefore of interest to firstly plot the evolution of pore pressure under three different loading modes, given the boundary conditions that are defined in the last section, while the influence of the factors of interest on the pore pressure will be analyzed and discussed later.

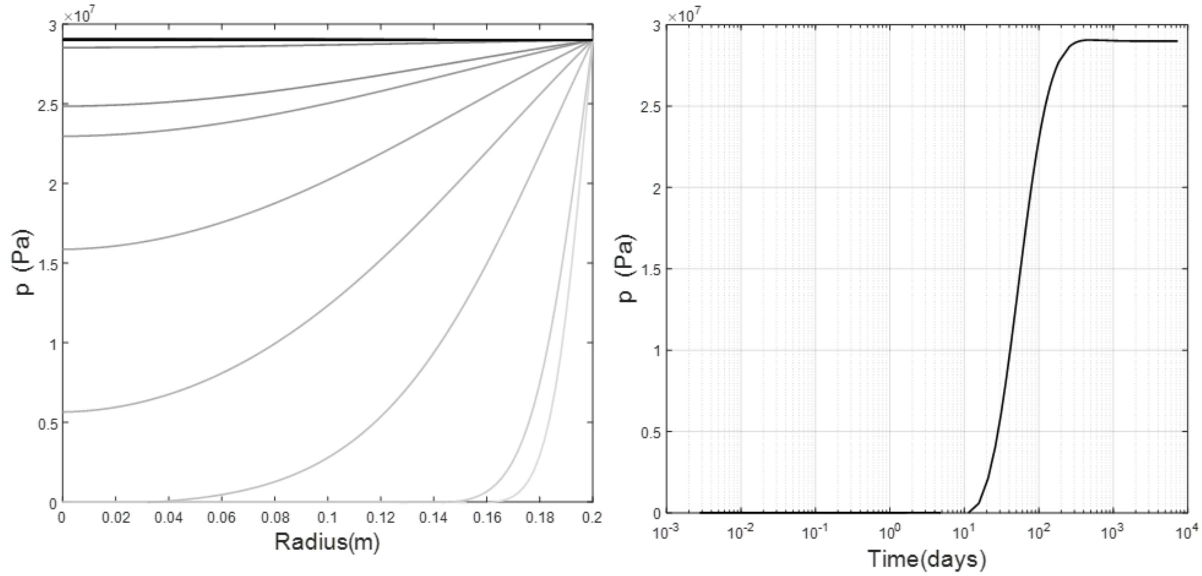

Figure 16 (a) Pore pressure change (p) due to mode 1 loading, where the curves grade from gray to black as time increases; (b) Evolution of pore pressure change (p) induced by mode 1 at center of the cylinder (r=0).

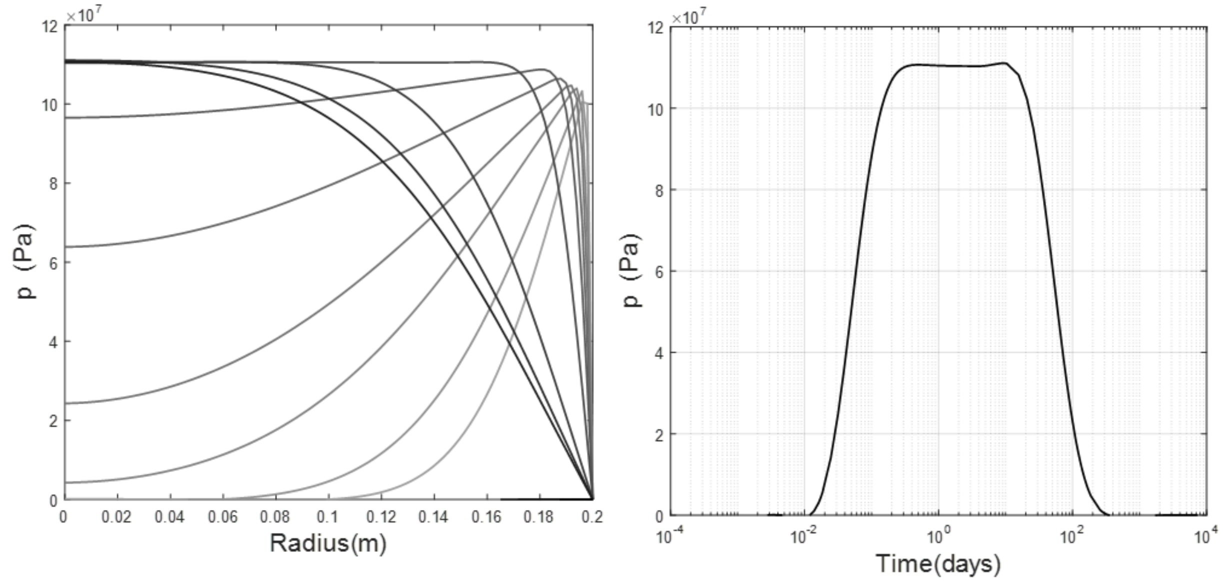

Figure 17 (a) Pore pressure change (p) due to mode 2 loading, where the curves grade from gray to black as time increases; (b) Evolution of pore pressure change (p) induced by mode 2 at center of the cylinder (r=0).

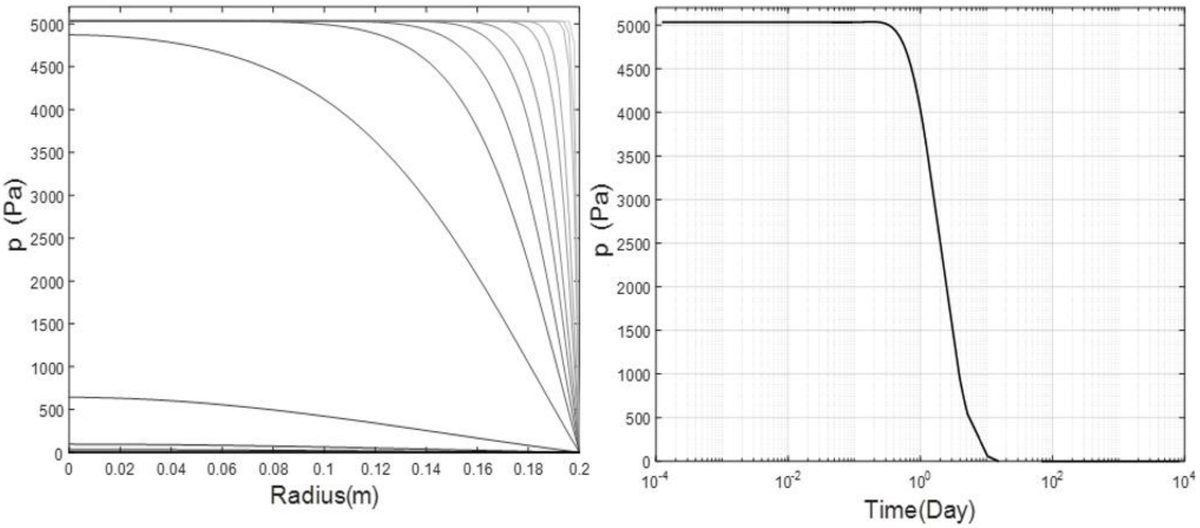

Figure 18 (a) Pore pressure change (p) due to mode 3 loading, where the curves grade from gray to black as time increases; (b) Evolution of pore pressure change (p) induced by mode 3 at center of the cylinder (r=0).

Figure 16a and Figure 17a illustrate the pore pressure change (p) profile along the radius in response to mode 1 loading (pore pressure loading) and mode 2 loading (temperature loading), respectively. Under the mode 1 loading, the pore pressure evolution follows in the manner of a classical diffusion process. The pore pressure near the surface (r=0.2m) is instantly raised to the level of the pore pressure loading, and then the pore pressure gradually diffuses towards the center (r=0).

In contrast to gradual and smooth diffusion process from external pore pressure loading, the pore pressure induced by mode 2 temperature loading firstly peaks just inside the boundary. The pressure change at the boundary in this case is held at zero due to the boundary conditions. Once the initial pressure peak develops, it initially decreases to zero at the inner core, resulting in a pressure peak. This pore pressure peak results in fluid flux both toward the boundary and toward the center. However, because fluid diffusion is slow compared to thermal diffusion, the pressure does not appreciably dissipate. Instead, as the temperature front moves to the core, the pore pressure increases along with it. Eventually the pressure becomes nearly uniform through the central region, while it continues to have a gradient toward the boundary. Hence, the pressure is being alleviated by fluid diffusion across the outer boundary. But, again because of the slow fluid diffusion due to low hydraulic conductivity (in comparison to the thermal conductivity), for some time there persists only a small layer at the boundary where the pressure is able to drain. Eventually, long after the entire specimen is entirely heated, the entire pore pressure dissipates and returns to zero everywhere.

The time evolution of the pore pressure due to modes 1 and 2 loading is illustrated by the pressure at the center, shown in Figure 16b and Figure 17b. After pressure loading, the pore pressure in the center is shown for this example to begin increasing after about 1 month, reaching its peak, steady-state value after about 1 year. Hence, any pore pressure change that takes place over a time that is considerably smaller than this characteristic time of evolution can be approximated by the instantaneous change considered in this solution. The pore pressure due to thermal loading progresses somewhat more quickly, owing to the higher thermal diffusivity. After the thermal loading is induced, the pressure at the center begins to rise very soon thereafter, within less than 1 day. The induced pressure pulse in this example persists for a few months.

In contrast to the previous two modes, the pore pressure change (p) that is induced by mode 3 (isotropic far-field stress) is shown in Figure 18a. Here the pore pressure immediately arrives at its highest value except in a small layer near the boundary where the pore pressure reduces to zero due to the boundary conditions. This initial pore pressure field gradually declines to zero everywhere due to fluid diffusion. The entire process for this example takes place over the course of about 1 month (Figure 18b). It should be noted that the magnitude of the pore pressure induced by mode 3 is much smaller compared to the pore pressure induced by mode 1 and mode 2. Even at the highest level of pore pressure, which is right after the loading is applied, the ratio of mode 3 induced pore pressure over mode 1 and mode 2 induced pore pressure is around 0.01%-0.02%. This is also in line with the findings from the classical poroelastic model (Detournay et al. (1988).

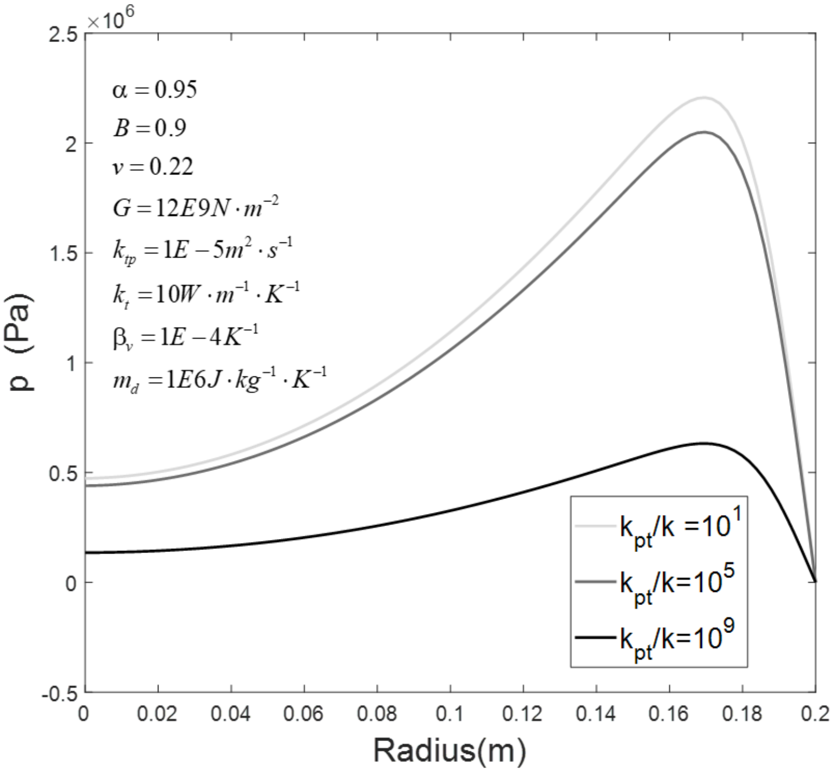

Figure 19 Various ratios of kpt/k(thermo-osmosis's influence) impacting the mode 2 induced pore pressure shown at (10-4 days).

3.5.2 Thermo-Osmosis and Thermo-Filtration Effects

So far, all results have been presented with a single combination of parameters governing thermos-osmosis and thermo-filtration. To examine these effects, we will present the internal pressure profile at *t*=10 days after thermal (mode 2) loading. Three different ratios (1, 10^5, 10^9) of

k_{pt} / k are selected to show the different developments of the temperature induced pore pressure (Figure 19), noting that $k_{pt} / k = 1$ corresponds to the case presented in Figure 17. All three cases show a peak pore pressure near the surface region; however, the magnitude of the peak induced pore pressure has considerable reduction when the thermo-osmotic coefficient is significantly larger than the hydraulic conductivity (i.e., $k_{pt} / k = 10^9$). While it is not clear if this ratio is realistic (it might be, but there has been little study), it is clear that thermos-osmosis does have potential to contribute a reduction in the induced pore pressure from temperature loading.

The role of thermo-filtration is made most apparent by observing the temperature profiles resulting from the mode 2 (temperature) loading. A base case is shown in Figure 20. As the time proceeds, temperature is increasing monotonically from surface towards the inner core of the plug, and finally arrives at equilibrium, which is the equilibrium. Three different ratios of thermal conductivity over the thermal filtration coefficients are selected to show the impact of the thermal filtration effect on the temperature profile as it is changed by the pore pressure gradient from mode 1 loading. As shown in Figure 21, among the three selected ratios, the maximum temperature difference induced by the pore pressure gradient is within 1 Kelvin. Furthermore, when the thermal conductivity is significantly larger than the thermal filtration coefficient ($k_t / k_{tp} = 10^8$), the induced temperature differences are negligible under the current model settings and inputs.

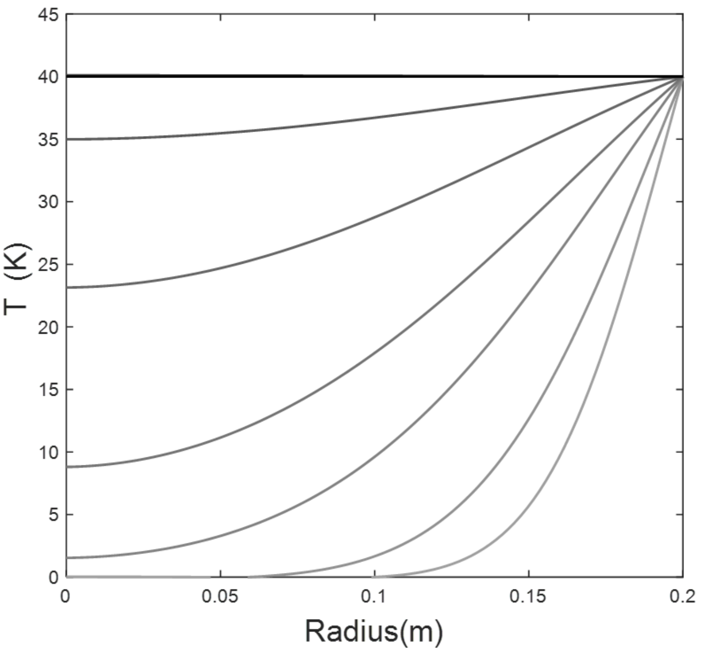

Figure 20 The development of temperature change (T) under loading mode 2, where the curves grade from gray to black as time increases.

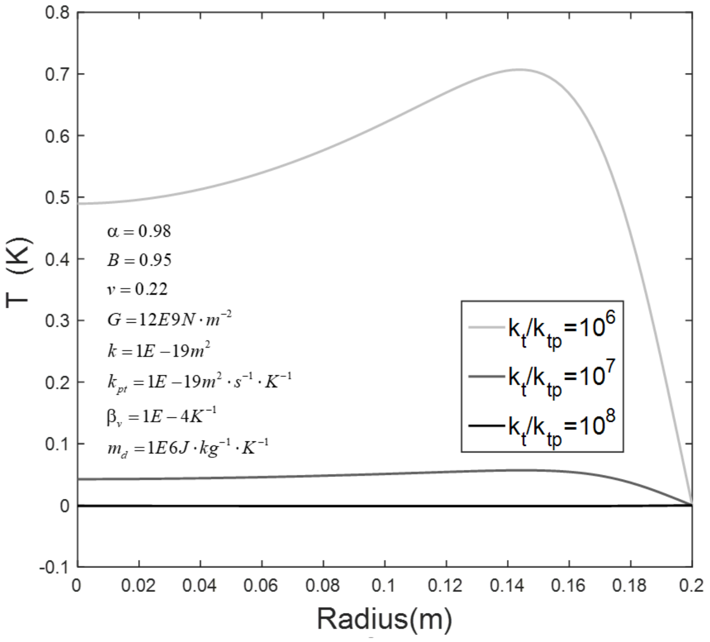

Figure 21 Various ratios of kt/ktp (thermal filtration's influence) impacting the temperature change (T) due to loading mode 1.

3.5.3 Effective Stress

There is a vast literature pointing to the impact of the so-called effective stress on behavior of porous media, where effective stress is defined as the difference between the total stress and the pore pressure (Biot, 1941; Terzaghi, 1925). Its significance lies in that it quantifies the total stress carried by the solid skeleton. Hence, when it becomes tensile, it indicates that the skeleton is subjected to tension. In materials like cement, rock, and soil, the tensile strength is low and so generation of tension indicates risk of tensile failure. Based on the information provided by the literatures (Addis, 1997; Santarelli et al., 1998), the initial conditions of this example are set up as follows: the initial pore pressure of the cement plug is set up 1.5×10^7 Pa; the initial temperature in cement is initially 313 Kelvin; the initial far-field isotropic stress is setup as 4×10^7 Pa. The boundary conditions are still remained the same as what stated at the beginning of this section. Here, the effective radial stress $\sigma_r^{'}$ is obtained as the summation of the initial effective stress ($\sigma_{initial}^{'}$) and superposition of the effective stress $\sigma_{rr}^{i'}$ from three loading modes as

$$\sigma_r^{'} = \sigma_{initial}^{'} + \sum \sigma_{rr}^{i'}, \tag{3-36}$$

where $\sigma_{initial}^{'} = \sigma_{rr\_initial} - p_{initial}$, $\sigma_{rr}^{i'} = \sigma_{rr}^{i} - p^{i}$, and $i = 1, 2, 3$.

The result is plotted in Figure 22, recalling that tension is positive. It is observed that after the cement is placed under the pore pressure, temperature, and stress loadings, the induced pore pressure will increase and will therefore reduce the radial effective stress near the boundary. The results show that it can create a region where effective stress is tensile. However, outside of this region and at early times, the rest of the material will still be subjected to compressive effective stresses. Furthermore, because the pore pressure diffusion process is very slow compared to thermal diffusion, the pore pressure continues to increase through to the center and eventually a tensile region will be created throughout the central region. Finally, at a later time when induced pore pressure is fully dissipated, the radial effective stress will return to be compressive again. This demonstration of the whole diffusion process indicates that cementing under the HTHP has potential to induce a high value of pore pressure, which will lower the effective stress and can even generate a tensile region. This coupled behavior can therefore lead to cracking of the cement, jeopardizing the integrity of the cementing system with the potential to trigger unwanted consequences.

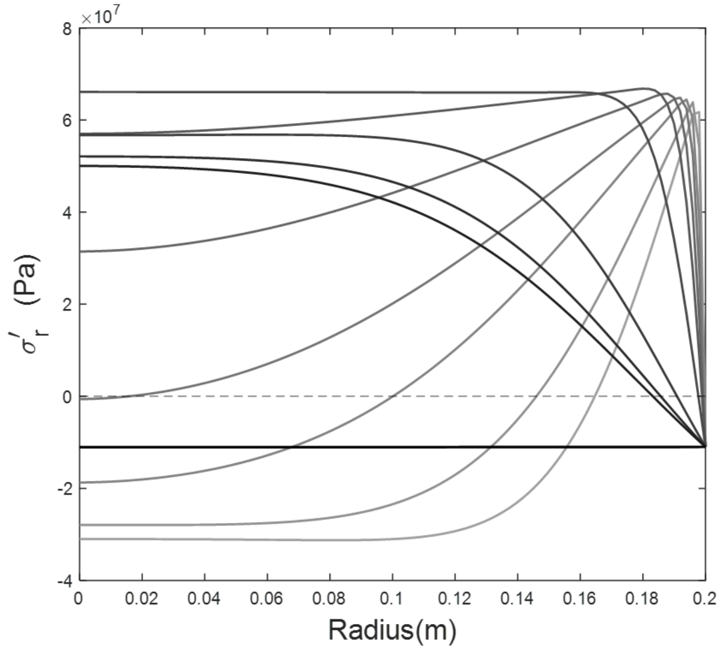

Figure 22 Effective radial stress of cement, with tension positive, where the curves grade from gray to black as time increases (boundary conditions and input values of each parameter are stated at Eq.3-35).

3.6 Pairwise Bivariate Analysis and Dimensional Analysis

The system behaviors discussed so far depend on the different values of input parameters and the mutual interactions of the physical processes they determine. If some of these parameters take on different values, the results can be much different. Thus, it is important to investigate the potential prevalence of the high pore pressure generation and its associated generation of tensile effective stress. The analysis starts with assigning values at random to each parameter within a certain range, as summarized in Table 6. Once these variables have been given values according to this Monte Carlo approach, they are substituted into the semi-analytical solution and a new solution is thus computed. For each solution, the most tensile effective radial stress at any location and any time is extracted from the data and then used to classify the case as “tensile” or “compressive”. The details of the above-mentioned procedures are summarized in the flowchart in Figure 23.

Table 6 Lower boundary and upper boundary for Monte Carlo Sampling

	Lower Boundary	Upper Boundary	Unit
α	0.5	0.95	---
B	0.5	0.98	---
β_v	1E-5	1E-3	K^{-1}
G	12E9	24E9	$N \cdot m^{-2}$
v	0.22	0.32	---
k	1E-21	1E-16	m^2
k_t	1E0	1E2	$W \cdot K^{-1} \cdot m^{-1}$
k_{tp}	1E-6	1E-9	$m^2 \cdot s^{-1}$
k_{pt}	1E-22	1E-19	$m^2 \cdot s^{-1} \cdot K^{-1}$
m_d	1E5	1E7	$J \cdot m^{-3} \cdot K^{-1}$

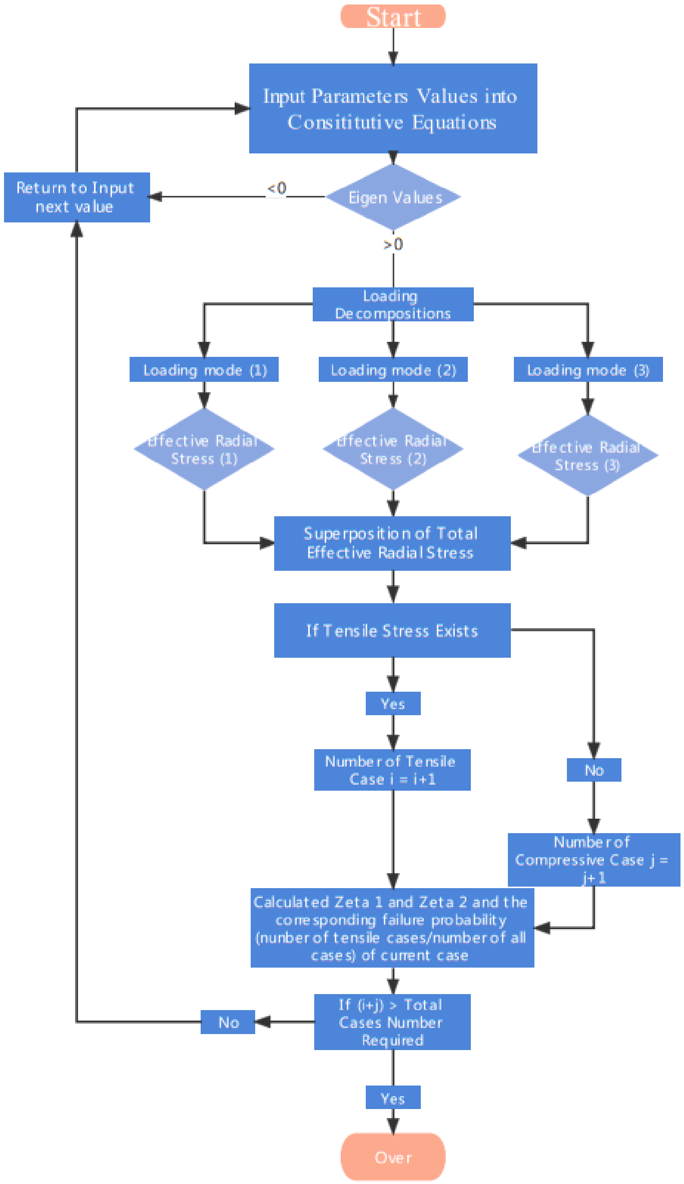

Figure 23 The algorithm that is used to construct the parametric studies.

3.6.1 Pairwise Bivariate Analysis for Each Variable

Following the procedures detailed in the flowchart described in Figure 23, a total of 3000 cases are calculated and then categorized into two groups: tensile (1914 cases) and compressive (1217 cases). Next, the relationship between each variable and the outcome of "tensile" is examined by the pairwise bivariate distributions that are shown in Figure 24. The non-diagonal elements are scatter plots which display the correlation between two variables and give insight on the distribution features of these variables. The matrix of the results is symmetric about its diagonal. The diagonal elements are univariate distribution plots which are drawn to show the probability density function of each variable. Based on the information provided by the diagonal components, it can be found that in the events of a tensile case, the specific heat and permeability are more concentrated at their lower range, and the thermal conductivity and the thermal expansion coefficient differences are more concentrated at their higher range, whereas the rest of the parameters are almost evenly distributed along their whole range. This indicates a general trend that, within the framework of PTEOF, at higher values of β_v, k_t and lower values of k and m_d will increase the propensity for generating tensile radial effective stress increases.

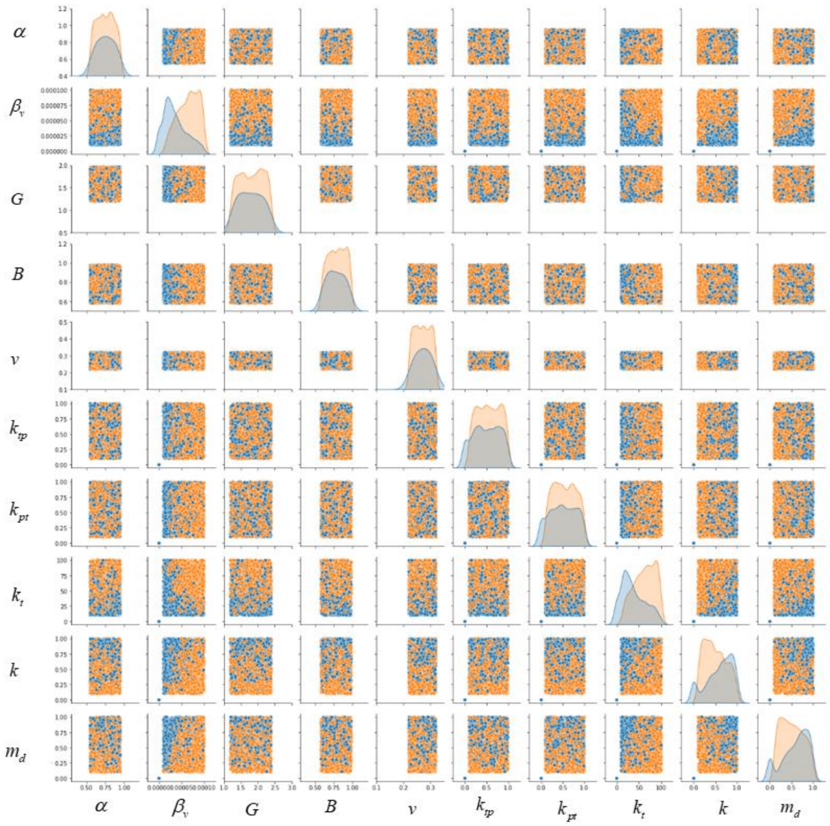

Figure 24 Pairwise bivariate distributions for eleven variables. The blue distribution on diagonals indicate distribution of the parameters for comparative cases, while orange shows distribution for tensile.

The impact of permeability on tendency to generate tension is a point that bears further discussion. One common cement design principle is that lower hydraulic conductivity is synonymous with a better cement barrier. This cement designing philosophy is possibly effective under many working conditions (i.e., ambient temperature and pressure) for which cement is originally developed. However, when the cement is placed under HTHP conditions, and poromechanics are taken into consideration, our results show that the lower permeability will actually increase the probability of the cement experiencing tensile effective stress, which can be detrimental to the integrity of the cementing system. This is mainly due to the fact that under the framework of porous media, the lower permeability will greatly slow down the pore fluid diffusion process when the pore pressure is rapidly built up within the cement due to the HTHP boundary conditions. Hence, the pursuit of low permeability regardless of the intrinsic porous properties of the cement itself and without guidance from poromechanical models could instead increase likelihood of degradation of the cement and hence reduce its effectiveness at providing mechanical support and zonal isolation. In other words, there is a negative aspect to having permeability that is too low, which we will henceforth call a “permeability penalty”. To avoid the permeability penalty for cementing design under HTHP, perhaps the most favorable solution is to keep the permeability at certain ranges which can achieve the sealing function, but at the same time, allowing the diffusion of pore pressure that is built up by the HTHP conditions and therefore not cause unnecessary damage induced by the excess pore pressure. This permeability-forgiveness design is actually very popular in pavement design of permeable porous systems (PPS) (Scholz et al., 2007) where one or two special drainage layers with relatively higher permeability are designed to reduce the runoff rates during storms while providing a hard surface for the traffic flow. The PPS design has been successfully turned into wide variety of residential, commercial, and industrial applications in the last two decades (Drake et al., 2013). Furthermore, finding a suitable permeability window should in principle be possible for wellbore cementing owing to the vast difference between the length scale associated with drainage of pore pressure to a radial boundary and the length scale associated with fluid diffusion through the length of the barrier. A permeability that is high enough to allow the former while preventing the latter should be attainable.

It also worth mentioning that the specific heat capacity has received little attention in previous research of HTHP cementing design. However, based on our results, it does play a very important role, because a large specific heat capacity will effectively slow down the heat transfer process and hence reduce the tendency to generate thermally-induced pore pressure. This will give the pore-pressure more time to dissipate compared to the rate of its build-up. This observation suggests a new direction for creating cement with high specific heat capacity and low thermal conductivity which would comprise suitable design for HTHP conditions.

3.6.2 Parameter Groups Governing Effective Stress Evolution

Although the pairwise bivariate distributions shown in Figure 24 gives a full picture of how each parameter will individually influence the system behavior, the mutual interactions of different properties and their group effects cannot be analyzed from it. To solve this problem, classical scaling and dimensional is utilized. Usually these methods are used to reduce a complex physical problem to a simpler version (at least in terms of the number of independent governing parameters) prior to obtaining a quantitative answer while also grasping the effects of various physical phenomena at the same time. With that said, it is not clear from the governing equations alone which grouping(s) of parameters have the most important effects on the propensity to generate tensile effect stress. However, by dimensional analysis and guided by the features that the diagonal elements from the pairwise bivariate distributions (Figure 24) provide, one can propose a dimensionless parameters as

$$\mathscr{Z}_1 = \frac{\alpha B c_t \beta_f}{c_f \beta_d}\,, \tag{3-37}$$

$$c_t = \frac{k_t(1 + aMg_1) - k_{pt} M(\beta_e - K_d \beta_d g_1)}{m_d - M\beta_e^{\,2} + K_d \beta_d g_2 + aM\beta_e g_2 + aMg_1 m_d + K_d M \beta_d \beta_e g_1} \tag{3-38}$$

$$c_f = \frac{k_{tp} M(ag_2 - \beta_e) + Mk(m + K_d \beta_d g_2)}{m_d - M\beta_e^{\,2} + K_d \beta_d g_2 + aM\beta_e g_2 + aMg_1 m_d + K_d M \beta_d \beta_e g_1} \tag{3-39}$$

This dimensionless group, $\mathcal{Z}_1$, consists of the Biot coefficient α, Skempton coefficient B, thermal expansion coefficient of fluid β_f and solid β_d, as well as fluid diffusivity c_f and thermal diffusivity c_t, where the last two terms are obtained from the diagonal elements of the coefficient matrix (Eq. 3-17 and Eq. 3-20). This proposed $\mathcal{Z}_1$ mainly contains the hydro-thermal properties of the porous media. It is thus named the Hydro-Thermal Non-Dimensional parameter (HTND).

At the same time, if the variation of fluid content ζ in Eq.(3-4) is set as zero (undrained solution), one can eliminate the volumetric stress σ in the same equation, and thus obtain $\mathcal{E}$ as

$$\mathcal{E} = g_3 p + g_4 T \text{, where } g_3 = \frac{\alpha}{K_d} - \frac{1}{BK_d}, g_4 = \beta_d + \frac{\beta_v}{\alpha}. \tag{3-40}$$

If one firstly inverts Eq. 3-32 into time domain and then inserts Eq. 3-38 into it, by integration

$$\mathcal{U} = (g_3 p + g_4 T) r / 2. \tag{3-41}$$

Then by inserting Eq. 3-39 into Eq. 3-31 in time domain, and setting up the σ_{rr} as zero given the boundary conditions of the mode 2 loading, the thermal induced pore pressure given a temperature rise is

$$p_{thermal} = \frac{\alpha_d - G g_4 - 2Gv/(1-2v) g_4}{2Gv/(1-2v) g_3 + G g_3 - \alpha} \Delta T. \tag{3-42}$$

Thus, the second proposed parameter is proposed as

$$\mathcal{Z}_2 = \frac{p_{thermal}}{\sigma_{rr\_initial}}, \tag{3-43}$$

which consists of thermal induced pore pressure ($p_{thermal}$) and the in-situ stress ($\sigma_{rr\_initial}$).

Given the newly proposed parameters, a new plot can by generated to show the tensile and compressive spatial distribution cases based on $\mathcal{Z}_1$ and $\mathcal{Z}_2$. In Figure 25(a), the same 3000 cases are replotted where the red dots represent the tensile cases and the green dots represent the compressive cases.

It can be clearly seen that the spatial distributions of the tensile and compressive cases in the $\mathcal{Z}_1$ vs. $\mathcal{Z}_2$ plot are dividing the sampling feasible area into three zones with clear boundaries: safe zone, transition zone and damage zone.

Futhermore, in Figure 25(b) where $\mathcal{Z}_1$ is equally divided into 200 intervals, the probability of generating the tensile cases in each of these intervals is calculated. If just considering $\mathcal{Z}_1$ as a safety index solely from the plugging material's perspective, it is shown that in the area where the $\mathcal{Z}_1$ are smaller than 0.07 is fully occupied by compressive cases; not a single tensile case exists in this region. It indicates no tensile failure would be expected to occur within this range under the framework of the PTEOF model (and for the particular boundary and initial conditions considered in this example).

When $\mathcal{Z}_1$ increases from 0.07 to 0.3, the probablity of generating tensile cases gradually increases up to 100%. Both tensile and compressive cases could happen in this region, but with a higher value of $\mathcal{Z}_1$, the possibility of generating a tensile case will be higher. This area is where the transition zone mostly locates.

When $\mathcal{Z}_1$ is greater than 0.3, no compressive case is exists within this range and it is fully occupied by tensile cases, which means the probality of generting a tensile cases is 100%. It is thus named the damage zone which means when designing the cement under the HTHP conditions, if the resulting $\mathcal{Z}_1$ is landing greater 0.3, tensile damage will certainly occur in the cement.

Drawing on the analyses and conclusions above, it can be clearly seen that the Shear Modulus and Poisson's ratio, which are not included in $\mathcal{Z}_1$ but traditionally considered as two of the most important mechanical properties, have very limited contribution to the system behavior when in terms of its propensity to generate poromechanical tensile effective stress.

So, this work suggests that from at least this one perspective, more attention should be put into the components that keep the value of $\mathcal{Z}_1$ below 0.07, as to avoid potential for tensile damage. For example, as shown in Figure 26, the Peak 1 is recalled from the Figure 17(b), giving a case for which $\mathcal{Z}_1$ equals to 1.26.

This case is firmly in the "damage zone". However, if the permeability of the material is increased by two orders of magnitude, the induced pressure is much lower, shown here as Peak 2. Still, the value of $\mathcal{Z}_1 = 0.21$ and Figure 25(b) suggests a probability of 92% to generate tensile effective stress. If the specific heat of Peak 2 is further increased by two orders of magnitude, the induced pore pressure will have an even more considerable reduction (Peak 3). The corresponding $\mathcal{Z}_1 = 0.03$, which is indicated in Figure 25(a) to be in the "safe zone" with negligible probability of generating tensile effective stress.

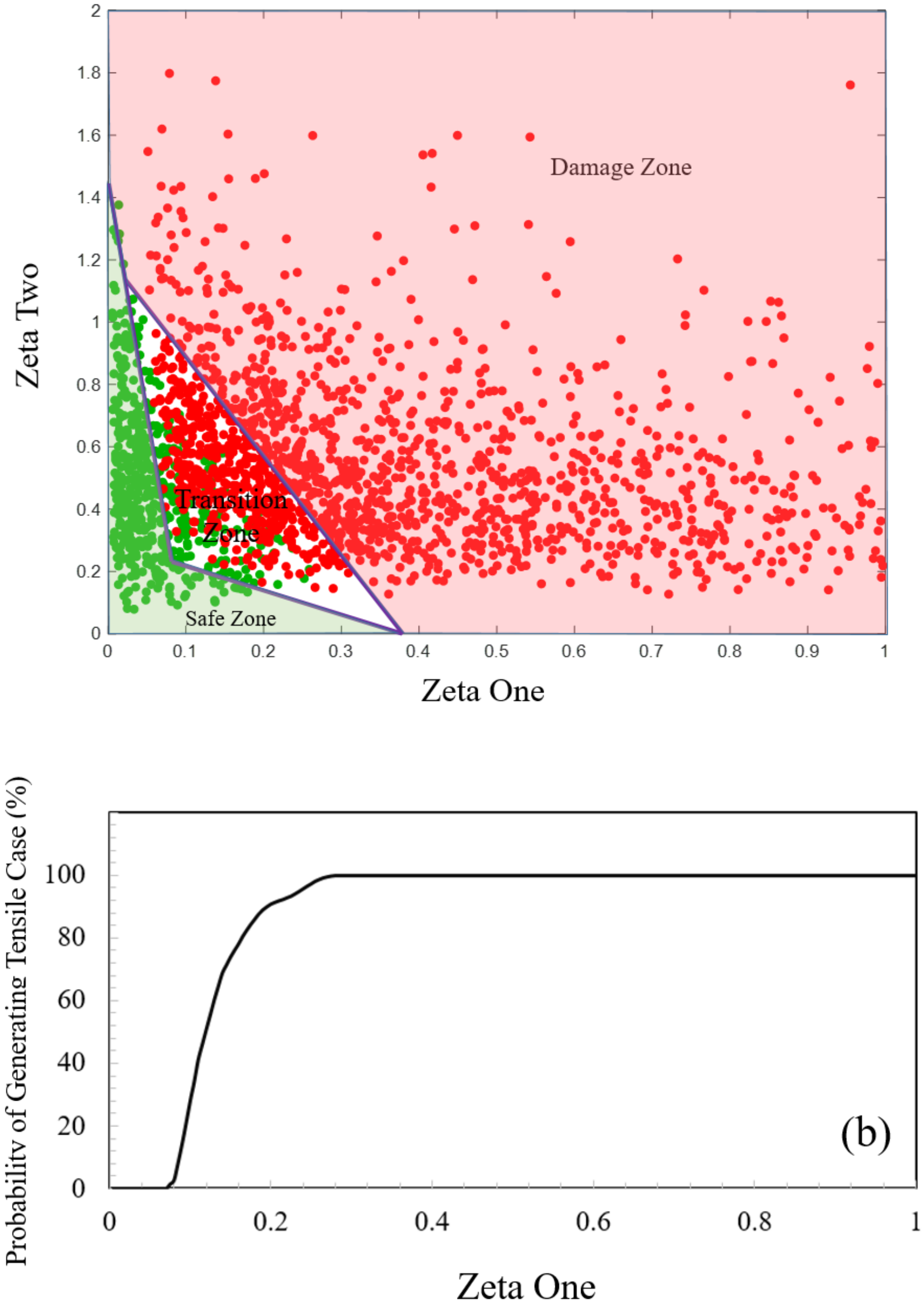

Figure 25 (a) Z1 and Z2 plot with tensile cases (red color) and compressive cases (green color). Note the range of Zeta One can be larger than 1 based on the ranges of the selected parameters. (b) The probability plot of generating tensile cases on different Z1 .

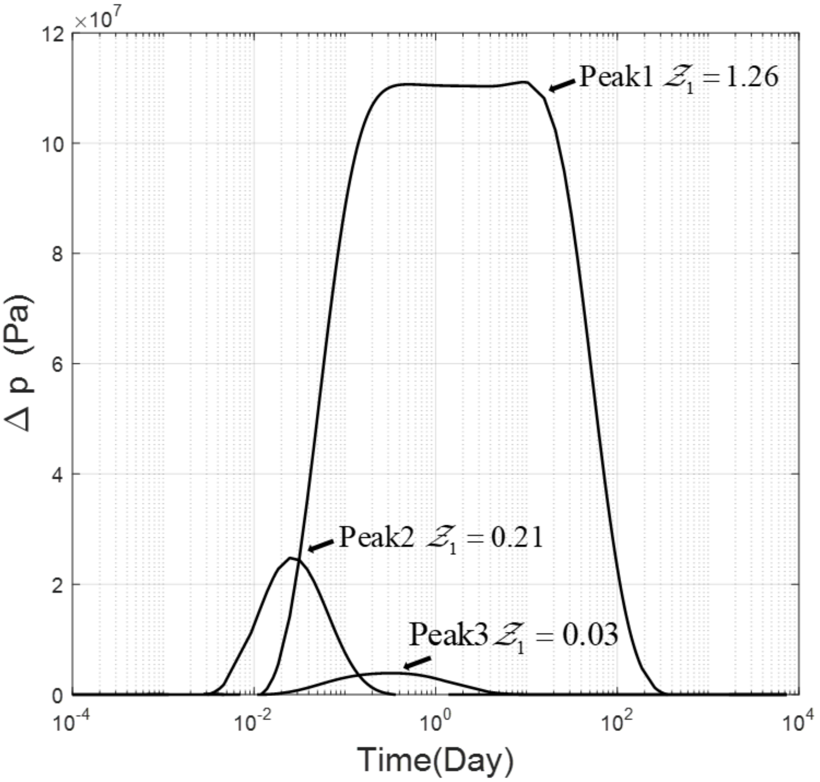

Figure 26 The influence of Zeta 1 on the Mode 2 induced pore pressure. Peak 1 is recalled from Fig. 17 Right; The permeability of Peak 2 is three orders of magnitude smaller than Peak 1, the rest of selected parameters remain the same as Peak 1; The specific heat of Peak 3 is two orders of magnitude smaller than Peak 2, the rest of selected parameters remains the same as Peak 2.

3.7 Conclusions

Using the primary cementing in P&A as an example, the fully coupled porothermoelastic-osmosis-filtration (PTEOF) model is presented here. It has been demonstrated that under HTHP conditions, the induced pore pressure in low permeability material such as cement can be so large that it can generate tensile effective stresses. This phenomenon will, in general, increase the probability of cement failure. By the pairwise bivariate analysis, the properties that are important for the HTHP cementing are parsed out. Based on these results, two new concepts are proposed in which: 1) permeability targets a desired range that is large enough to facilitate timely dissipation of pore pressure due to radial fluid flow while still giving the necessary zonal isolation by preventing axial flow through the length of the plug, and 2) seeking methods to substantially increase the specific heat of the cement. Furthermore, by scaling analysis and Monte Carlo simulation, three zones (safe, transition, and damage) with clear boundary values are shown in the $\mathcal{Z}_1$ and $\mathcal{Z}_2$ plot. Of these, $\mathcal{Z}_1$ is by far the most influential, showing that cement design with higher permeability and specific heat is expected to reduce the likelihood of pore-pressure induced failure as the cement experiences temperature changes during its service life.

A practical implication is that thermal properties, such as thermal conductivity, specific heat capacity, thermal expansion coefficient ratio, deserve more attention in cement design for HTHP conditions. The potential impact of increasing the specific heat capacity is substantial, especially because it allows mitigation of pore pressure buildup without the need to deliberately increase the hydraulic diffusivity (which may not be desirable for other reasons).

These results show the need for mechanical modeling to guide design of cementing materials for HTHP conditions. Common cement improvement practices, such as including different additives into cement to enhance its mechanical properties, will not change the fact that cement is inevitably a porous medium. While the new additive can change the pore spaces into various sizes as small as the nano-scale, without considering the underlying physical principles governing the mechanical behaviors within a poromechanical framework, modifications of properties with on objective in mind could inadvertently increase risk of failure due to another mechanism. On the other hand, guided by fully-coupled modelling, the future of cement design for HTHP conditions can be more effective by pursuing directions that may not be apparent without the use of a poromechanical model.

4.0 Prediction and Demonstration of Periodic Dilation Band Formation in Rate-Dependent Porous Cement

4.1 Chapter Summary

Periodic dilation bands are shown to occur when cylinder-shaped saturated cement specimens are subjected to rapid decompression, with the spacing between the bands scaling as a power law of the decompression time. This behavior is predicted by theory, which is specified to this scenario based on prior work that was more general and applied to compaction. Specifically, the formation of the bands is shown to coincide with periodicity that naturally arises in the effective stress when the material follows a Terzaghi-type consolidation law, although in reverse for dilation and with material deformation described by a rate-dependent viscoplastic law. When strain rate is proportional to effective stress to a power that is greater than one, periodic regions of tensile effective stress arise through the poromechanical fluid-solid coupling. The theoretically-predicted exponent of the resulting power-law relationship between dilation band spacing and unloading time successfully brackets the experimental results, for which it is observed that the exponent is slightly stronger than a square-root relationship (0.28 to 0.67) at testing temperatures of 20 ℃ and 90 ℃. These results demonstrate that rapid-depressurization leads to periodic fracturing that could, on the one hand, be detrimental to the isolation provided by cement used to seal wellbores in the petroleum industry. On the other hand, the dilation bands could also be favorable to production if generated in low-permeability reservoir rocks such as shales that are targeted for petroleum production or granites that are targeted for geothermal energy.

4.2 Introduction

Deformation bands that occur in porous geo-materials comprise one important line of evidence for the stress history of the rock. They are mainly categorized into three types of tabular geological structures: shear bands, compaction bands and dilation bands (Borja, 2004; Du Bernard et al., 2002; Eichhubl et al., 2010; Fossen et al., 2007; Gapais, 1989; Issen et al., 2000; Wolf et al., 2003). Many of these deformation bands in natural rocks are low-displacement deformation zones of millimeters to centimeters thickness that tend to have different cohesion and permeability compared with ordinary fractures (Fossen et al., 2007). The observable features of these deformation bands can reveal information about the local glacial history, the generation process of soft-sediment deformation or post-burial faulting. They can also significantly alter fluid flow patterns by their impact on the permeability of the geo-materials, in some cases by several orders of magnitude (Antonellini et al., 1994, 1995; Fossen et al., 2007; Jamison et al., 1982; Pittman, 1981). As one example, Sigda et al. (1999) found that the deformation bands that occur in the low porosity formations can induce flow channeling which can determine pathways for groundwater flow through the Vadose zone. This channelization phenomenon can also be observed during the production of a petroleum reservoir where deformation bands may be forming in low-permeability reservoir rocks during the stimulation phase of reservoir development (Fossen et al., 2007).

Given the distinctive characteristics of the deformation bands and information they can provide for geoscientists and engineers, considerable attention has been devoted to understanding the conditions and mechanisms that control their formation. It has been previously concluded that factors such as porosity, mineralogy, and grain size and shape will have some influence on the deformation band formations, but they are mainly controlled by three main factors (Fossen et al., 2007; Olsson, 1999; Rudnicki et al., 1975). These are: 1) geometry (kinematic boundary conditions, layering, etc.), 2) the constitutive response of the material (viscous, elastic, viscoelastic, etc.), and 3) the under-pinning multi-physical coupling and competitions processes.

Band width and spacing, which is one of the most readily observable of their features, are a focal point of many studies including recent reviews (Jacquey et al., 2021; Regenauer-Lieb et al., 2013). Based on the classical constitutive modeling approach from elasticity and plasticity, and combining the multi-physical coupling processes with their respective length and time, an overarching feature is the explicit emergence, at various scales, of deformation bands as dissipative patterns from the behavior of the energy equations. The body of previous literature also provides a sound basis to incorporate multiple physical principles such as coupling the laws of thermodynamics, material balances, and constitutive models and, as one might expect, each physical principle brings characteristic length and/or time scales thereby leading to different length and time scales associated with the predicted emergence of deformation bands.

One research area focuses on deformation bands associated with fundamentally slow processes, for example examining formations of these patterns in response to tectonic strain rates in the range of 10^{-12} to 10^{-16} s^{-1} (Jackson et al., 1986; Pfiffner et al., 1982). However, at the other end of the spectrum in terms of characteristic time scales, deformation bands could also be induced in low-permeability porous geo-materials such as shale and cement from engineering processes which involve rapid pressurization/depressurization. Such rapid processes can come at the beginning of a well's life, for example, from pressure fluctuations induced by reservoir stimulation (i.e. hydraulic fracturing). They can also come at the end of a well's life, for example from the rapid depressurization required as a part of a canonical cement plug test that is often required in order to verify integrity as a part of permanent plugging and abandoning of wells (Khalifeh et al., 2020). Because they involve changes in stresses and/or fluid pressures that are of a similar order to the strength of the rock (order of tens of MPa) over timeframes where pore pressure often cannot drain (seconds to tens of minutes), these engineering processes have potential to induce failure of geomaterials due to coupled poromechanical processes (see e.g. Detournay et al. (2000); Lu et al. ; Pearson (1981); Schmitt et al. (1989)).

With there being a possibility of cement and rock to fail as a result of rapid engineering processes, the tendency of failing geomaterials to form periodic deformation structures is important to understand if such material failure is to be either avoided (i.e. for cement integrity) or pursued (i.e. for reservoir stimulation). Past investigations mainly focus on compaction and shear bands (Baud et al., 2004; Bésuelle, 2001; Okubo et al., 2005; Olsson et al., 2000; Olsson, 1999; Olsson et al., 2004; Wong et al., 2001). As for dilation bands, they have been previously observed in highly porous media (Du Bernard et al., 2002). However, little (possibly no) experimental evidence of the formation of dilation bands in low-permeability materials has been observed and reported in the literature. As a result, the mechanism of the formation of dilation bands is a knowledge gap that is addressed here by showing that dilation bands occur in experiments performed in the laboratory on low-permeability, low-porosity cement when it is subjected to rapid reduction in applied stress (decompression). After reviewing a recent theoretical framework for compaction band spacing predictions, this paper extends this theory to the dilation bands family and presents a series of experimental demonstrations. Furthermore, discussions of the implications for practice, especially the methods used for cement plug verification which could be damage the integrity they are intended to ensure are also included.

4.3 Governing Equations of Periodic Dilation Band Theory

A theoretical framework for prediction of deformation bands was recently developed by (Veveakis et al., 2015) and Jacquey et al. (2021). The prior work is more general at first and then is specified to a form that describes compaction bands under 1D strain conditions. An alternate derivation and summary that is instead targeted to the present interest of dilation bands begin with a simplified one dimensional (1D) problem formulation where the orientation of the coordinate system (denoted with coordinate *z*) is selected according to the approach of Issen et al. (2000) so as to be orthogonal to the anticipated orientation of compaction/dilation bands. Expressing stress equilibrium in the *z* direction for a material with no body force and under static conditions, as well as stating the definition of Terzaghi's effective stress, gives

$$\frac{d\sigma_{zz}}{dz} = 0\,, \tag{4-1}$$

$$\sigma'_{zz} = \sigma_{zz} - p\,. \tag{4-2}$$

Here σ_{zz} is the normal total stress acting in the z direction, σ'_{zz} is Terzaghi's effective stress (the part of the total stress that is bearing on the solid matrix), and *p* is the pore pressure. Combining these leads to

$$\frac{\partial \sigma'_{zz}}{\partial z} = -\frac{\partial p}{\partial z}\,, \tag{4-3}$$

Note that compressive stresses are taken to be positive in this sign convention.

Next one needs to express mass balances. This begins for a saturated porous medium by defining the partial densities of solid skeleton phase (ρ_s) and fluid phase (ρ_f). These are defined as mass of skeleton and mass of fluid over the volume of porous material, respectively. These relate to the density of each constituent (i.e. the mass of solid over volume of solid and mass of fluid over volume of fluid) via porosity n, via

$$\rho_s = (1-n)\rho_1, \tag{4-4}$$

$$\rho_f = n\rho_2. \tag{4-5}$$

Here we denote the constituent densities as $\rho_i (i=1,2)$, where 1 represents the solid skeleton and 2 represents the fluid. Then in the general case where local mass exchange between the matrix and the voids (i.e. pores) is allowed, the mass balance equations for the solid and fluid phases are (Veveakis et al., 2015)

$$\frac{1-n}{\rho_s}\frac{\partial \rho_s}{\partial t} - \frac{\partial n}{\partial t} - \frac{\partial n v_z^s}{\partial x_z} + \frac{\partial v_z^s}{\partial x_z} = 0, \tag{4-6}$$

$$\frac{n}{\rho_f}\frac{\partial \rho_f}{\partial t} + \frac{\partial n}{\partial t} + \frac{\partial n v_z^f}{\partial x_z} = 0, \tag{4-7}$$

In these expressions, v_z^s and v_z^f are the partial velocities of the solid and fluid in the *z*-direction, respectively. Furthermore, if the solid and fluid phases are both considered as incompressible, i.e., when ρ_s and ρ_f are constant, Eq.(4-6) and Eq. (4-7) reduce to

$$-\frac{\partial n}{\partial t} - \frac{\partial n v_z^s}{\partial z} + \frac{\partial v_z^s}{\partial z} = 0, \tag{4-8}$$

$$\frac{\partial n}{\partial t} + \frac{\partial n v_z^f}{\partial z} = 0. \tag{4-9}$$

By summing Eq.(4-8) and Eq.(4-9), the mass balance equation of the mixture is obtained as

$$\frac{\partial n(v_z^s - v_z^f)}{\partial z} + \frac{\partial v_z^s}{\partial z} = 0. \tag{4-10}$$

Next we introduce the classical expression of the Gersevanov filter velocity $n(v_z^f - v_z^s)$ given by (Gersevanov, 1937)

$$n(v_z^f - v_z^s) = -\frac{k_\pi}{\mu_f}\frac{\partial p}{\partial z} + \rho g + h.o.t., \tag{4-11}$$

where g is gravitational acceleration, μ_f the viscosity of the fluid ($Pa \bullet s$), and k_π permeability (m^2), which is assumed as constant in this study as commonly done in consolidation theory. Additionally, the higher order terms (h.o.t.) refer to the nonlinear models of the flux. By neglecting the higher order terms as well as the gravitationally-driven part of the flux, the Gersevanov velocity reduces to an expression of Darcy's law, that is

$$n(v_z^f - v_z^s) = -\frac{k_\pi}{\mu_f}\frac{\partial p}{\partial z}. \tag{4-12}$$

This expression of Darcy's law will be substituted to the first expression in Eq. (4-10). To address the second expression in Eq. (4-10), we recognize that it is giving rate of the normal infinitesimal strain rate in the *z*-direction ($\dot{\varepsilon}_{zz}$), that is

$$\dot{\varepsilon}_{zz} = -\frac{\partial v_z^s}{\partial z} \ , \tag{4-13}$$

Here the minus sign is from the compression-positive sign convention. The strain rate can be decomposed into elastic and plastic parts

$$\dot{\varepsilon}_{zz} = \dot{\varepsilon}_{zz}^{(e)} + \dot{\varepsilon}_{zz}^{(p)}. \tag{4-14}$$

If some linear relationship between the elastic strain rate and the effective stress is assumed (as in classical consolidation theory), then

$$\dot{\varepsilon}_{zz}^{(e)} = a\dot{\sigma}_{zz}{}', \tag{4-15}$$

where a is the compressibility. Furthermore, consider the plastic deformation to be described via a rate-dependent viscoplastic power law of the well-studied form (Borja et al., 1985; Hickman et al., 2007; Taylor, 1948)

$$\dot{\varepsilon}_{zz}^{(p)} = sgn(\sigma_{zz}{}^{'})\eta\left[\frac{\left|\sigma_{zz}{}^{'}\right|}{\sigma_{ref}}\right]^{m}, \tag{4-16}$$

where η is the creep parameter (in s^{-1}), m is the material sensitivity (Hickman et al., 2007), and σ_{ref} a reference stress which depends on the loading condition used to obtain the creep parameter and material sensitivity. The value selection of these parameters for this problem will be discussed later. For now, by substitution of Eq. (4-3), (4-13), (4-14), (4-15) and (4-16) into Eq. (4-12), one can obtain the diffusion equation that considers both elastic and plastic strain

$$\frac{\partial^2 S^{'}}{\partial \xi^2} = \frac{a\mu_f L^2}{k_\pi}\frac{\partial S^{'}}{\partial t} + sgn(S^{'})\frac{\eta\mu_f L^2}{k_\pi \sigma_{ref}} S^{'m}, \tag{4-17}$$

where $S^{'} = \frac{\sigma_{zz}{}^{'}}{\sigma_{ref}}$ and $\xi = \frac{z}{L}$. This governing equation for the effective stress can be solved provided with appropriate initial and boundary conditions along with the necessary inputs of material properties. Behavior of the solution for cases relevant to the depressurization of a cylinder is described in the next section.

4.4 Behavior of the Model

This section will investigate different solution behaviors of the governing equations. However, some simplifications and specifications will be made firstly before discussing how the value selections of the material sensitivity m will influence on the solutions of the model.

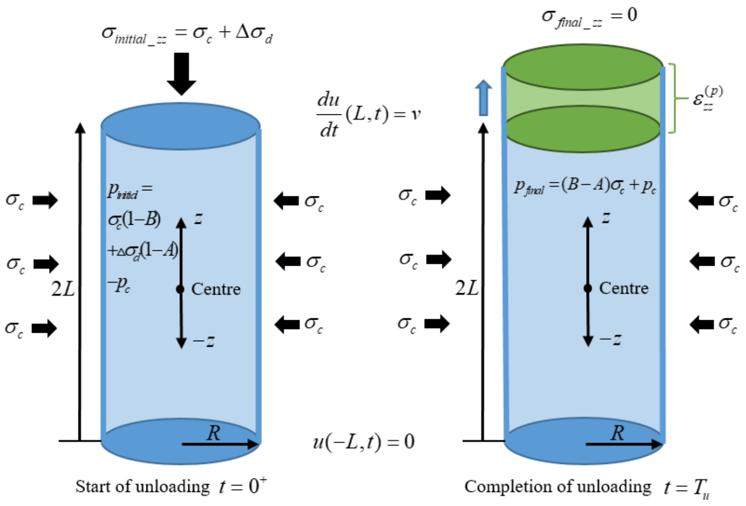

Figure 27 Illustrations of the initial and boundary conditions during dilation in the unloading progress.

Figure 27 shows a 1D cylindrical sample that is used for a convenient geometry that illustrates how the unloading can progress to generate the dilation bands. During such axial decompression under the undrained conditions, the elastic strain parts ($\varepsilon_{zz}^{(e)}$) are considered very small compared to the plastic parts ($\varepsilon_{zz}^{(p)}$) which mainly contribute to the local fluctuations and pore fluid flow. Of course, this assumption may not be valid for all materials, but in the end the consolidation theory has to do with which process generates the most change in capacity for fluid storage, i.e. the change in porosity. If most of the porosity changes in viscoplastic, the system exhibits some complex behaviors that are the focus here. So, with this assumption, the immediate response part of the Eq. (4-17) is dropped here with the idea that the elastic strain will generate very little change in porosity, so that Eq. (4-17) becomes

$$\frac{\partial^2 S^{'}}{\partial \xi^2} = sgn(S^{'}) \frac{\eta \mu_f L^2}{k_\pi \sigma_{ref}} S^{'m} . \tag{4-18}$$

Now we turn our attention to the initial conditions relevant to the problem of axial decompression. Firstly, before considering the decompression problem, we need to consider the loading stage. In this stage, the sample is loaded by a confining stress σ_c and deviatoric stress $\Delta\sigma_d$. This loading (the total stress) will be partitioned between a part that is carried by the pore fluid and a part that is carried by the solid skeleton, where the former is the pore pressure and the latter is the effective stress (recall Eq. (4-2) (Biot, 1941; Terzaghi, 1925). Furthermore, after this immediate response of the pore pressure, there is a possibility of additional transfer of the total stress from the skeleton to the pore fluid as the skeleton undergoes some permanent deformation. With these considerations, after applying and holding the initial loading, the resulting pore pressure is

$$p_{load} = B\sigma_c + A\Delta\sigma_d + p_c , \tag{4-19}$$

where A and B are Skempton pore pressure coefficients and p_c is creep-induced pore pressure. So, after applying the initial loading, the total stress is

$$\sigma_{load\_zz} = \sigma_c + \Delta\sigma_d , \tag{4-20}$$

The initial dimensionless effective stress can thus be expressed as

$$S^{'}(\xi, 0) = \frac{\sigma_{load\_zz} - p_{load}}{\sigma_{ref}} = \frac{\sigma_c(1-B) + \Delta\sigma_d(1-A) - p_c}{\sigma_{ref}} . \tag{4-21}$$

During the subsequent unloading (decompression) period, which consists of moving the top platen at a constant velocity for a travel distance (u) until the entire axial stress is zero after the total unloading time T_u , the boundary conditions are maintained as

$$u(-L,t)=0\,,\ \frac{du}{dt}(L,t)=v_z\,, \tag{4-22}$$

and the resulting plastic strain rate can be defined as

$$\dot{\varepsilon}_{zz}^{(p)}=\frac{\varepsilon_{zz}^{(p)}}{T_u}\,. \tag{4-23}$$

When the unloading is completed, the total stress in the *z*-direction returns to zero ($\sigma_{final\_zz}=0$) and, assuming sufficiently rapid unloading so that undrained conditions apply, the pore pressure (p_{final}) at this moment is

$$p_{unload}=(B-A)\sigma_c+p_c\,. \tag{4-24}$$

Thus, at the end of unloading, the effective stress is

$$\sigma_{unload\_zz}^{'}=\sigma_{unload\_zz}-p_{unload}=-((B-A)\sigma_c-p_c)\,. \tag{4-25}$$

During this decompression process, the creep parameter η and the reference stress σ_{ref} can take the value of $\dot{\varepsilon}_{zz}^{(p)}$ and $\sigma_{ref}=(B-A)\sigma_c-p_c$, respectively, as Veveakis et al. (2015) show that these value selections are valid in the compaction band framework. In the dilation process, the effective stress boundary condition in the dimensionless form is

$$S^{'}(-1)=S^{'}(1)=\frac{\sigma_{unload\_zz}^{'}}{\sigma_{ref}}=-1\,. \tag{4-26}$$

Following sign conventions mentioned above, the negative sign indicates that the effective stress is tensile which in turn results in $-sgn(S^{'})=-1$. Then, the Eq. (4-18) becomes

$$\frac{\partial^2 S'}{\partial \xi^2} + \zeta S'^m = 0, \qquad (4\text{-}27)$$

where ζ is a dimensionless unloading rate given by

$$\zeta = \frac{\varepsilon_{zz}^{(p)}}{T_u} \frac{\mu_f L^2}{k_\pi[(B-A)\sigma_c + p_c]}. \qquad (4\text{-}28)$$

The solutions of Eq. (4-27) are dependent on material sensitivity m. For all m>1, the solution has singularities (Veveakis et al., 2010). The solution, in general, requires numerical methods. However, closed-form analytical solutions exist for m=2 and m=3 (after Regenauer-Lieb et al., 2013). The m=2 solution has some desirable features (namely, the effective stress is symmetric rather than antisymmetric about the singularities), and so we focus on the m=2 solution which is expressed as

$$S' = \frac{6}{\zeta} \wp(\xi + c_1, 0, c_2), \text{ when } m = 2; \qquad (4\text{-}29)$$

where $\wp(u, \omega_1, \omega_2)$ is the Weierstrass P function(Abramowitz et al., 1964). Taking the coefficient $c_1 = 0$ ensures the symmetrical distributions of S' about the center ($\xi = 0$) of the specimen along the ξ direction. With this symmetry, the boundary conditions from Eq. (4-26) can both be satisfied by appropriate selection of c_2, which is the solution of a transcendental equation obtained by expression Eq. (4-29) at $\xi = \pm 1$. The value of c_2 is therefore dependent on the ζ value, and so must be solved numerically for each given value of ζ. The result is a family of solutions that depend on ζ, as shown in Figure 28. Clearly the solution is characterized by periodic singularities, which generate periodically-distributed regions of tensile effective stress and therefore have the potential to generate periodic tensile fracturing, i.e. “dilation bands”.

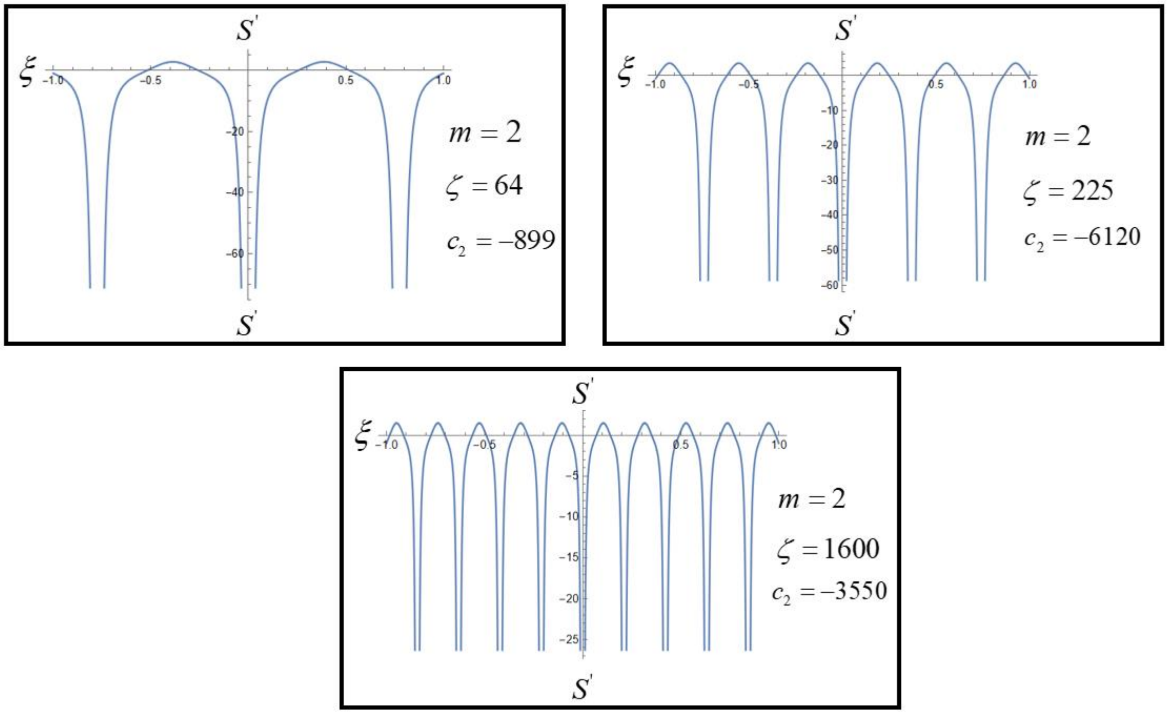

Figure 28 Different solution behaviors of when material sensitivity m and Zeta is taking different values.

In the Discussion section that is to follow, we will reflect on the physical nature of the coupling that leads to periodic regions of tensile effective stress. At this point, we will focus on the dependence of the period of the tensile stress regions on ζ with the anticipation that we can vary this quantity in the laboratory by varying the unloading rate and in this sense test the utility of the model for predicting dependence of the dilation band spacing on unloading rate. To this point, when $m = 2$, the number of singularities (N) on the domain $-1 \leq \xi \leq 1$ is scaling as a power law of ζ , with the exponent of the power law taking on different values depending upon the range of ζ (Figure 29). Hence, we describe the number of singularities as

$$N = \lambda \zeta^{\gamma} \tag{4-30}$$

Based on Figure 29, when ζ is in the range from ~20 to ~200, the number of singularities (N) is scaling with ζ at an exponent of 0.67. However, when ζ ranges from ~200 to ~1600, the number of singularities (N) is scaling with ζ at a smaller exponent of 0.28. Between distinctive power laws lies the region of $100 \le \zeta \le 1000$, which is of interest because it is where the number of singularities is between 2 and 7. Hence it is a region where the number could be readily observed in experiments. In this region, the behavior will not strictly follow a power law, however, if one were to fit a power law the exponent would be expected to be around ½, as illustrated by the orange color sketched line with a slope of $N \propto \zeta^{1/2}$.

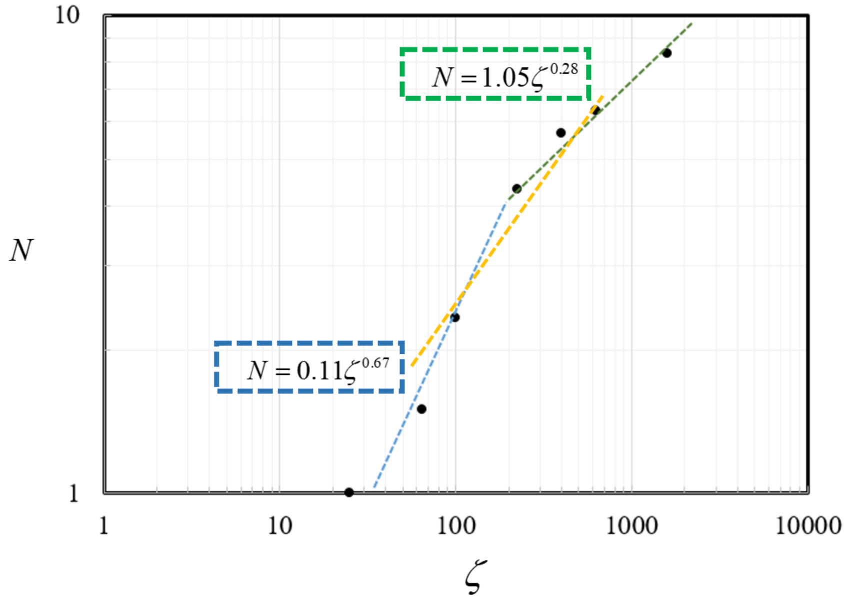

Figure 29 When m=2, two different power law relationships occur between the number of singularities (N) and Zeta based on different ranges of Zeta. The orange dash line is an illustration for fitting purpose when the exponent is 1/2.

4.5 Experimental Demonstration

4.5.1 Experimental Setup and Procedures

The decompression tests are performed in a temperature-controlled Hoek-type triaxial cell. This system consists of three main parts: axial loading system, confining stress system, and temperature-control system (Figure 30). The deviatoric loading is controlled by an INSTRON-600DX load frame, which can provide up to 600KN. The confining stress is maintained by a high-pressure syringe pump (ISCO-260D), which is also allowing precise measurement of the volume change of the specimen associated with a given confining stress up to 70 MPa. The temperature is provided by wrapping the Hoek cell with the heating tape that can provide a controlled temperature up to 180°C.

In the experimental procedure for performing the decompression tests, the cylindrical specimen (60 mm height; 30 mm diameter) is kept in fully saturated conditions until the test starts. Then the specimen is placed into the membrane, which is specially designed to attach to the cell so that the whole system remains airtight (Figure 31). After the membrane with a specimen inside is placed into the Hoek cell, hydraulic oil is pumped into the space between membrane and cell so the lateral pressure can be provided. The specimen is axially enclosed by two steel loading plates (top-loading plate and bottom spacer). The top vertical piston of the load frame directly contacts the top-loading plate so the deviatoric load can be applied. By using heating tape wrapped around the Hoek cell, the temperature of the cell is slowly increased to the targeted temperature, i.e., 90℃, over two to three hours while maintaining a low hydrostatic (both confining and axial) applied stress of 1.4 MPa. Note that by requiring hours for the heating process, it is possible to drive some evaporation of pore fluid so that the specimen can potentially deviate from fully saturated conditions. The airtight seal between membrane and specimen and the tight contact between the steel platens and the ends of the specimen is relied upon to prevent evaporation, which is one motivation to perform the heating under a hydrostatic applied stress.

After the desired system temperature is achieved and stabilized, the confining pressure and vertical load are increased to the targeted pressure value of 13.7 MPa, so the specimen is initially loaded isotropically. Next, the deviatoric load is increased to the targeted value of 20.7 MPa and held for a short period of time (around 15 minutes) to make sure the system is stabilized.

After this holding period (akin to the initial loading described in the previous section), the the axial stress is released by prescribing a set rate of motion of the actuator that is responsible for applying the axial load. During this time, the axial load is completely released, and the radial load is still maintained at the value of the confining stress.

This comprises the experiment as far as the mechanisms of interest are concerned. Hence, the final unloading of the radial stress is done very slowly, after which the specimen is removed for inspection and measurement. These are done both visually and by scanning by a North Star Imaging M-5000 Computed Tomography (CT) scanner with Feinfocus FXE source at 185 kV and 200 mA.

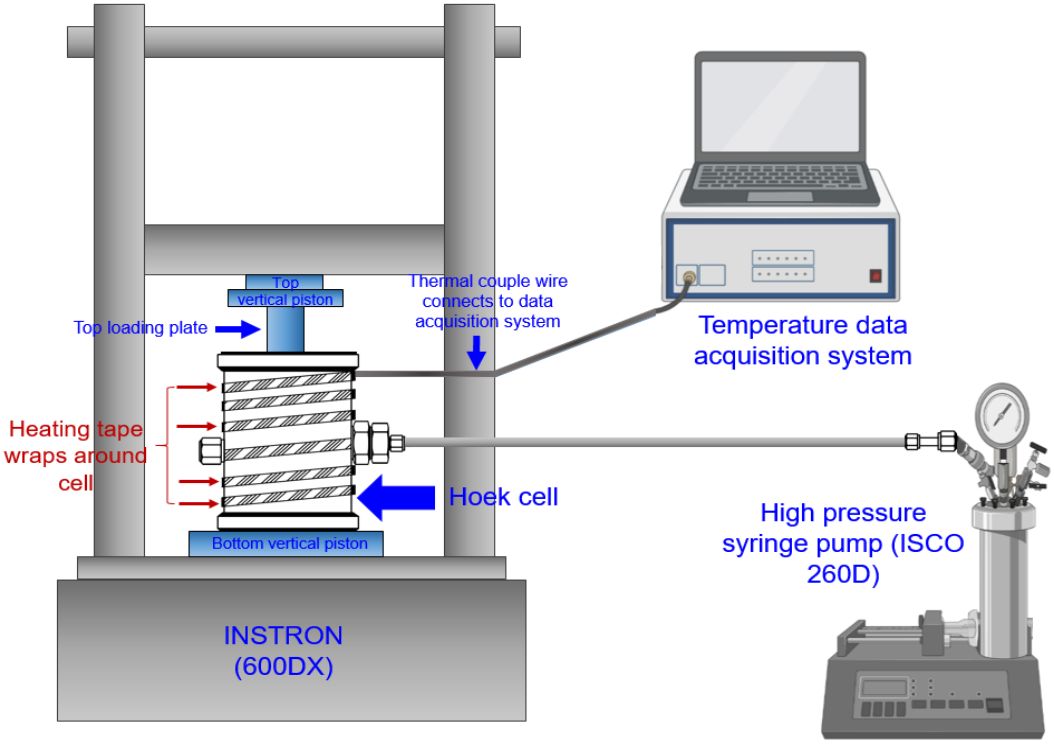

Figure 30 Experimental setup of the decompression tests, includes the axial loading system, confining stress system, and temperature-control system.

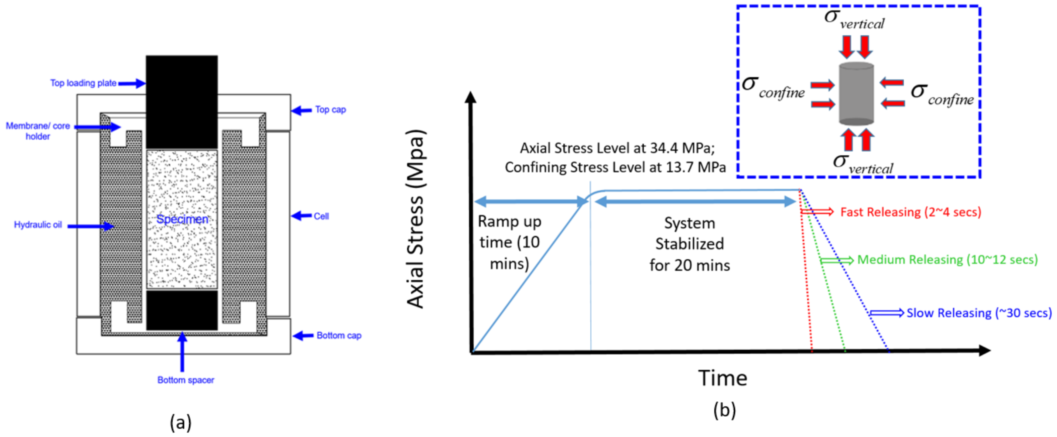

Figure 31 (a) The internal structure of the Hoek-cell; (b) Specimen with its boundary conditions and the loading and unloading paths.

4.5.2 Experimental Results

The observed fractures (the locations are indicated as green arrows) and their spacing from the experiment are shown in Figure 32. Note that there are two types of fractures that are observed. Taking the fast release at room temperature (top left corner) as an example, fractures (f1, f2, and f3) are penetrating-through fractures which are completely separating the whole cross section of the sample. These fractures can be observed by visual inspection. However, the internal fractures (f4 and f5) are not visible by inspection of the outer surfaces of the specimen, but they are visible in the CT scans. The spacing between these experimental observed fractures and the corresponding unloading time to generate these fractures are summarized in Table 7.

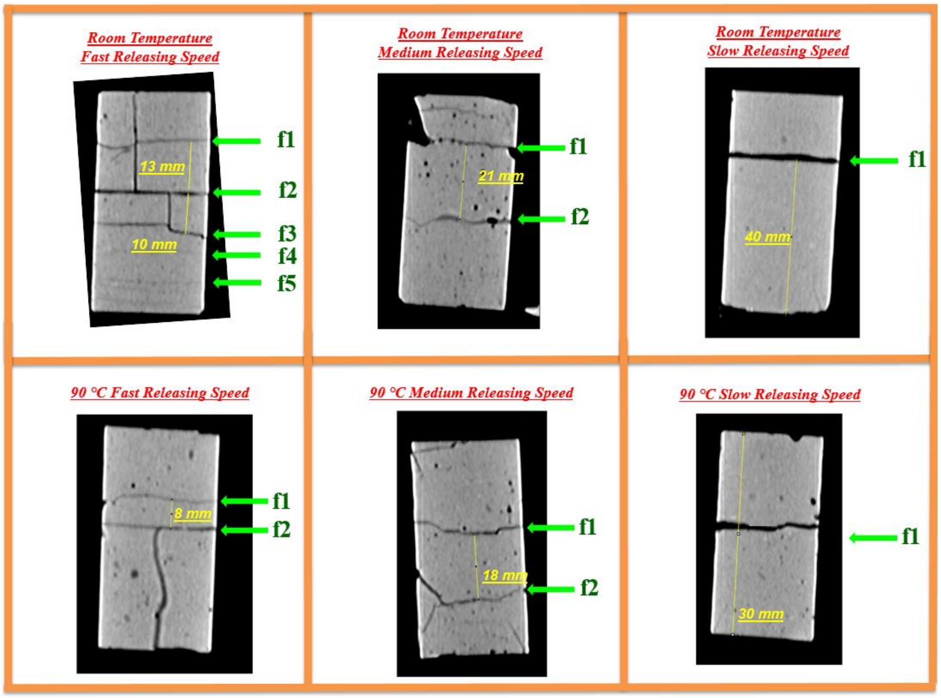

Figure 32 Measurement of tensile bands spacing occurs during decompression test at room temperature and 90 C. The location of each observed fractures is indicated and labeled by an arrow on the right side.

Table 7 Unloading time and experimental measured spacing of each specimen in Figure 32

Testing Temperature	Unloading Time (s)	Experimental Measured Spacing (mm)
Room Temperature	3 (fast)	11.5
Room Temperature	11 (medium)	21
Room Temperature	30 (slow)	40
90°C	3 (fast)	8
90°C	11 (medium)	18
90°C	30 (slow)	30

4.6 Discussions

Knowing the sample length (2L) and the predicted number of singularities, a relationship for the spacing between singularities (fractures) h and the unloading time (T_U) is obtained as

$$h = \frac{2L}{N} = \frac{2L}{\lambda}\left[\frac{\varepsilon_{zz}^{(p)}}{T_u}\frac{\mu L^2}{k_\pi[(B-A)\sigma_c + p_c]}\right]^{-\gamma} \propto T_u^{\gamma}\,. \tag{4-31}$$

As discussed in the last section, the exponent γ is dependent on the parameters of m and ζ . Its range is from 0.28 to 0.67 when m=2. As shown in Figure 33, the power law relationship between the experimental observed spacing and the unloading time is plotted in log-log space, the exponent at high temperature (90℃) is found as 0.5764 with R^2 = 0.9968 and the exponent at room temperature (20℃) is found as 0.5376 with R^2 =0.9913. These reported values are falling into the reasonable ranges of exponents when m=2. This is especially true when considering that the total number of observed dilation bands is consistent with ζ being in the range of 100 to 1000. For m=2, if one had only three of the model predictions across this limited range, inspection of Figure 29 shows that the apparent exponent of a power law would be near 0.5. Hence, these experimental results give support to the scaling relationships between the numbers of tensile effective stress regions and ζ based on the theoretical framework of periodic dilation band formation in rate-dependent porous materials.

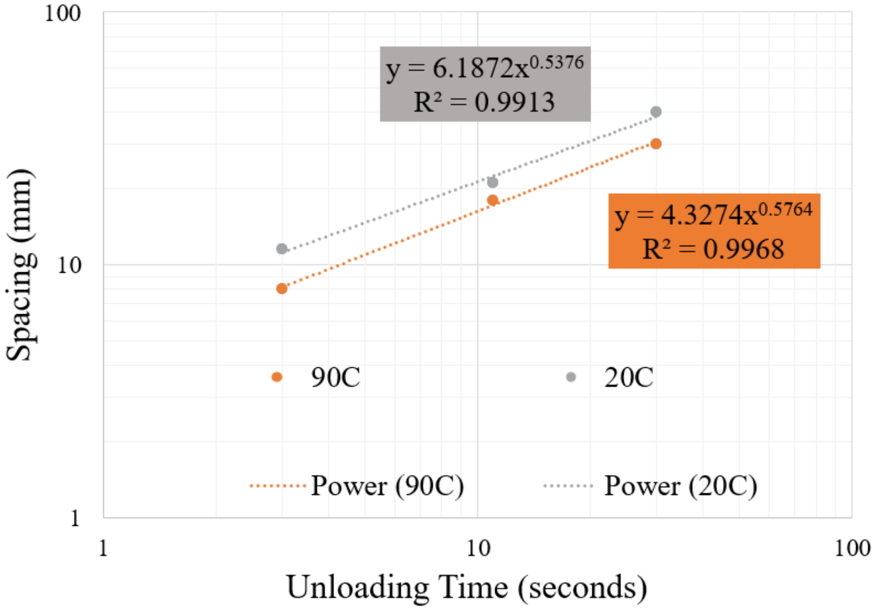

Figure 33 Power law relationship between unloading time and spacing from the experimental observation is summarized in Table 7.

Post-experiment inspection of the fracture surface shows no evidence of crushing, pore collapse, or sliding. Hence it is consistent with a tensile mechanism and stands in contrast with prior work on deformation bands of different modes that show evidence of grain translation, shear displacement, or even crushing in poorly consolidated sand and sandstone (Du Bernard et al., 2002). It is therefore worth reflecting on the coupled mechanisms that lead to the formation of these dilation bands (DBs).

Beginning from the moment the axial load begins to be removed from the specimen, the internal coupling becomes complex as the movement of the fluid (following diffusion law) and movement of the solid (viscoplastic law) interplay. Because the starting point is the conservation of both solid and fluid phases, the movement of these phases must be counter to one another. That is, as the solid deforms and thus moves in a certain direction, mass balance requires there to be a counterflow of fluid. So, if we examine what happens in the moments leading up to the sample being completely unloaded in the axial direction, there is a dilation process relative to the loaded state. Because of the pore pressure generated during the loading that is then unable to be dissipated on the rapid timescale of the unloading, the effective stress becomes negative (tensile) everywhere. By the viscoplastic law, the volumetric strain rate has the same sign as the effective stress, which means the sample is volumetrically dilating.

If this dilation is initially uniform, consider what would happen if there is a small perturbation locally within the specimen to be even smaller (more tensile). By the viscoplastic law, the dilational strain rate will become even greater at that location. This dilational strain amounts to a movement of the solid phase away from the location of the perturbation. But, throughout this process, the total stress must remain constant in order to satisfy equilibrium, which means that the reduction of the solid phase at that location will transfer more of the load to the fluid phase. This will elevate the pore pressure at the location of the perturbation, thus leading the effective stress to become even more negative. This leads to a further acceleration of the local strain (dilation) and an additional transfer of load to the pore fluid, raising the pore pressure and thus further decreasing effective stress in order to maintain constant total stress. In this way, a local perturbation can grow unstably unless it is somehow mitigated by the rate at which fluid pressure can equilibrate between the local perturbation with high pore pressure and the “far-field” relative to the perturbation with low pore pressure. In this regard, the dilation bands can be seen as a form of material instability existing in a coupled poromechanical system, eventually leading to a separation of the solid phase into a dilation band (as illustrated in Figure 34).

With this in mind, the solution to the coupled governing equations is therefore indicating the natural spacing that is predicted to arise as some perturbations grow and others are suppressed, with growth and suppression representing a competition between the rate of solid deformation and the rate at which diffusion can dissipate accumulating pore pressure. This competition is indeed embodied in the form of the dimensionless strain rate, ζ , which is directly proportional to the solid strain rate and inversely proportional to the fluid diffusivity (permeability over fluid viscosity). When this ratio is small (higher diffusivity and/or lower strain rate), the fluid diffusion can take place at a larger scale and so the spacing between tensile regions is larger. When this ratio is higher (smaller diffusivity and/or higher strain rate), fluid diffusion can only occur at a smaller scale and so the spacing between tensile regions resulting from this coupled process becomes smaller.

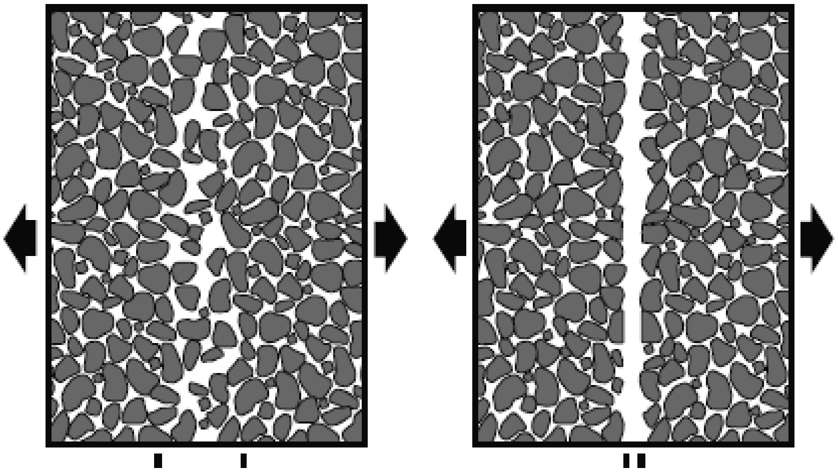

Figure 34 Left: Compaction band surface is characterized by grain translation, displacement, or even crushing in poorly consolidated sand and sandstone; Right: dilation bands surface is characterized by planar opening-mode fractures with two discrete and neat surface.

The previously-reported compaction bands are proposed to work in the opposite way. During the compaction process, where compressive total stress is applied and held as constant throughout, the effective stress is positive (compressive) everywhere in the sample. As the same viscoplastic law states, the compaction rate will become faster if there is a perturbation that causes the effective stress to be larger, which will reduce pore pressure in order to keep a constant total stress. This will in turn lead to an even larger effective stress on the solid phase and will once again reduce the pore pressure as the results of maintaining the constant total stress. This shedding process from the pore fluid to the skeleton will make the solid phase take more stress which will eventually lead to the rearrangements (translation, displacement, or even crushing) of the grains, which have been reported in the literature to be physical characteristics resulting from the formation of compaction bands (Du Bernard et al., 2002, Fossen et al., 2007, Olsson et al., 2000). The discoveries and results from the present work can be applied as a guide to several engineering processes and applications. Taking hydraulic fracturing treatments for example, at the end of each stage there is an abrupt pressure drop associated with the end of pumping. In some cases, there is immediate flowback, while in others there could be another opportunity for rapid decompression when the well is finally flowed back at the end of a multi-stage treatment at the transition to production. Our results show that such rapid depressurization at the end of pumping can induce tensile dilation bands in the well cement sheath and thus can jeopardize the well integrity. On the other hand, if rapid depressurization is translated into the reservoir and occurs in the vicinity of the hydraulic fractures, there could be a generation of secondary fractures as dilation bands with could impact fluid flow and contribute positively to production.

Another scenario that could be leading to the occurrence of dilation bands is the process of plug verification during well plug and abandonment. Currently, none of the industrial codes delineates the appropriate loading/unloading rates for the hydraulic pressure tests which are used to verify the zonal isolation functionalities of permanent cement plugs. Because the cement is low permeability and likely rate-sensitive (recall the material used in this study is wellbore cement), it is possible that the load/unload cycle of pressure used for plug verification could, somewhat ironically, be causing damage in the form of induced dilation bands. In fact, the "better" the cement is, in the sense of having lower permeability the more susceptible it will be to dilation band formation and the associated damage to its material properties. This points to a material design tradeoff, guided by Eq. (4-32), wherein cement plug material should be low enough permeability to ensure zonal isolation, but high enough permeability so that the risk of damage due to dilation band formation is at an acceptable level in light of the anticipated loading/unloading rates to which it will be subjected.

4.7 Conclusions

A theoretical framework capturing the coupling between fluid diffusion and viscoplastic solid deformation predicts that periodic regions of tensile effective stress could form as a result of rapid depressurization of a low-permeability, rate-dependent porous material. This solution for the effective stress $S^{'}$ is dependent on the material rate-sensitivity exponent m and a dimensionless strain rate ζ , where the latter embodies a comparison between the viscoplastic solid deformation rate and the diffusive dissipation of pore pressure. Mathematical solutions point to power law scaling relationships between the number of tensile zones and the dimensionless strain rate, where a higher dimensionless strain rate (i.e. higher actual strain rate and/or smaller diffusivity of the porous material) results in more closely-spaced regions of tensile stress. More specifically, there are at least two distinct zones with different power laws, one for smaller values of ζ and another for larger values, with the transition occurring when this quantity is in the hundreds.

As a proof of concept to the dilation bands predicted by theory, their emergence is observed in experiments on fully-saturated cylindrical cement samples during the decompression tests with different releasing speeds. The experimental observations show that a faster unloading time will cause a higher number of (i.e. a smaller spacing between) the periodic tensile fractures. The exponent of the power law relationship between unloading time and dilation band spacing from the experimental observations is found to fall into ranges consistent with theoretical predictions.

Based on this initial level of consistency between theory and experiment, the observed formation of the periodic dilation bands is inferred to occur when the strain rate is following a viscoplastic law and fluid flow is following Darcy's law. To satisfy mass balance, solid deformation must induce a counterflow of fluid. At the same time, whenever fluid pressure increases, it takes more of the load and so to maintain constant total stress, more load must be shifted away from the skeleton, thereby further decreasing the effective stress (making it more tensile). This positive feedback is proposed to be the underlying mechanism of dilation band formation that leads to the observation of planar opening-mode fractures with two discrete and neat surfaces in the low permeable porous materials with strong rate dependency.

The mechanism of dilation band formation could be responsible for periodic tensile fracturing in a variety of low-permeability, rate dependent porous materials such as wellbore cement and clay-rich rocks. Focusing on engineering timescales this work shows both the potential pitfalls of dilation band formation that could lead to the reduction of zonal isolation provided by wellbore cement as well as possible benefits if dilation bands form near hydraulic fractures in reservoir rocks and increase the ability of oil and gas to flow to a well. The coupling that leads to these behaviors furthermore comprises a new way to see porous materials, even at an intuitive level, as being prone to localization of dilation in a manner that is spontaneous and regular in its behavior.

5.0 Conclusions

The long-standing integrity issues of P&A in the deep-well system have been recognized as a pollution source with potential to cause severe consequences to our environment, health, and economy. The number of wells that need to be abandoned and plugged is ever-increasing and the oil discharge from leaky wells is ongoing. However, our society – including governments, companies, and research institutions – has yet to come up with an effective solution to prevent it from happening. More importantly, to ensure the qualities of the P&A job, an appropriate time window is crucial. If it cannot be planned, designed, and operated well at the very beginning, it will be extremely difficult to fix once leakage is already happening.

The difficulty of fixing leaky wells is rooted in many reasons. One of the main causes of these leaks is the harsh conditions where the cementing materials are threatened by the HTHP, acidic geofluid and mud contaminations in the geological timeframe. Stopping this leakage problem can therefore be difficult due to the insufficient performance of the current cementing materials, which are initially designed to perform under ambient temperature and pressure in the service life of 20-30 years. Furthermore, although the P&A system has multiple barriers to safeguard against leaks, once one of the barriers is broken, the rest of the system can eventually fail due to a chain of exposures set off by the initial failure. As such, leaky wellbores can persist for decades, resulting in cumulative damaging effects through the continuous release of Hydro-Carbon (HC) into the environment.

Inspired by work on the reaction kinetics associated with geochemical alteration of ultramafic minerals, the first part of this research shows an entirely new cementing material which turns the challenging deep-well conditions into an advantage, by providing the necessary acceleration of both the hydration and carbonation reactions that turn granular ultramafic raw materials into cemented rock, dubbed here as "Geologically Activated Cement" (GAC). Batch reactions run under simulated deep well conditions explore reactions between olivine sand, water, CO_2, and other chemical additives. The reaction products are analyzed and identified by X-ray powder diffraction (XRD), scanning electron microscope (SEM), and Energy-dispersive X-ray spectroscopy (EDS). These proof-of-concept experiments demonstrate that within the hours to days relevant to P&A operational timeframes, the magnesium silicate-based, solid, rock-like material can be produced from Mg_2SiO_4-CO_2 mixtures. Furthermore, the GAC is resilient to damage, as demonstrated by intentionally damaging (thermally cracking) the GAC and then subjecting it to a flow of acidic fluid under HPHT conditions. These experiments show that the GAC heals itself under well-like Chemo-Hydro-Thermo-Mechanical (CHTM) conditions within a few hours. This self-sealing ability under the challenging conditions mentioned above gives the foundations to develop a resilient wellbore sealing and plugging system in which the integrity can be restored after it is damaged and the leak problem can be reduced and controlled. It has the potential to impact this long-standing issue and is also widely-applicable to Enhanced Geothermal System (EGS), Carbon Sequestration, Storage and Utilization (CSSU) in the near future.

Besides contributing a new type of material for long-term, resilient P&A, this dissertation research contributes to the body of work that focuses on reinforcing the cement by adding various additives, which aims to provide better mechanical and hydraulic properties, in the hopes of maintaining the system integrity under the extreme conditions. However, the identification of the "better" mechanical and hydraulic properties of cement under the scenario of high temperature and high pressure (HTHP) are still unclear and it does require a more comprehensive and thorough study to highlight the challenges associated with HTHP cementing so a solution can be developed to suit these challenges. Using the primary cementing in P&A as an example, the fully coupled porothermoelastic-osmosis-filtration (PTEOF) model is presented within the second part of this dissertation. It has been demonstrated that under high-temperature and high pressure (HTHP) conditions, the induced pore pressure in low permeability material such as cement can be very large, which greatly reduces the effective stress and can even extend it into the tensile region. This reduced effective stress phenomenon will, in general, increase the probability of different types of failure of different types of cement, and these phenomena are firstly described as permeability penalty. By the pairwise bivariate analysis, the properties that are important for the HTHP cementing are found out. Based on these results, two new concepts, permeability forgiveness cement and phase-change cement, are proposed here for the future of HTHP cementing design. Furthermore, by adapting the traditional scaling analysis approach, three zones (safe, transition, and damage) with clear boundary values are shown in the Hydro-Thermal Non-Dimensional parameter and Mechanical Non-Dimensional parameter plot to give the cementing researchers and practitioners direct and meaningful guidance about how much tensile failure risk the cement is taking when it is placed under HTHP conditions. More importantly, the implications of the results challenge the prevailing HTHP cementing principles and provide a new perspective of design and guidance by addressing the porous intrinsic nature of cement. Thus, this research paves the way for designing plugging materials under HTHP conditions to have more robust and reliable zonal isolation functions, and hence wider applicability.

As a final point, this dissertation research also presents an experimental demonstration of a novel mode of failure that could be very commonly encountered in a full life span of wells that undergo rapid temperature and/or pressure cycling. It shows that if a material’s creep deformation is rapid enough compared to its ability to dissipate pore pressure build up, then it will be prone to fail through the generation of regularly and predictably spaced periodic cracks. This is the first discovery of this type of failure occurring in wellbore cements under conditions relevant to P&A operations.

In summary, this research experimentally contributes two new, resilient, self-sealing materials to improve well integrity that are ideally suited to the temperature and pressure conditions encountered in deep-wells. At the same time, the cementation and expansion from the carbonation of the ultramafic minerals (notably olivine) widens its applications in challenging conditions such as Enhanced Geothermal System (EGS), Carbon Sequestration, Storage and Utilization (CSSU) in the near future. Furthermore, the present research provides the development of a new, semi-analytical solution for the thermoporoelastic response of wellbore plugging materials to changes in stress, pressure, and temperature. It shows that plugging materials with a certain combination of material properties can be much more prone to failure when subjected to sudden temperature changes that can be encountered in P&A. The problematic combination occurs when the material has low specific heat, low hydraulic permeability, and large thermal conductivity. Unfortunately, many current efforts in wellbore plugging material development focus only on obtaining low permeability, and therefore inadvertently create materials prone to failure under geothermal conditions. By clearly elucidating the ratio of material property values that is needed for the cement to be safe from thermoporoelastic failure, this has created a new focus for research and development in well cements under HTHP conditions. Last but not least, by demonstrating and experimentally-validating a theoretical prediction for periodic cracking of cement during rapid unloading, including the spacing of the periodic cracking that comprises the cement failure, the present research shows that any excessive load and unnecessary rapid loading/unloading rate during the life span of the well could lead to periodic cracks. Such cracking is predicted to be particularly problematic when cement permeability is very low and/or susceptibility to creep deformation is very high. Hence, this research provides new guidance for future P&A operations as well as directions for developing new materials that will withstand and be resilient in the challenging subsurface environments common for oil and gas wells.

Appendix A Details of Stehfest's Method

For a given function p with Laplace transform, Stehfest's method (Stehfest, 1970) can be expressed as, taking pore pressure for example:

$$p(\xi,t)=L^{-1}\{\tilde{p}(\xi,s)\}\cong\frac{\ln 2}{t}\sum_{j=1}^{n}c_j\tilde{p}(\xi,\frac{j\ln 2}{t})\ (1)$$

Where the coefficient c_j are given by

$$c_j=(-1)^{j+n/2}\sum_{k=floor[(j+1)/2]}^{\min(j,n/2)}\frac{k^{n/2}(2k)!}{(N/2-k)!k!(k-1)!(j-k)!(2k-j)!}$$

Bibliography

Aarlott, M. M. (2016). *Cost analysis of plug and abandonment operations on the Norwegian continental shelf*. NTNU, Retrieved from http://hdl.handle.net/11250/2449646

Abdel Gawwad, H., Abd El-Aleem, S., & Faried, A. (2017). Effect of internal sulfate attack on the properties of sulfate-resisting cement and alkali-activated slag. *Geosystem Engineering, 20*(4), 195-206.

Abramowitz, M., & Stegun, I. A. (1964). *Handbook of mathematical functions with formulas, graphs, and mathematical tables* (Vol. 55): US Government printing office.

Achang, M., Yanyao, L., & Radonjic, M. (2020). A review of past, present, and future technologies for permanent plugging and abandonment of wellbores and restoration of subsurface geologic barriers. *Environmental Engineering Science, 37*(6), 395-408.

Acosta, J., Barroso, M., Mandal, B., Soares, D., Milankovic, A., Lima, L., & Piedade, T. (2017). *New-generation, circumferential ultrasonic cement-evaluation tool for thick casings: case study in ultradeepwater well.* Paper presented at the OTC Brasil, Rio de Janeiro, Brazil, October 2017. Paper number: OTC-28062-MS.

Addis, M. (1997). Reservoir depletion and its effect on wellbore stability evaluation. *International Journal of Rock Mechanics and Mining Sciences, 34*(3-4), 4. e1-4. e17.

Aggarwal, P., Singh, R. P., & Aggarwal, Y. (2015). Use of nano-silica in cement based materials—A review. *Cogent Engineering, 2*(1), 1078018.

Ahmed, S., Salehi, S., & Ezeakacha, C. (2020). Review of gas migration and wellbore leakage in liner hanger dual barrier system: Challenges and implications for industry. *Journal of Natural Gas Science and Engineering, 78*, 103284.

Allahvirdizadeh, P. (2020a). A review on geothermal wells: Well integrity issues. *Journal of cleaner production, 275*, 124009.

Allahvirdizadeh, P. (2020b). A review on geothermal wells: Well integrity issues. *Journal of Cleaner Production*, 124009.

Antonellini, M., & Aydin, A. (1994). Effect of faulting on fluid flow in porous sandstones: petrophysical properties. *AAPG bulletin, 78*(3), 355-377.

Antonellini, M., & Aydin, A. (1995). Effect of faulting on fluid flow in porous sandstones: geometry and spatial distribution. *AAPG bulletin, 79*(5), 642-671.

Ashraf, W. (2016). Carbonation of cement-based materials: Challenges and opportunities. *Construction and Building Materials, 120*, 558-570.

Ashraf, W., & Olek, J. (2016). Carbonation behavior of hydraulic and non-hydraulic calcium silicates: potential of utilizing low-lime calcium silicates in cement-based materials. *Journal of materials science, 51*(13), 6173-6191.

Ashraf, W., & Olek, J. (2018). Carbonation activated binders from pure calcium silicates: Reaction kinetics and performance controlling factors. *Cement and Concrete Composites, 93*, 85-98.

Ashraf, W., Olek, J., & Atakan, V. (2015). *A comparative study of the reactivity of calcium silicates during hydration and carbonation reactions.* Paper presented at the 14th International congress on cement chemistry, Beijing, China, 13~16 October 2015.

Bachu, S., & Bennion, D. B. (2009). Experimental assessment of brine and/or CO2 leakage through well cements at reservoir conditions. *International journal of greenhouse gas control, 3*(4), 494-501.

Banthia, N., & Mindess, S. (1989). Water permeability of cement paste. *Cement and concrete research, 19*(5), 727-736.

Barclay, I., Pellenbarg, J., Tettero, F., Pfeiffer, J., Slater, H., Staal, T., . . . Whitney, C. (2001). The beginning of the end: a review of abandonment and decommissioning practices. *Oilfield Review, 13*(4), 28-41.

Barlet-Gouédard, V., Rimmelé, G., Porcherie, O., Quisel, N., & Desroches, J. (2009). A solution against well cement degradation under CO2 geological storage environment. *International journal of greenhouse gas control, 3*(2), 206-216.

Baud, P., Klein, E., & Wong, T.-f. (2004). Compaction localization in porous sandstones: spatial evolution of damage and acoustic emission activity. *Journal of Structural Geology, 26*(4), 603-624.

Bear, J., & Corapcioglu, M. (1981). A mathematical model for consolidation in a thermoelastic aquifer due to hot water injection or pumping. *Water Resources Research, 17*(3), 723-736.

Beltrán-Jiménez, K., Skadsem, H. J., Gardner, D., Kragset, S., & Lourenco de Souza, M. I. (2019a). *Leakage Through Micro-Annulus Geometries Incorporating Pressure-Driven*

Elastic Deformation. Paper presented at the Offshore Technology Conference Brasil. https://doi.org/10.4043/29718-MS

Beltrán-Jiménez, K., Skadsem, H. J., Gardner, D., Kragset, S., & Lourenco de Souza, M. I. (2019b). *Leakage through Micro-annulus Geometries Incorporating Pressure-Driven Elastic Deformation.* Paper presented at the Offshore Technology Conference Brasil, Rio de Janeiro, Brazil, October 2019, Paper Number: OTC-29718-MS.

Bésuelle, P. (2001). Evolution of strain localisation with stress in a sandstone: brittle and semi-brittle regimes. *Physics and Chemistry of the Earth, Part A: Solid Earth and Geodesy, 26*(1-2), 101-106.

Biot, M. A. (1941). General theory of three ‐ dimensional consolidation. *Journal of applied physics*, *12*(2), 155-164.

Biot, M. A. (1977). Variational Lagrangian-thermodynamics of nonisothermal finite strain mechanics of porous solids and thermomolecular diffusion. *International Journal of Solids and Structures, 13*(6), 579-597.

Bly, M. (2011). *Deepwater Horizon accident investigation report*: Diane Publishing.

Bois, A.-P., Vu, M.-H., Noël, K., Badalamenti, A., Delabroy, L., Thérond, E., & Hansen, K. (2019). Evaluating cement-plug mechanical and hydraulic integrity. *SPE Drilling & Completion, 34*(02), 92-102.

Borja, R., & Kavazanjian, E. (1985). A constitutive model for the stress–strain–time behaviour of ‘wet’clays. *Geotechnique, 35*(3), 283-298.

Borja, R. I. (2004). Computational modeling of deformation bands in granular media. II. Numerical simulations. *Computer Methods in Applied Mechanics and Engineering, 193*(27-29), 2699-2718.

Bruneau, M., Chang, S. E., Eguchi, R. T., Lee, G. C., O'Rourke, T. D., Reinhorn, A. M., . . . Von Winterfeldt, D. (2003). A framework to quantitatively assess and enhance the seismic resilience of communities. *Earthquake spectra, 19*(4), 733-752.

Bu, Y., Du, J., Guo, S., Liu, H., & Huang, C. (2016). Properties of oil well cement with high dosage of metakaolin. *Construction and Building Materials, 112*, 39-48.

Cai, W., Deng, J., Luo, M., Feng, Y., Li, J., & Liu, Q. (2022). Recent advances of cementing technologies for ultra-HTHP formations. *International Journal of Oil, Gas and Coal Technology, 29*(1), 27-51.

Carroll, S., Carey, J. W., Dzombak, D., Huerta, N. J., Li, L., Richard, T., . . . Zhang, L. (2016). Role of chemistry, mechanics, and transport on well integrity in CO2 storage environments. *International journal of greenhouse gas control, 49*, 149-160.

Case, D. H., Wang, F., & Giammar, D. E. (2011). Precipitation of magnesium carbonates as a function of temperature, solution composition, and presence of a silicate mineral substrate. *Environmental Engineering Science, 28*(12), 881-889.

Chen, G., & Ewy, R. T. (2005). Thermoporoelastic effect on wellbore stability. *SpE Journal, 10*(02), 121-129.

Cheng, A. H.-D. (2016). *Poroelasticity* (Vol. 27): Springer.

Chizmeshya, A. V., McKelvy, M. J., Squires, K., Carpenter, R. W., & Béarat, H. (2007a). A novel approach to mineral carbonation: Enhancing carbonation while avoiding mineral pretreatment process cost. (924162). doi:https://doi.org/10.2172/924162

Chizmeshya, A. V., McKelvy, M. J., Squires, K., Carpenter, R. W., & Béarat, H. (2007b). *A novel approach to mineral carbonation: Enhancing carbonation while avoiding mineral pretreatment process cost*. Retrieved from https://doi.org/10.2172/924162

Corina, A. N., Opedal, N. v. d. T., Vrålstad, T., & Sangesland, S. (2019a). *Cement plug sealing studies of silica cement systems.* Paper presented at the International Conference on Offshore Mechanics and Arctic Engineering, June 9-14, 2019, Glasgow, Scotland, UK, Paper number: OMAE2019-95928, V008T11A056.

Corina, A. N., Opedal, N. v. d. T., Vrålstad, T., & Sangesland, S. (2019b). *Cement Plug Sealing Studies of Silica Cement Systems.* Paper presented at the International Conference on Offshore Mechanics and Arctic Engineering.

Davidovits, J. (1991). Geopolymers: inorganic polymeric new materials. *Journal of Thermal Analysis and calorimetry, 37*(8), 1633-1656.

de Brito, J., Thomas, C., Medina, C., & Agrela, F. (2021). *Waste and Byproducts in Cement-Based Materials: Innovative Sustainable Materials for a Circular Economy*: Woodhead Publishing.

De Silva, P., Bucea, L., Moorehead, D., & Sirivivatnanon, V. (2006). Carbonate binders: Reaction kinetics, strength and microstructure. *Cement and Concrete Composites, 28*(7), 613-620.

De Silva, P., Bucea, L., & Sirivivatnanon, V. (2009). Chemical, microstructural and strength development of calcium and magnesium carbonate binders. *Cement and concrete research, 39*(5), 460-465.

DeBruijn, G., Skeates, C., Greenaway, R., Harrison, D., Parris, M., James, S., . . . Temple, L. (2008). High-pressure, high-temperature technologies. *Oilfield Review, 20*(3), 46-60.

Delaney, P. T. (1982). Rapid intrusion of magma into wet rock: Groundwater flow due to pore pressure increases. *Journal of Geophysical Research: Solid Earth, 87*(B9), 7739-7756.

Derski, W. (1979). Equations of linear thermoconsolidation. *Archives of Mech., 31*(3), 303-316.

Detournay, E., & Atkinson, C. (2000). Influence of pore pressure on the drilling response in low-permeability shear-dilatant rocks. *International Journal of Rock Mechanics and Mining Sciences, 37*(7), 1091-1101.

Detournay, E., & Cheng, A.-D. (1988). Poroelastic response of a borehole in a non-hydrostatic stress field. *International Journal of Rock Mechanics and Mining Sciences & Geomechanics Abstracts, 25*(3), 171-182.

Drake, J. A., Bradford, A., & Marsalek, J. (2013). Review of environmental performance of permeable pavement systems: state of the knowledge. *Water Quality Research Journal of Canada, 48*(3), 203-222.

Du Bernard, X., Eichhubl, P., & Aydin, A. (2002). Dilation bands: A new form of localized failure in granular media. *Geophysical Research Letters, 29*(24), 29-21-29-24.

Duguid, A., Radonjic, M., & Scherer, G. W. (2011). Degradation of cement at the reservoir/cement interface from exposure to carbonated brine. *International Journal of Greenhouse Gas Control, 5*(6), 1413-1428.

Dusseault, M. B., Gray, M. N., & Nawrocki, P. A. (2000). *Why oilwells leak: cement behavior and long-term consequences.* Paper presented at the International Oil and gas conference and exhibition in China, Beijing, China, November 2000. Paper Number: SPE-64733-MS.

Dusseault, M. B., Gray, M. N., & Nawrocki, P. A. (2000). *Why Oilwells Leak: Cement Behavior and Long-Term Consequences*. Paper presented at the SPE-64733-MS. https://doi.org/10.2118/64733-MS

Duxson, P., Fernández-Jiménez, A., Provis, J. L., Lukey, G. C., Palomo, A., & van Deventer, J. S. (2007). Geopolymer technology: the current state of the art. *Journal of materials science, 42*(9), 2917-2933.

Eichhubl, P., Hooker, J. N., & Laubach, S. E. (2010). Pure and shear-enhanced compaction bands in Aztec Sandstone. *Journal of Structural Geology, 32*(12), 1873-1886.

Fossen, H., Schultz, R. A., Shipton, Z. K., & Mair, K. (2007). Deformation bands in sandstone: a review. *Journal of the Geological Society, 164*(4), 755-769.

Gaitero, J. J., Campillo, I., & Guerrero, A. (2008). Reduction of the calcium leaching rate of cement paste by addition of silica nanoparticles. *Cement and concrete research, 38*(8-9), 1112-1118.

Gao, J., Deng, J., Lan, K., Song, Z., Feng, Y., & Chang, L. (2017). A porothermoelastic solution for the inclined borehole in a transversely isotropic medium subjected to thermal osmosis and thermal filtration effects. *Geothermics, 67*, 114-134.

Gapais, D. (1989). Shear structures within deformed granites: mechanical and thermal indicators. *Geology, 17*(12), 1144-1147.

Ge, Z., Yao, X., Wang, X., Zhang, W., & Yang, T. (2018). Thermal performance and microstructure of oil well cement paste containing subsphaeroidal konilite flour in HTHP conditions. *Construction and Building Materials, 172*, 787-794.

Gerdemann, S. J., O'Connor, W. K., Dahlin, D. C., Penner, L. R., & Rush, H. (2007). Ex situ aqueous mineral carbonation. *Environmental science & technology, 41*(7), 2587-2593.

Gersevanov, N. (1937). Fundamentals of soil masses dynamics. *StroyIzdat, Moscow*.

Ghabezloo, S., & Sulem, J. (2010). Temperature induced pore fluid pressurization in geomaterials. *arXiv preprint arXiv:1011.6501*.

Ghassemi, A., & Diek, A. (2002). Porothermoelasticity for swelling shales. *Journal of Petroleum Science and Engineering, 34*(1-4), 123-135.

Ghassemi, A., Tao, Q., & Diek, A. (2009). Influence of coupled chemo-poro-thermoelastic processes on pore pressure and stress distributions around a wellbore in swelling shale. *Journal of Petroleum Science and Engineering, 67*(1-2), 57-64.

Giammar, D. E., Bruant Jr, R. G., & Peters, C. A. (2005). Forsterite dissolution and magnesite precipitation at conditions relevant for deep saline aquifer storage and sequestration of carbon dioxide. *Chemical Geology, 217*(3-4), 257-276.

Gibbons, G. J., Williams, R., Purnell, P., & Farahi, E. (2010). 3D Printing of cement composites. *Advances in Applied Ceramics, 109*(5), 287-290.

Ginebra, M., Driessens, F., & Planell, J. (2004). Effect of the particle size on the micro and nanostructural features of a calcium phosphate cement: a kinetic analysis. *Biomaterials, 25*(17), 3453-3462.

Gomar, M., Goodarznia, I., & Shadizadeh, S. R. (2014). Transient thermo-poroelastic finite element analysis of borehole breakouts. *International Journal of Rock Mechanics and Mining Sciences*, *71*, 418-428.

Gong, M., & Morriss, S. (1992). *Ultrasonic cement evaluation in inhomogeneous cements.* Paper presented at the SPE Annual Technical Conference and Exhibition, Washington, D.C., October 1992. Paper Number: SPE-24572-MS.

Goto, S., & Roy, D. M. (1981). The effect of w/c ratio and curing temperature on the permeability of hardened cement paste. *Cement and concrete research*, *11*(4), 575-579.

Group, D. H. S. (2011). Final report on the investigation of the Macondo well blowout. *Center for Catastrophic Risk Management, University of California at Berkeley*.

Gruber, S., & Plank, J. (2021). Challenges in Cementing Deep Offshore Wells. *Vietnam Symposium on Advances in Offshore Engineering*, 459-466. doi:https://doi.org/10.1007/978-981-16-7735-9_5

Guan, X., LIU, S., ZHANG, H., DOU, Z., QIU, M., & FENG, C. (2018). Carbonation and Hardening Properties of Low Calcium Silicates Minerals-A short review. *Journal of the Chinese Ceramic Society*, 02.

Gutberlet, T., Hilbig, H., & Beddoe, R. (2015). Acid attack on hydrated cement—Effect of mineral acids on the degradation process. *Cement and concrete research*, *74*, 35-43.

Hambach, M., Rutzen, M., & Volkmer, D. (2019). Properties of 3D-printed fiber-reinforced Portland cement paste. In *3D concrete printing technology* (pp. 73-113): Elsevier.

Hargis, C. W., Chen, I. A., Devenney, M., Fernandez, M. J., Gilliam, R. J., & Thatcher, R. P. (2021). Calcium Carbonate Cement: A Carbon Capture, Utilization, and Storage (CCUS) Technique. *Materials, 14*(11), 2709.

Hickman, R., & Gutierrez, M. (2007). Formulation of a three‐dimensional rate‐dependent constitutive model for chalk and porous rocks. *International journal for numerical and analytical methods in geomechanics, 31*(4), 583-605.

Hmadeh, L. (2021). *The Beginning of the End: A Digital Planning of P&A Operations.* NTNU,

Hou, P., Cheng, X., Qian, J., & Shah, S. P. (2014). Effects and mechanisms of surface treatment of hardened cement-based materials with colloidal nanoSiO2 and its precursor. *Construction and Building Materials*, *53*, 66-73.

Hou, P., Cheng, X., Qian, J., Zhang, R., Cao, W., & Shah, S. P. (2015). Characteristics of surface-treatment of nano-SiO2 on the transport properties of hardened cement pastes with different water-to-cement ratios. *Cement and Concrete Composites*, *55*, 26-33.

Ingraffea, A. R., Wells, M. T., Santoro, R. L., & Shonkoff, S. B. (2014). Assessment and risk analysis of casing and cement impairment in oil and gas wells in Pennsylvania, 2000–2012. *Proceedings of the National Academy of Sciences*, *111*(30), 10955-10960.

Issen, K. A., & Rudnicki, J. W. (2000). Conditions for compaction bands in porous rock. *Journal of Geophysical Research: Solid Earth, 105*(B9), 21529-21536.

Jackson, M. P., & Talbot, C. J. (1986). External shapes, strain rates, and dynamics of salt structures. *Geological Society of America Bulletin, 97*(3), 305-323.

Jacquey, A. B., Rattez, H., & Veveakis, M. (2021). Strain localization regularization and patterns formation in rate-dependent plastic materials with multiphysics coupling. *Journal of the Mechanics and Physics of Solids, 152*, 104422.

Jamison, W. R., & Stearns, D. W. (1982). Tectonic deformation of Wingate Sandstone, Colorado National Monument. *AAPG bulletin, 66*(12), 2584-2608.

Jiang, J., Li, J., Nie, J., Liu, G., Huang, T., & Li, W. (2019). *Study on Influence of Mechanical Parameters of Cement Plug on Sealing Integrity of Abandoned Wellbore*. Paper presented at the International Conference on Computational & Experimental Engineering and Sciences. https://doi.org/10.1007/978-3-030-27053-7_50

Kaiser, M. J., & Narra, S. (2018). A hybrid scenario-based decommissioning forecast for the shallow water US Gulf of Mexico, 2018–2038. *Energy*, *163*, 1150-1177.

Katende, A., Lu, Y., Bunger, A., & Radonjic, M. (2020a). Experimental quantification of the effect of oil based drilling fluid contamination on properties of wellbore cement. *Journal of Natural Gas Science and Engineering, 79*, 103328.

Katende, A., Lu, Y., Bunger, A., & Radonjic, M. (2020b). Experimental Quantification Of The Effect Of Oil Based Drilling Fluid Contamination On Properties Of Wellbore Cement. *Journal of Natural Gas Science and Engineering*, 103328.

Kelemen, P. B., & Matter, J. (2008). In situ carbonation of peridotite for CO2 storage. *Proceedings of the National Academy of Sciences*, *105*(45), 17295-17300.

Khalifeh, M., & Saasen, A. (2020). *Introduction to permanent plug and abandonment of wells*: Springer Nature.

Khalifeh, M., Saasen, A., Vralstad, T., & Hodne, H. (2014). Potential utilization of class C fly ash-based geopolymer in oil well cementing operations. *Cement and Concrete Composites, 53*, 10-17.

Kiran, R., Teodoriu, C., Dadmohammadi, Y., Nygaard, R., Wood, D., Mokhtari, M., & Salehi, S. (2017). Identification and evaluation of well integrity and causes of failure of well integrity barriers (A review). *Journal of Natural Gas Science and Engineering, 45*, 511-526.

Koťátková, J., Zatloukal, J., Reiterman, P., & Kolář, K. (2017). Concrete and cement composites used for radioactive waste deposition. *Journal of environmental radioactivity, 178*, 147-155.

Krakowiak, K. J., Thomas, J. J., James, S., Abuhaikal, M., & Ulm, F.-J. (2018). Development of silica-enriched cement-based materials with improved aging resistance for application in high-temperature environments. *Cement and concrete research, 105*, 91-110.

Kurashige, M. (1989). A thermoelastic theory of fluid-filled porous materials. *International Journal of Solids and Structures, 25*(9), 1039-1052.

Kutchko, B. G., Strazisar, B. R., Dzombak, D. A., Lowry, G. V., & Thaulow, N. (2007). Degradation of well cement by CO2 under geologic sequestration conditions. *Environmental science & technology, 41*(13), 4787-4792.

Kutchko, B. G., Strazisar, B. R., Lowry, G. V., Dzombak, D. A., & Thaulow, N. (2008). Rate of CO2 attack on hydrated class H well cement under geologic sequestration conditions. *Environmental science & technology, 42*(16), 6237-6242.

Lackner, K. S., Butt, D. P., & Wendt, C. H. (1997). Progress on binding CO2 in mineral substrates. *Energy Conversion and Management, 38*, S259-S264.

Li, Y., & Radonjic, M. (2019). *Microstructural Comparison of the Impact of Drilling Fluids Contamination and Casing Corrosion on Wellbore Cement Barriers*. Paper presented at the 53rd U.S. Rock Mechanics/Geomechanics Symposium. ARMA-2019-2082

Lisabeth, H., Zhu, W., Kelemen, P., & Ilgen, A. (2017). Experimental evidence for chemo-mechanical coupling during carbon mineralization in ultramafic rocks. *Earth and Planetary Science Letters, 474*, 355-367.

Lu, Y., & Bunger, A. Semi-Analytical Solution for Thermo-Poro-Elastic Stresses in a Wellbore Cement Plug and Implications for Cement Properties that Minimize Risk of Failure.

Luhar, I., Luhar, S., Abdullah, M. M. A. B., Razak, R. A., Vizureanu, P., Sandu, A. V., & Matasaru, P.-D. (2021). A state-of-the-art review on innovative geopolymer composites designed for water and wastewater treatment. *Materials, 14*(23), 7456.

Mahmood, W., Khan, A.-u.-R., & Ayub, T. (2021). Carbonation Resistance in Ordinary Portland Cement Concrete with and without Recycled Coarse Aggregate in Natural and Simulated Environment. *Sustainability, 14*(1), 437.

Marangu, J. M., Thiong'o, J. K., & Wachira, J. M. (2019). Review of carbonation resistance in hydrated cement based materials. *Journal of Chemistry, 2019*.

Massion, C., Radonjic, M., Lu, Y., Bunger, A., & Crandall, D. (2021). *Impact of Graphene and the Testing Conditions on the Wellbore Cement Mechanical and Microstructural Properties.* Paper presented at the 55th US Rock Mechanics/Geomechanics Symposium, Paper number: ARMA 21–2089 20-23, June, 2021, Houston, Texas.

Massion, C., Vissa, V. S., Lu, Y., Crandall, D., Bunger, A., & Radonjic, M. (2022). Geomimicry-Inspired Micro-Nano Concrete as Subsurface Hydraulic Barrier Materials: Learning from Shale Rocks as Best Geological Seals. In *REWAS 2022: Energy Technologies and CO2 Management (Volume II)* (pp. 129-138): Springer.

Meng, M., Frash, L. P., Carey, J. W., Li, W., Welch, N. J., & Zhang, W. (2021). Cement stress and microstructure evolution during curing in semi-rigid high-pressure environments. *Cement and concrete research, 149*, 106555.

Mo, L., Deng, M., Tang, M., & Al-Tabbaa, A. (2014). MgO expansive cement and concrete in China: Past, present and future. *Cement and concrete research, 57*, 1-12.

Mo, L., Zhang, F., Panesar, D. K., & Deng, M. (2017). Development of low-carbon cementitious materials via carbonating Portland cement–fly ash–magnesia blends under various curing scenarios: a comparative study. *Journal of cleaner production, 163*, 252-261.

Morandeau, A. E., & White, C. E. (2015a). In situ X-ray pair distribution function analysis of accelerated carbonation of a synthetic calcium–silicate–hydrate gel. *Journal of Materials Chemistry A, 3*(16), 8597-8605.

Morandeau, A. E., & White, C. E. (2015b). Role of magnesium-stabilized amorphous calcium carbonate in mitigating the extent of carbonation in alkali-activated slag. *Chemistry of Materials, 27*(19), 6625-6634.

Norge, S. (2013). NORSOK Standard D-010: Well integrity in drilling and well operations, Rev. 4. In: Standards Norway: Lysaker.

O’Connor, W., Dahlin, D., Rush, G., Gerdemann, S., Penner, L., & Nilsen, D. (2005a). Aqueous mineral carbonation. *Final Report–DOE/ARC-TR-04-002*.

O’connor, W., Dahlin, D., Rush, G., Gerdemann, S., Penner, L., & Nilsen, D. (2005b). Aqueous mineral carbonation: Mineral availability, pretreatment, reaction parametrics, and process studies. *National Energy Technology Laboratory, US DOE. Available online: http://www. webcitation. org/query*, 3051-3075.

Oelkers, E. H. (2001). An experimental study of forsterite dissolution rates as a function of temperature and aqueous Mg and Si concentrations. *Chemical Geology, 175*(3-4), 485-494.

Oil, & Gas, U. (2015). Decommissioning Insight 2015. In.

Okubo, C. H., & Schultz, R. A. (2005). Evolution of damage zone geometry and intensity in porous sandstone: insight gained from strain energy density. *Journal of the Geological Society, 162*(6), 939-949.

Olson, J., Eustes, A., Fleckenstein, W., Eker, E., Baker, R., & Augustine, C. (2015). Completion Design Considerations for a Horizontal Enhanced Geothermal System. *GRC Transactions, 39*, 335-344.

Olsson, W., & Holcomb, D. (2000). Compaction localization in porous rock. *Geophysical Research Letters, 27*(21), 3537-3540.

Olsson, W. A. (1999). Theoretical and experimental investigation of compaction bands in porous rock. *Journal of Geophysical Research: Solid Earth, 104*(B4), 7219-7228.

Olsson, W. A., Lorenz, J. C., & Cooper, S. P. (2004). A mechanical model for multiply-oriented conjugate deformation bands. *Journal of Structural Geology, 26*(2), 325-338.

Pearson, C. (1981). The relationship between microseismicity and high pore pressures during hydraulic stimulation experiments in low permeability granitic rocks. *Journal of Geophysical Research: Solid Earth, 86*(B9), 7855-7864.

Pfiffner, O.-A., & Ramsay, J. (1982). Constraints on geological strain rates: arguments from finite strain states of naturally deformed rocks. *Journal of Geophysical Research: Solid Earth, 87*(B1), 311-321.

Picandet, V., Rangeard, D., Perrot, A., & Lecompte, T. (2011). Permeability measurement of fresh cement paste. *Cement and concrete research, 41*(3), 330-338.

Pittman, E. D. (1981). Effect of fault-related granulation on porosity and permeability of quartz sandstones, Simpson Group (Ordovician), Oklahoma. *AAPG bulletin, 65*(11), 2381-2387.

Power, I. M., Harrison, A. L., Dipple, G. M., Wilson, S. A., Kelemen, P. B., Hitch, M., & Southam, G. (2013). Carbon mineralization: from natural analogues to engineered systems. *Reviews in Mineralogy and Geochemistry, 77*(1), 305-360.

Qin, J., Pang, X., Cheng, G., Bu, Y., & Liu, H. (2021). Influences of different admixtures on the properties of oil well cement systems at HPHT conditions. *Cement and Concrete Composites*, *123*, 104202.

Regenauer-Lieb, K., Veveakis, M., Poulet, T., Wellmann, F., Karrech, A., Liu, J., . . . Fusseis, F. (2013). Multiscale coupling and multiphysics approaches in earth sciences: Applications. *Journal of Coupled Systems and Multiscale Dynamics, 1*(3), 281-323.

Rouillac, D. (1994). *Cement evaluation logging handbook*: Éditions Technip.

Rudnicki, J. W., & Rice, J. (1975). Conditions for the localization of deformation in pressure-sensitive dilatant materials. *Journal of the Mechanics and Physics of Solids, 23*(6), 371-394.

Samarakoon, M., Ranjith, P., & Wanniarachchi, W. (2022). Properties of well cement following carbonated brine exposure under HTHP conditions: A comparative study of alkali-activated and class G cements. *Cement and Concrete Composites*, *126*, 104342.

Sanchez, M., Alonso, M., & González, R. (2014). Preliminary attempt of hardened mortar sealing by colloidal nanosilica migration. *Construction and Building Materials, 66*, 306-312.

Santarelli, F., Tronvoll, J., Svennekjaier, M., Skeie, H., Henriksen, R., & Bratli, R. (1998). *Reservoir stress path: the depletion and the rebound.* Paper presented at the SPE/ISRM Rock Mechanics in Petroleum Engineering.

Sarout, J., & Detournay, E. (2011). Chemoporoelastic analysis and experimental validation of the pore pressure transmission test for reactive shales. *International Journal of Rock Mechanics and Mining Sciences, 48*(5), 759-772.

Schmitt, D., & Zoback, M. (1989). *Laboratory tests of the effects of pore pressure on tensile failure.* Paper presented at the ISRM International Symposium, paper number: ISRM-IS-1989-111.

Scholz, M., & Grabowiecki, P. (2007). Review of permeable pavement systems. *Building and environment, 42*(11), 3830-3836.

Senff, L., Labrincha, J. A., Ferreira, V. M., Hotza, D., & Repette, W. L. (2009). Effect of nano-silica on rheology and fresh properties of cement pastes and mortars. *Construction and Building Materials*, *23*(7), 2487-2491.

Shadravan, A., Schubert, J., Amani, M., & Teodoriu, C. (2014). *HPHT cement sheath integrity evaluation method for unconventional wells.* Paper presented at the SPE International Conference on Health, Safety, and Environment.

Shakor, P., Sanjayan, J., Nazari, A., & Nejadi, S. (2017). Modified 3D printed powder to cement-based material and mechanical properties of cement scaffold used in 3D printing. *Construction and Building Materials, 138*, 398-409.

Sigda, J. M., Goodwin, L. B., Mozley, P. S., & Wilson, J. L. (1999). Permeability alteration in small-displacement faults in poorly lithified sediments: Rio Grande Rift, Central New Mexico. *Washington DC American Geophysical Union Geophysical Monograph Series, 113*, 51-68.

Singh, L., Karade, S., Bhattacharyya, S., Yousuf, M. M., & Ahalawat, S. (2013). Beneficial role of nanosilica in cement based materials–A review. *Construction and Building Materials, 47*, 1069-1077.

Smith, D. W., & Booker, J. R. (1993). Green's functions for a fully coupled thermoporoelastic material. *International Journal for Numerical and Analytical Methods in Geomechanics, 17*(3), 139-163.

Snee, J.-E. L., & Zoback, M. D. (2018). State of stress in the Permian Basin, Texas and New Mexico: Implications for induced seismicity. *The Leading Edge, 37*(2), 127-134.

Song, Z., Liang, F., Lin, C., & Xiang, Y. (2019). Interaction of pore pressures in double-porosity medium: Fluid injection in borehole. *Computers and Geotechnics, 107*, 142-149.

Standard, N. (2004). Well integrity in drilling and well operations. *D-010, rev, 3*.

Stehfest, H. (1970). Algorithm 368: Numerical inversion of Laplace transforms [D5]. *Communications of the ACM, 13*(1), 47-49.

Summerhayes, C. (2011). Deep water–the gulf oil disaster and the future of offshore drilling. *Underwater Technology, 30*(2), 113-115.

Tao, Q., & Ghassemi, A. (2010). Poro-thermoelastic borehole stress analysis for determination of the in situ stress and rock strength. *Geothermics, 39*(3), 250-259.

Taylor, D. W. (1948). *Fundamentals of soil mechanics* (Vol. 66): LWW.

Terzaghi, K. (1925). *Erdbaumechanik auf bodenphysikalischer Grundlage*: F. Deuticke.

Trudel, E., Bizhani, M., Zare, M., & Frigaard, I. (2019). Plug and abandonment practices and trends: A British Columbia perspective. *Journal of Petroleum Science and Engineering, 183*, 106417.

Unluer, C., & Al-Tabbaa, A. (2013). Impact of hydrated magnesium carbonate additives on the carbonation of reactive MgO cements. *Cement and concrete research, 54*, 87-97.

Valov, A., Golovin, S., Shcherbakov, V., & Kuznetsov, D. (2022). Thermoporoelastic model for the cement sheath failure in a cased and cemented wellbore. *Journal of Petroleum Science and Engineering, 210*, 109916.

Verruijt, A. (2016). *Theory of groundwater flow*: Macmillan International Higher Education.

Veveakis, E., Alevizos, S., & Vardoulakis, I. (2010). Chemical reaction capping of thermal instabilities during shear of frictional faults. *Journal of the Mechanics and Physics of Solids, 58*(9), 1175-1194.

Veveakis, E., & Regenauer-Lieb, K. (2015). Cnoidal waves in solids. *Journal of the Mechanics and Physics of Solids, 78*, 231-248.

Vrålstad, T., Saasen, A., Fjær, E., Øia, T., Ytrehus, J. D., & Khalifeh, M. (2019). Plug & abandonment of offshore wells: Ensuring long-term well integrity and cost-efficiency. *Journal of Petroleum Science and Engineering, 173*, 478-491.

Wang, Y., & Dusseault, M. B. (2003). A coupled conductive–convective thermo-poroelastic solution and implications for wellbore stability. *Journal of Petroleum Science and Engineering, 38*(3-4), 187-198.

Water, D. (2011). The Gulf Oil Disaster and the Future of Offshore Drilling, Report to the President. *National Commission on the BP Deepwater Horizon*, 226.

Weisstein, E. W. (2002). Eigen decomposition. https://mathworld. *wolfram. com/*.

Wolf, H., König, D., & Triantafyllidis, T. (2003). Experimental investigation of shear band patterns in granular material. *Journal of Structural Geology, 25*(8), 1229-1240.

Wong, T. f., Baud, P., & Klein, E. (2001). Localized failure modes in a compactant porous rock. *Geophysical Research Letters, 28*(13), 2521-2524.

Zhang, Z., Li, L., Ma, X., & Wang, H. (2016). Compositional, microstructural and mechanical properties of ambient condition cured alkali-activated cement. *Construction and Building Materials, 113*, 237-245.

Zhou, X., & Ghassemi, A. (2009). Finite element analysis of coupled chemo-poro-thermo-mechanical effects around a wellbore in swelling shale. *International Journal of Rock Mechanics and Mining Sciences*, *46*(4), 769-778.

Zhu, W., Fusseis, F., Lisabeth, H., Xing, T., Xiao, X., De Andrade, V., & Karato, S. i. (2016). Experimental evidence of reaction ‐ induced fracturing during olivine carbonation. *Geophysical Research Letters*, *43*(18), 9535-9543.

Zoback, M., Barton, C., Brudy, M., Castillo, D., Finkbeiner, T., Grollimund, B., . . . Wiprut, D. (2003). Determination of stress orientation and magnitude in deep wells. *International Journal of Rock Mechanics and Mining Sciences, 40*(7-8), 1049-1076.